UNIVERSITY OF CALIFORNIA
RIVERSIDE

Graphene Nanoelectromechanical Systems

A Dissertation submitted in partial satisfaction
of the requirements for the degree of

Doctor of Philosophy

in

Physics

by

Tengfei Miao

March 2015

Dissertation Committee:

Dr. Marc Bockrath , Chairperson
Dr. Ward Beyermann
Dr. Nathaniel Gabor

The Dissertation of Tengfei Miao is approved:

Committee Chairperson

University of California, Riverside

Acknowledgments

I would like to thank my advisor, Professor Marc Bockrath. With his guidance, I feel I had an amazing journey in research during the past five years. His deep insight into science makes him a great source of knowledge and inspiration to me. He is always kind, patient and supportive, no matter what kind of silly questions I ask. His respect to each individual makes the whole lab filled with free atmosphere. I feel truly fortunate to be his student.

I would also like to thank the committee members of my defense and candidacy exams: Professor Ward Beyermann, Professor Nathaniel Gabor, Professor Jeanie Lau, Professor Shan-Wen Tsai and Professor Jianlin Liu. I want to give my special thanks to Professor Lau for the wonderful collaboration and inspiring discussions. I also thank her for generously allowing me to use her equipment.

My research could never progress here without the contribution from my co-workers: Sinchul Yeom, Peng Wang and Brian Standley. I also thank the other current Bockrath group members: Bin Cheng, Yong Wu, Cheng Pan, Yi Wu, Juan Aguilera, Oleg Martynov, Adrian Nosek, Sean Nelson, Nan Zhang, Rui Lv and the former group members: Professor Hsin-Ying Chiu, Anthony Mendez, Honest Makamba for the discussions and various technical supports. My thanks also go to the whole Lau group members for their assistance and advise.

I also thank my roommates, Fenglin Wang and Peng Wang, and all my friends here. Your friendships are important for me to survive the graduate school life. Most importantly, I thank my parents for their endless love and support.

Finally, I thank ACS Publications for allowing me to reprint my previous published work [1] in Chapter 3, 4 and 5.

To my parents for all the support.

ABSTRACT OF THE DISSERTATION

Graphene Nanoelectromechanical Systems

by

Tengfei Miao

Doctor of Philosophy, Graduate Program in Physics
University of California, Riverside, March 2015
Dr. Marc Bockrath , Chairperson

Graphene, a carbon-based two-dimensional material, has remarkable electrical and mechanical properties, making it an ideal material for studying the Nanoelectromechanical Systems (NEMS). In this thesis, we focus on the performance of few-layer graphene NEMS resonators in drumhead geometry. We will discuss the experimental techniques and studies on their intrinsic properties, nonlinear dynamics and quality factor. We report our measurement on the coefficient of the Duffing nonlinearity, suggesting a geometric origin of this term. The line width of resonance at large drives is enhanced by nonlinear damping, in qualitative agreement with recent theory of damping by radiation of in-plane phonons. The amplitude of response is parametrically amplified due to periodic thermal expansion from the ac source-drain voltage, resulting an anomalously large line width at the largest drives. We observe Q scales inversely with the temperature. We develop a model that includes the intermodal coupling in tensioned graphene resonators and demonstrate Q is determined by the stochastic frequency broadening rather than frictional damping. We will also report our work on a graphene/h-BN (hexagonal boron nitride) drum resonator and discuss its potential applications.

Contents

List of Figures

Chapter 1

Introduction

1.1 Introduction

Nanoelectromechanical systems (NEMS) are the successor of microelectromechanical systems (MEMS). They integrate the electrical and mechanical functionality of devices on the submicron scale. Particularly, for a resonant NEMS device, the input electrical signal couples to the device and excite resonant modes of the mechanical element. The mechanical resonance is then transduced back into the electrical signal. [2] One simple example of such type of devices is a doubly-clamped beam resonator. The low-dimensional carbon-based materials such as carbon nanotubes [3] and graphene [4] are ideal materials for making the NEMS devices because of their miniature sizes, remarkable electrical and mechanical properties. They are promising for applications including ultra-sensitive mass sensing [5, 6, 7], and signal processing [8, 9], and are also good systems for studying nonlinear physics [10, 11]. This thesis will focus on the performance of graphene nanoelectromechanical resonators.

1.2 Electronic Properties of Graphene

Monolayer graphene is a sheet of carbon atoms arranged in a honeycomb lattice. The conduction band and valence band touch at isolated points at the corners of the Brillouin zone, and the touching points are named Dirac points. The low energy band structure near the Dirac point has a linear dispersion relation:

$$E_{\pm}(\mathbf{q}) \approx \pm v_F|\mathbf{q}| \tag{1.1}$$

where $\mathbf{q}$ is the momentum relative to the Dirac point and v_F is Fermi velocity [12]. The electronic states are described by a massless Dirac equation. Due to its low electron effective mass, graphene obtains a high mobility with an intrinsic limit of $2 \times 10^5\,\mathrm{cm^2V^{-1}s^{-1}}$ at room temperature. [13] This high room temperature field effect mobility greatly enhance the transduced signal of the graphene mechanical resonators and make them promising for real applications.

1.3 Mechanical Properties of Graphene

Graphene has excellent elastic properties. It has high stiffness: the 2D elastic stiffness of monolayer graphene is measured to be 340N/m, corresponding to an effective Young's modulus of 1TPa. It can also take strains up to 25% without breaking. [14] It also has low mass ($\rho = 7.6 \times 10^{-19}\mathrm{kg}/\mu\mathrm{m}^2$). Because of the high stiffness and low mass, a graphene NEMS resonator has a high fundamental resonance frequency. The low mass also increases its sensitivity to the applied forces. Because graphene is atomically thin, the mechanics behaves as an elastic membrane. The fundamental frequency of a monolayer or few-layer graphene NEMS resonator is typically tension dominated and the bending energy can be neglected. This allows us to study to the intermodal coupling.

1.4 Harmonic Oscillator

Here we follow ref. [15] to explore the behavior of a driven harmonic oscillator under damping. In addition to the driving force, the oscillator experiences frictional damping forces that tend to damp the oscillation. In the linear damping case, the frictional damping force is proportional to the velocity. The equation of motion is

$$m\ddot{z} + m\omega_0^2 z + m\Gamma\dot{z} = F, \tag{1.2}$$

where m is the mass of the oscillator, ω_0 is the resonance frequency which is intrinsic to the oscillator, z is the displacement of the oscillator, $m\omega_0^2 z$ is the restoring force, $m\Gamma\dot{z}$ is the frictional damping force and $F = F_0\cos(\omega t)$ is the driving force. We can simplify the above equation by defining $\gamma = \Gamma/m$:

$$\ddot{z} + \omega_0^2 z + \gamma\dot{z} = F/m. \tag{1.3}$$

To solve this equation, we first write F in the form of $F_0 e^{i\omega t}$ and the solution in the form of $z^0 e^{i\omega t}$. Then we solve for z^0. The final solution should be the real part of $z^0 e^{i\omega t}$. By plugging $z = z^0 e^{i\omega t}$ into the homogeneous equation, we have

$$-\omega^2 + \omega_0^2 + i\gamma\omega = 0. \tag{1.4}$$

This leads to

$$\omega = \pm\sqrt{\omega_0^2 - \gamma^2/4} + i\gamma/2. \tag{1.5}$$

For our graphene mechanical resonators measured in a vacuum condition, we are usually in the situation where $\omega_0^2 > \gamma^2/4$. Thus we can get the transient solution of the homogeneous equation:

$$z_t(t) = z_t^0 e^{-\frac{\gamma}{2}t}\cos(t\sqrt{\omega_0^2 - \gamma^2/4} + \phi_t), \tag{1.6}$$

where z_t^0 and ϕ_t are determined by the initial conditions. The amplitude of the transient solution decays as time goes on.

The non-homogeneous equation, we can first get the susceptibility:

$$\chi(\omega) = \frac{z(\omega)}{F(\omega)} = \frac{1}{m}\frac{1}{-\omega^2 + \omega_0^2 + i\omega\gamma} \tag{1.7}$$

By taking the real part of $\chi(\omega)F_0e^{i\omega t}$, we can get the steady-state solution satisfying the non-homogeneous equation:

$$z_s(t) = z_s^0 \cos(\omega t + \phi_s), \tag{1.8}$$

where

$$z_s^0 = \frac{F_0/m}{\sqrt{(\omega_0^2 - \omega^2)^2 + (\omega\gamma)^2}}. \tag{1.9}$$

Here ϕ_s is the phase of the response relative to the driving force. We should have

$$\phi_s = \arctan(\frac{\omega\gamma}{\omega^2 - \omega_0^2}). \tag{1.10}$$

Fig. 1.1 plots z_s^0 and ϕ_s near the resonance frequency ω_0. The final solution should be a combination of the transient and steady-state solutions:

$$z(t) = z_t(t) + z_s(t). \tag{1.11}$$

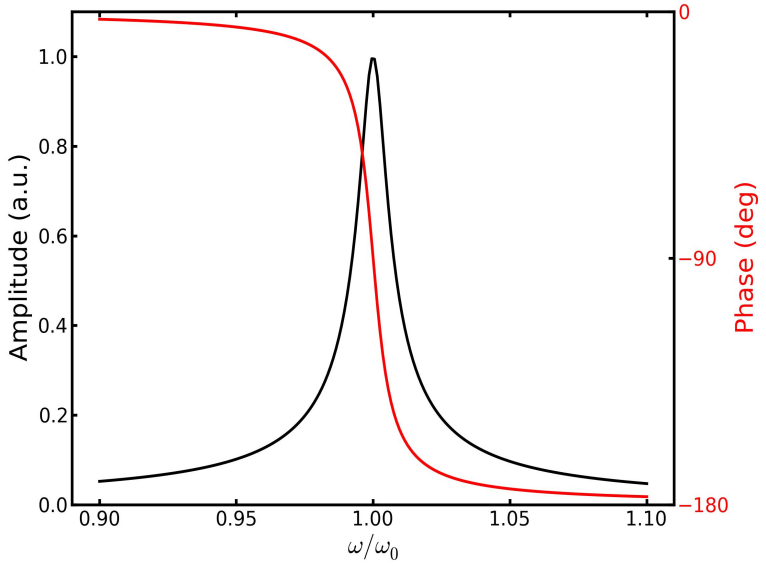

Figure 1.1: Amplitude and phase of steady-state response of a harmonic oscillator with damping. The amplitude z_s^0 is a Lorentzian function of ω with a peak at the resonance frequency ω_0. As the frequency goes through ω_0, the phase ϕ_s goes from 0 to $-\pi$ through $-\pi/2$ at the resonance frequency.

There is an important parameter called quality factor Q that characterizes the energy loss (damping) in the oscillator. The definition is

$$Q = 2\pi \frac{\text{Energy Stored}}{\text{Energy dissipated per cycle}}. \tag{1.12}$$

It can be shown that $Q = \omega_0/\gamma$. Then the displacement z has the form of

$$z_t(t) = z_t^0 e^{-\frac{\omega_0}{2Q}t} \cos(t\sqrt{\omega_0^2 - (\omega_0/2Q)^2} + \phi_t) \tag{1.13}$$

and

$$z_s(t) = \frac{F_0/m}{\sqrt{(\omega_0^2 - \omega^2)^2 + (\omega\omega_0/Q)^2}} \cos(\omega t + \phi_s), \tag{1.14}$$

where $\phi_s = \arctan(\frac{\omega\omega_0/Q}{\omega^2 - \omega_0^2})$. If the driving force is turned off, the amplitude of the oscillation decays. Since the energy stored in the oscillator is $\frac{1}{2}kz_t^2$, the decay of energy is twice as fast as the decay of the amplitude of displacement. It can be shown that it takes about a number of Q oscillation cycles for the energy to drop to $e^{-2\pi}$ of the initial

energy. We usually define that the energy decays as $e^{-t/\tau}$. Here $\tau = Q/\omega_0$ is defined as the characteristic time scale of the resonance.

Chapter 2

Device Fabrication and Measurement Techniques

2.1 Introduction

The most two common geometries of graphene NEMS resonators are the drum resonators and the doubly-clamped resonators. One of the drawbacks of the doubly-clamped resonators is they sometimes have vibrational modes at the free edges (edge modes) due to the nonuniform stress in some of the resonators [16], which makes the analysis more complicated. The drum resonators eliminate this edge mode problem. So throughout the thesis, we mainly focus on the performance of suspended graphene drum resonators. The monolayer and multilayer graphene can be obtained by two methods: mechanical exfoliation of graphite using scotch tapes [17] and chemical vapor deposition (CVD)[18]. Here we used both of the two types of graphene and developed two different procedures to fabricate the devices. The fabrication prodecures will be discussed in Section 2.2 and Section 2.3.The electrical measurement techniques and measurement setups are described in the following sections.

2.2 Drum Resonator Made by Exfoliated Graphene

Our goal is to fabricate a graphene field effect transistor on a Si/SiO_2 substrate, with the center part of the graphene suspended on a circular hole. The fabrication procedure has three stages: first, we fabricate arrays of circular holes in the SiO_2, and deposit graphene onto the holes; second, we tailor the graphene into a small size to maximize the ratio between suspended and unsuspended part; third, we fabricate source-drain electrodes to the graphene.

Stage one is shown in Fig. 2.1. First, we start with a p-doped Si chip with 290 nm of SiO_2. We want to fabricate circular holes in the oxide layer with a diameter of $2\,\mu$m. Here we choose buffered oxide etch (BOE) to wet etch the SiO_2, and electron-beam lithography to define the etch mask. One MMA resist layer (a positive e-beam resist) is spun onto the chip with a rotational speed of 4000 rpm, and a ramp-up rate of 1000 rpm/s. Then the chip with MMA resist is baked on a hot plate at $150\,^{\circ}$C for 10 minutes. After that, e-beam lithography is used to pattern arrays of holes with a diameter of $1.4\,\mu$m as an etching mask for the SiO_2. The e-beam exposed MMA resist is then developed in MIBK/IPA (1:3) solution for 65 seconds. Then we use BOE to etch the SiO_2 for 200 seconds. The etch rate is about 1.5 nm/s, so the 290 nm of SiO_2 should all be etched away. Since the BOE etching is isotropic, the actual diameter of the holes will be about 600 nm larger than $1.4\,\mu$m. After etching, the chip is transfered into a beaker with deionized (DI) water. Then it is transfered into another beaker with new DI water. We rinse the chip this way for 6 times. After that we use acetone to dissolve the MMA resist, and rinse the chip with isopropyl alcohol (IPA).

Now we have the chip with arrays of holes on the SiO_2. The next step is to use the scotch tape method to get the exfoliated graphene and randomly deposit them onto

the chip. There should be a chance that the graphene flakes land on some of the holes and form "graphene drums". Then we search for the "graphene drums" using optical microscope. Once the "drums" are found, we can do a Raman spectroscopy on them to find the number of layers of graphene.

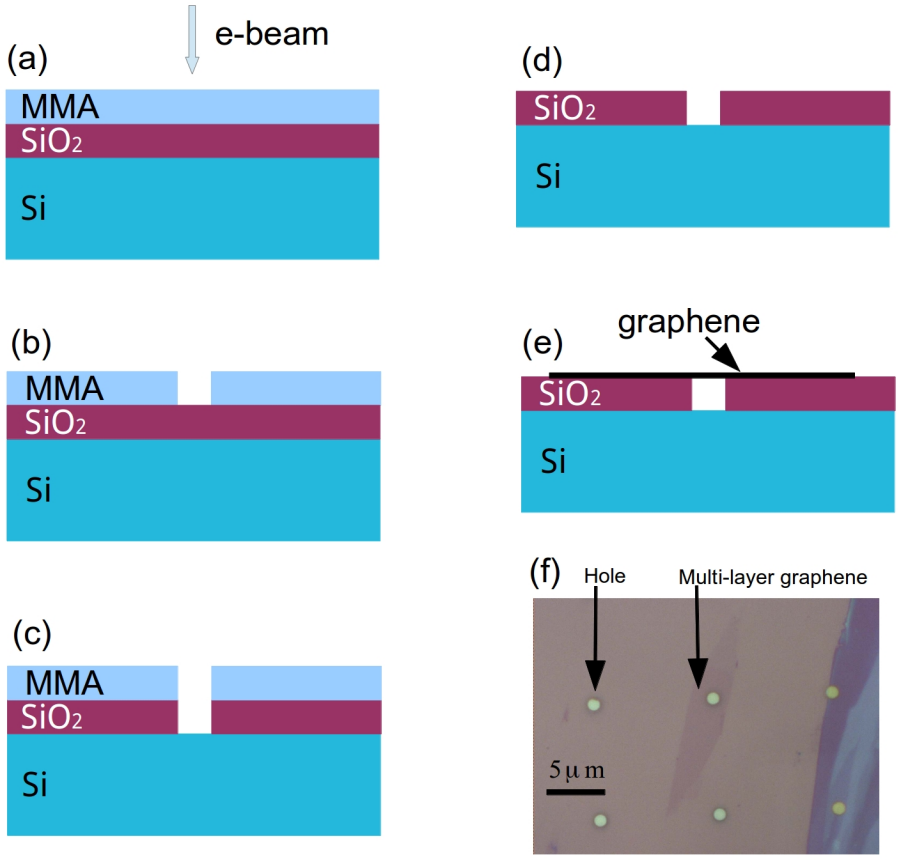

Figure 2.1: Fabrication procedure for graphene drum on SiO_2. (a) A MMA resist layer is spun on the chip followed by e-beam exposure. (b) The exposed resist is developed in MIBK/IPA(1:3) solution. (c) The SiO_2 is etched by BOE with the MMA resist mask. (d) MMA resist is dissolved by acetone. (e) Graphene is mechanical exfoliated and randomly deposited onto the holes. (f) Optical image of a multi-layer graphene drum.

The deposited graphene layers are usually larger than the holes, so we need to tailor them into smaller shapes. This is to make sure that the suspended graphene

dominate the conductance of the devices. Here we use PMMA, another positive e-beam resist, to define a etch mask for the graphene. However, spinning e-beam resist onto the chip in most of the cases will collapse the suspended graphene. In order to avoid this, we developed a new technique to dry transfer the e-beam resist onto the chip. The procedure is as follows. We prepare another chip with a little smaller size than the chip with the graphene drum, and spin coat a layer of water soluble poly(vinyl alcohol) (PVA) and then a layer of PMMA on it. Then we carefully cover the chip with a piece of blue dicing tape with a slightly larger size and press the tape to squeeze out the bubbles. We then put the chip/PVA/PMMA/tape in DI water on a hot plate and wait until the PVA is dissolved by water. The chip is now separated with the tape/PMMA bilayer. Then we take the tape/PMMA bilayer out from the DI water and blow-dry it with nitrogen gas. After that, we press the PMMA/tape onto the chip with the graphene drum carefully. The last step is to put the chip/PMMA/tape onto a hot plate at 120 °C, and slowly peel off the blue tape leaving the PMMA on the chip. Now the PMMA is successfully dry transferred onto the graphene drum. Then we use e-beam lithography to pattern a mask for etching the graphene. The graphene is then tailored using oxygen plasma etching. With the etch mask still on the chip, another layer of PMMA is spun coated on to the chip. We then use e-beam lithography to pattern the window for source-drain electrodes and use e-beam evaporator to deposit Ti/Au electrodes. The lift-off process is done in acetone at 60 °C for 15 minutes. Here we only use 15 minutes to minimize the chance of collapsing the graphene. After that, the device is transferred carefully into IPA. A critical point drying is followed to prevent the graphene drum from being damaged by the surface tension of liquid.[19]

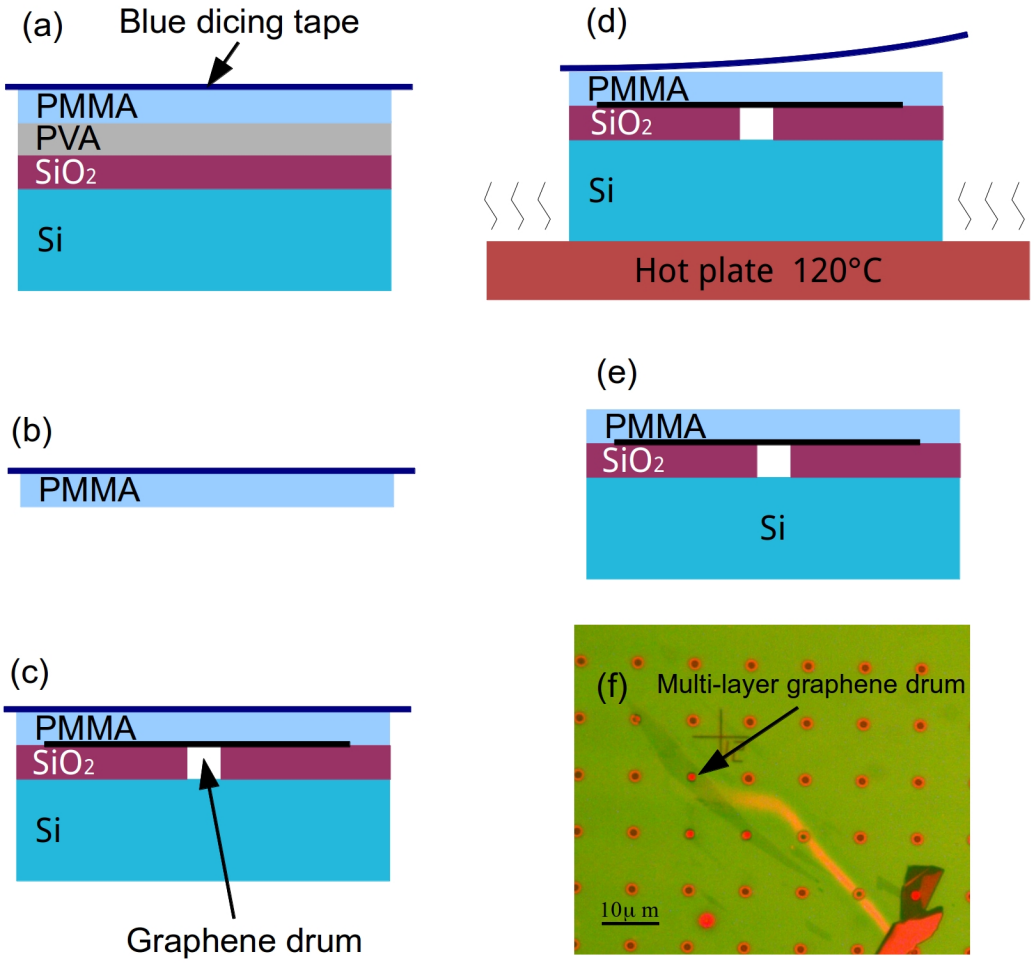

Figure 2.2: Fabrication procedure for dry transferring the PMMA resist. (a) A PVA/PMMA bi-layer is spun on a silicon chip, and a blue dicing tape is pressed on top of the PMMA. (b) The PVA layer is dissolved by water leaving the PMMA on the blue tape. (c) The PMMA/tape bi-layer is transferred onto the chip with the graphene drum on it. (d) The tape/PMMA/Graphene/SiO_2/Si chip is placed on a hot plate at 120 °C and the blue tape is peeled off. (e) PMMA resist is transferred onto the graphene drum. (f) Optical image of a multi-layer graphene drum with PMMA on it. It shows that the graphene drum has a smaller size and a different color than the holes not covered by suspended graphene. This is a different sample than that shown in Fig. 2.1

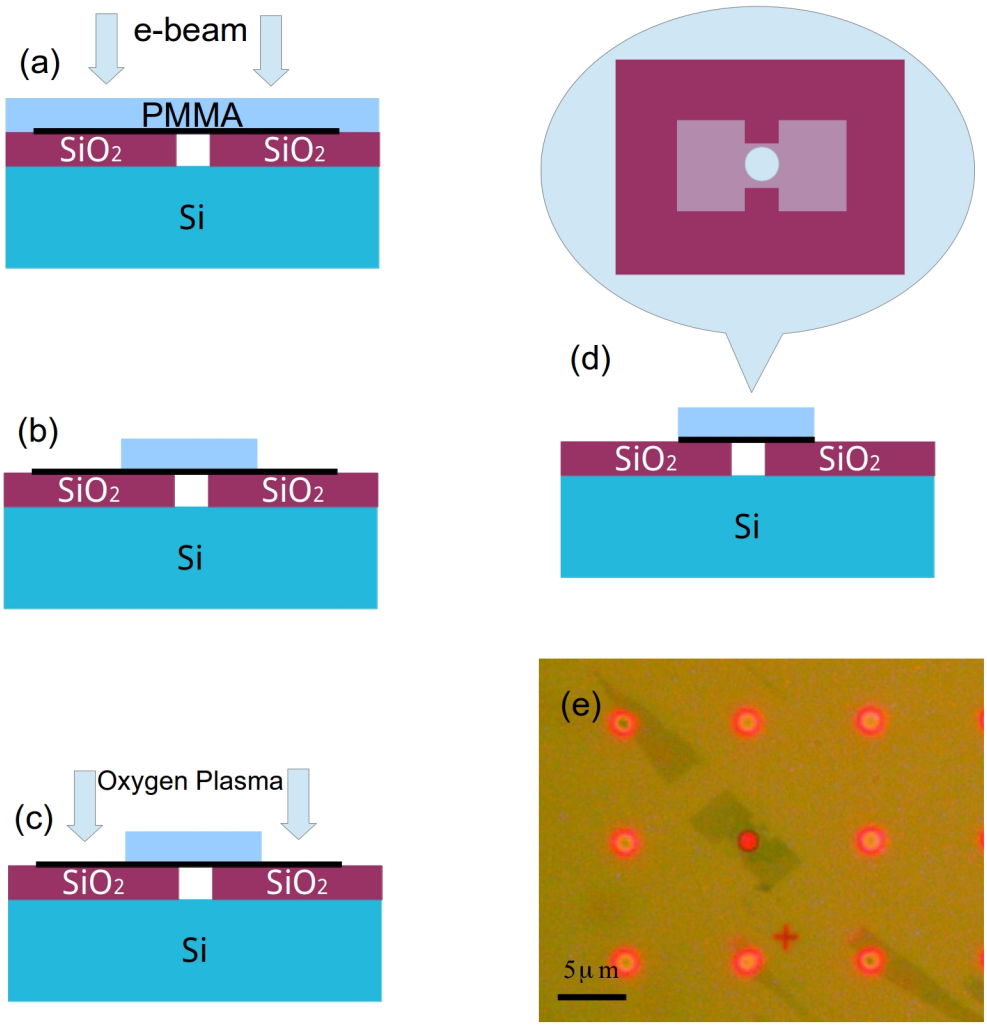

Figure 2.3: Fabrication procedure for tailoring the graphene. (a) E-beam lithography is used to expose the PMMA on top of the unwanted graphene. (b) The exposed PMMA is developed in MIBK/IPA (1:3) for 65 seconds leaving the unwanted graphene exposed to air. (c) Oxygen plasma is used to etch the exposed graphene. (d) Schematic diagram of tailored graphene. (e) Optical image of a multi-layer graphene drum in Fig. 2.2 tailored into a certain shape, covered with the PMMA resist.

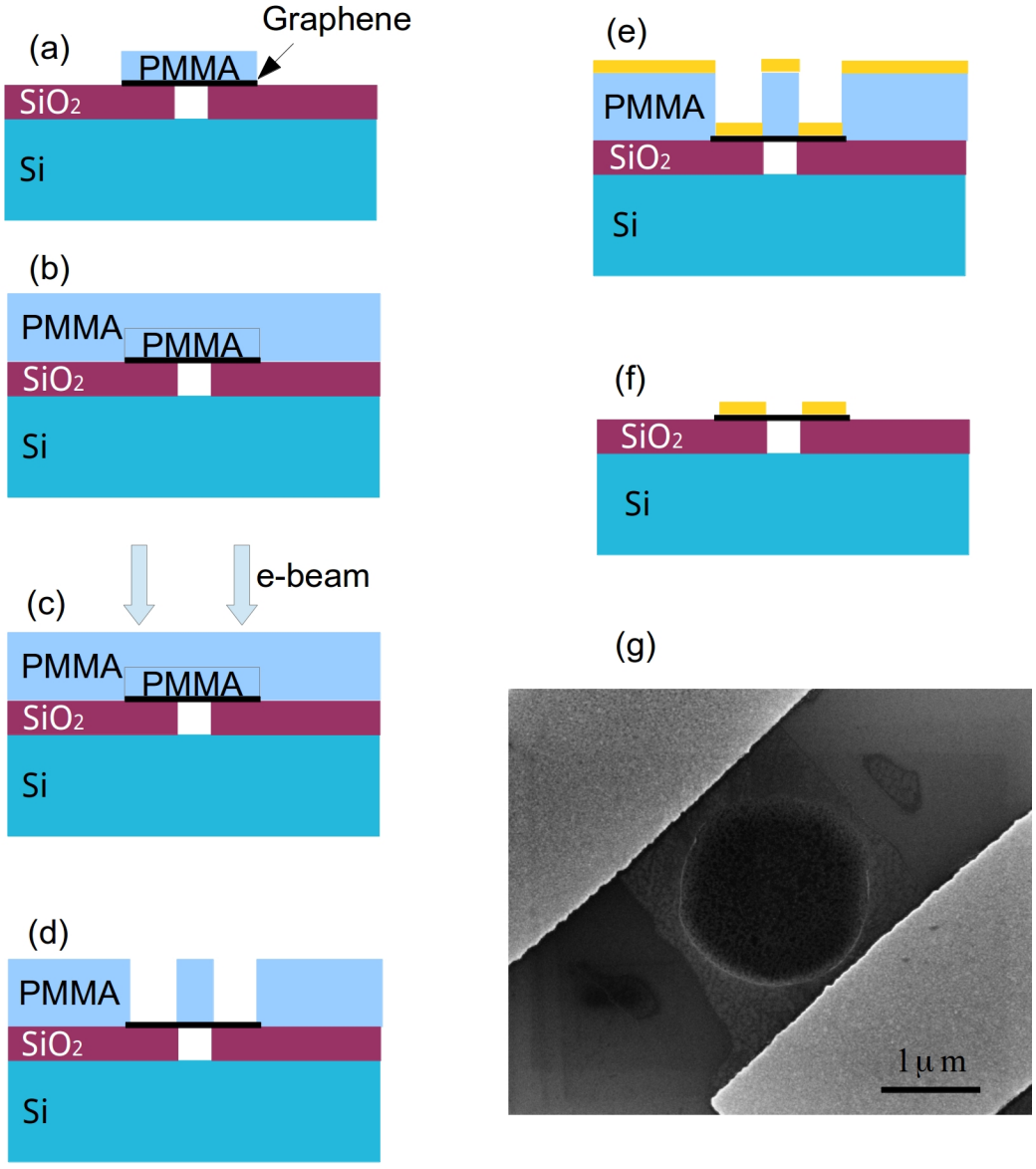

Figure 2.4: Fabrication procedure for the electrodes. (a) After oxygen plasma etching, the PMMA mask is kept on the chip. (b) Another layer of PMMA is spun on the top. (c) The electrode patterns are defined by e-beam lithography. (d) The PMMA is developed. (e) The Ti/Au electrodes are deposited by e-beam evaporation. (f) Lift-off process is done in acetone at 60 °C for 15 minutes. (g) Scanning Electron Microscope (SEM) image of the final device.

2.3 Drum Resonator Made by CVD Grown Graphene

The advantage of using the mechanically exfoliated graphene is they usually have better quality as compared to the CVD grown graphene. The drawback is it is very difficult to get a monolayer graphene landing on a hole by random deposition. However, with the CVD grown graphene, we can easily get a monolayer graphene and the fabrication yield can be significantly improved. So we also developed a procedure for fabricating graphene drum resonators using the monolayer CVD grown graphene.

The idea is to make arrays of predefined holes and electrodes on a chip, and then transfer CVD grown monolayer graphene onto the chip. The last step is to etch the graphene into small rectangles and form a device for etch hole.

First, we prepare a silicon chip with 290nm of oxide (SiO_2). Here, we use the E-beam Direct Write Lithography System (JBX-5500FS) to write patterns on the e-beam resist for the electrodes. After e-beam lithography and development, the chip is placed in the buffered oxide etch for 30 seconds. This is to etch a trench for the electrodes with a depth of about 50 nm. Then we use e-beam evaporator to deposit 5 nm of Ti and 45 nm of Au in to the trench. This makes the electrodes at about the same height as the oxide surface so that it becomes easier to transfer the graphene onto the chip. After that, we use the e-beam writer again to write holes with a diameter of 1.4 μm and use BOE to etch the SiO_2 for 200 seconds. The 290 nm of oxide should all be etched away.

Now we have a chip with arrays of predefined electrodes and holes. The next step is to transfer the CVD graphene which is grown on a copper foil onto the chip. Here we use a thermal release tape (NITTO DENKO)[20, 21] to assist the transferring. We first attach a piece of thermal release tape to the graphene on copper and gently apply

a force on it to ensure they conform without bubbles. Then we use HCl/H_2O_2 solution to dissolve the copper foil, leaving the gaphene on the thermal release tape. Then we rinse the tape/graphene in the DI water. The tape/graphene is then transferred and gently pressed onto the chip with the predefined electrodes and holes. The chip with the graphene/tape is then placed on a hot plate at 95 °C, so that the tape can be easily peeled off because it loses adhesion. There is usually tape residue left on the chip. The next step is to etch the graphene into small rectangles. Here we choose a negative e-beam resist, ma-N2403 to define the etch mask. In order to minimize the chance of collapsing the suspended graphene, we spin coat the ma-N2403 resist at a slow speed (1000 rpm) for 30 seconds and ramp-up rate at 100 rpm/s. We still use the spin coating here because the CVD graphene sheets are much larger than the mechanical exfoliated graphene sheets and they are less likely to collapse than the small exfoliated graphene. Then we bake the resist at 90 °C for 1 minute. We use the e-beam direct writer to write the etch mask, and use the ma-D525 developer to develop the resist for 2 minutes. The e-beam exposed resist remains on the chip and the unexposed resist is dissolved. After the development, we can see there is more resist residue left on the chip probably because the tape residue tends to attract the resist residue. Then, we treat the chip with the oxygen plasma to etch the graphene into rectangles. After that, the etch mask is dissolved in the Remover PG (a proprietary NMP based solvent stripper) at 65 °C for 15 minutes, and the chip is placed in IPA. A critical point drying process is followed to reduce the chance of collapsing the suspended graphene by liquid surface tension. The final step is to anneal the chip in H_2/Ar (0.2/0.4 SLM) at 220 °C for 2 hours to clean the sample. Then we look for good devices on the chip under SEM. Now we have a chip with many monolayer graphene resonators ready for the measurement.

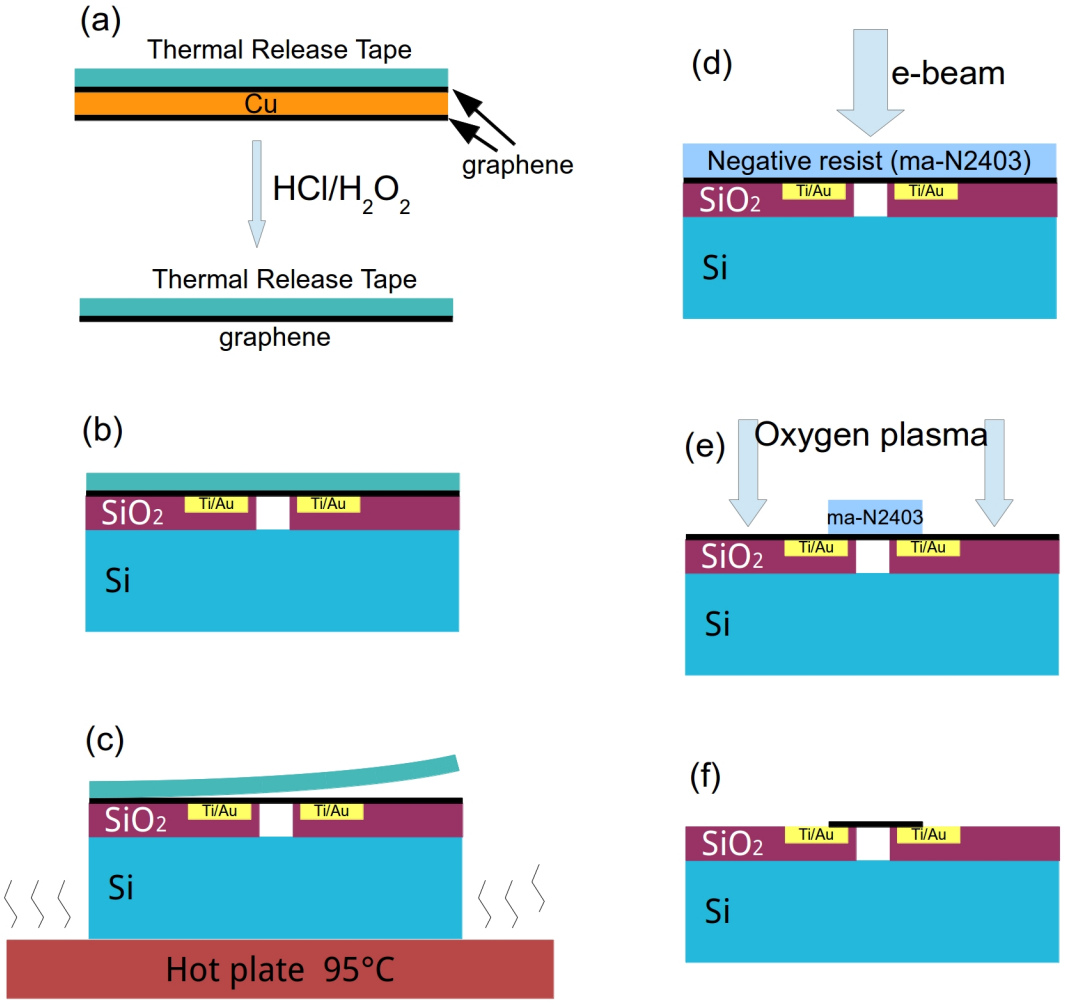

Figure 2.5: Fabrication procedure for the CVD graphene drum resonators. (a) A piece of thermal release tape is attached to the graphene on copper foil, and the copper is dissolved by HCl/H_2O_2 solution. (b) The tape/graphene is then transferred and gently pressed onto the chip with the predefined electrodes and holes. (c) The chip with graphene/tape is then placed on a hot plate at 95 °C, and the tape can be easily peeled off. (d) A negative e-beam resist ma-N2403 is spun on with a slow speed. The resist in a rectangular area around the hole is then exposed by e-beam. (e) The unexposed area of the resist is developed by the developer ma-D525. The oxygen plasma then is used to etch the unwanted graphene. (f) The etch mask is dissolved in Remover PG at 65 °C for 15 minutes, followed by a critical point drying and H_2/Ar (0.2/0.4 SLM) annealing at 220 °C for 2 hours.

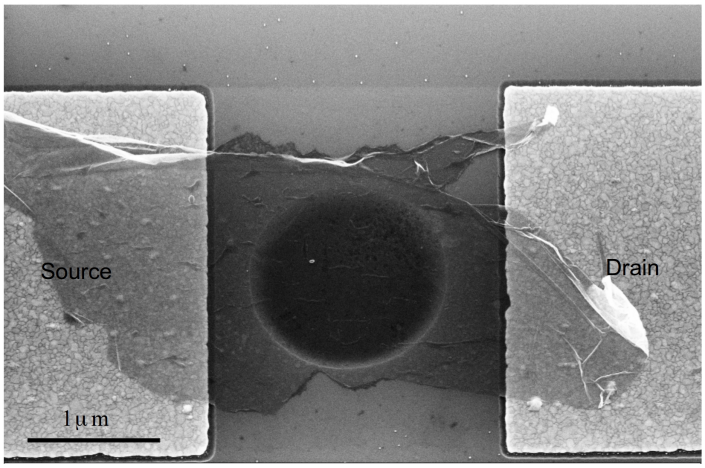

Figure 2.6: SEM image of a CVD graphene drum resonator. The shape of graphene is torn into a non-rectangular shape during the fabrication process.

2.4 Electrical Actuation

The graphene and doped silicon or metal gates form a parallel plate capacitor. By varying the relative voltage difference between graphene and gate, we can vary the electric field on graphene which will result in a change in the electrostatic force on graphene. Performing this at the resonance frequency can actuate the resonance.

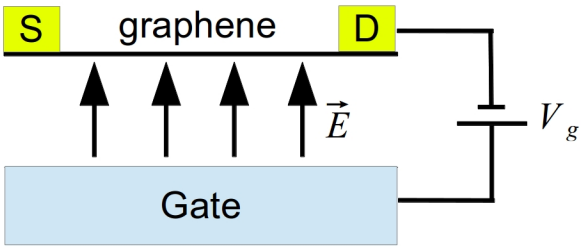

Figure 2.7: Diagram of a parallel plate capacitor formed by the graphene and the gate.

To derive the electrostatic force between the gate and graphene, here we start with the electrostatic energy stored in the system. We can easily get the electrostatic

energy:

$$U_{es} = \frac{1}{2} C V_g^2, \tag{2.1}$$

where C is the parallel plate capacitance and V_g is the gate voltage. The charge on the graphene is

$$Q = -CV_g. \tag{2.2}$$

If now the graphene changes its position by dz, the work done to the system by the battery is $-V_g dQ = dCV_g^2$. The change of the total energy of the system is:

$$dE = dU_{es} - dCV_g^2 = -\frac{1}{2} dCV_g^2. \tag{2.3}$$

Then the electrostatic force acting on the graphene is

$$F_{es} = -\frac{dE}{dz} = \frac{1}{2}\frac{dC}{dz} V_g^2. \tag{2.4}$$

If we apply a small ac voltage in addition to the dc gate voltage,

$$F_{es} = \frac{1}{2}\frac{dC}{dz}(V_g + \tilde{V}_g)^2. \tag{2.5}$$

The ac driving force is

$$\tilde{F}_{es} = \frac{dC}{dz} V_g \tilde{V}_g. \tag{2.6}$$

Instead of applying an ac gate voltage, We could also apply a small ac source-drain voltage to actuate the resonance. The effective potential on the graphene is $\frac{1}{2}\tilde{V}_{sd}$, so the electrostatic force is

$$F_{es} = \frac{1}{2}\frac{dC}{dz}(V_g - \frac{1}{2}\tilde{V}_{sd})^2, \tag{2.7}$$

Then the ac driving force has an extra factor of 1/2:

$$\tilde{F}_{es} = -\frac{1}{2}\frac{dC}{dz} V_g \tilde{V}_{sd}. \tag{2.8}$$

2.5 Electrical readout

The electrical readout of the mechanical resonance signal is feasible because the conductance of the graphene is tunable by the charge density in the graphene. The charge density is tunable by the the gate capacitance, and the gate capacitance is tunable by the distance between the gate and graphene. So overall, the conductance is tunable by the displacement of graphene. Direct readout of the change of conductance at the resonance frequency ($\sim$ 100 MHz for graphene resonators) is difficult for for the following reason. The characteristic impedance of transmission line is $50\,\Omega$ and the typical value for the device resistance is $\sim$ kΩ, so the the signal is always divided by a factor of approximately $1\text{k}/50 = 20$ or even more. In our experiments, we decided to use the electrical mixing technique to readout the mechanical resonance signal. There are several ways to do the electrical mixing. They can generally be categorized: the two source method (two RF sources are involved) [22, 5, 23] and one source methods[24, 25, 8, 10].

For the two source method, an ac signal with frequency ω is applied to the gate and an ac signal with frequency $\omega + \omega_L$ is applied to source electrode. ω is on the order of MHz and should be close to the mechanical resonance frequency and ω_L is on the order of kHz (typically 1 kHz). Then we collect the low frequency (ω_L) current at the drain electrode.

For one source methods, we either send an amplitude modulation (AM) signal or a frequency modulation (FM) signal to the source electrode and collect the low frequency current at the drain electrode.

2.6 Two Source Mixing

Previous works have used two source mixing technique to study the mechanical resonance of carbon nanotubes [22, 5] and graphene [23]. In this section, we will go through the mechanism for the two source mixing technique.

We can write the total current at drain electrode as:

$$I = G\tilde{V}_{sd} \tag{2.9}$$

G is the conductivity, which is a function of the charge q in the graphene. The charge q depends on the gate voltage V_g and the displacement of graphene z. So we can write the conductance as

$$G(V_g, z) = G(V_g^{dc}, z_s) + \frac{\partial G}{\partial q}\frac{\partial q}{\partial V_g}\tilde{V}_g + \frac{\partial G}{\partial q}\frac{\partial q}{\partial z}\tilde{z}. \tag{2.10}$$

Since

$$\frac{\partial G}{\partial q} = \frac{1}{C}\frac{\partial G}{\partial V_g}, \quad \frac{\partial q}{\partial V_g} = C, \quad \frac{\partial q}{\partial z} = V_g\frac{\partial C}{\partial z}, \tag{2.11}$$

we have

$$G(V_g, z) = G(V_g^{dc}, z_s) + \frac{\partial G}{\partial V_g}\tilde{V}_g + \frac{\partial G}{\partial V_g}V_g^{dc}\frac{C'}{C}\tilde{z}. \tag{2.12}$$

The ac gate voltage is

$$\tilde{V}_g = \delta V_g \cos(\omega t). \tag{2.13}$$

The displacement z has an extra phase relative to the gate voltage determined by eq. 1.10:

$$\tilde{z} = \delta z \cos(\omega t + \phi_M). \tag{2.14}$$

The source-drain voltage has a frequency detuned by ω_L from the frequency of the gate voltage, and an extra phase. The extra phase ϕ_E is possibly due to the different cable lengths[26], and some other unknown factors.

$$\tilde{V}_{sd} = \delta V_{sd} \cos(\omega t + \omega_L t + \phi_E). \tag{2.15}$$

The low frequency mixing current is

$$\tilde{I}^{\omega_L} = \frac{1}{2}\frac{\partial G}{\partial V_g}\delta V_g \delta V_{sd}\cos(\omega_L t + \phi_E) + \frac{1}{2}\frac{\partial G}{\partial V_g}V_g^{dc}\frac{C'}{C}\delta V_{sd}\delta z\cos(\omega_L t + \phi_E - \phi_M). \quad (2.16)$$

It can also be expressed with $\mathrm{Re}(\delta^* z)$ and $\mathrm{Im}(\delta^* z)$:

$$\begin{aligned}\tilde{I}^{\omega_L} &= \frac{1}{2}\frac{\partial G}{\partial V_g}\delta V_g \delta V_{sd}\cos(\omega_L t + \phi_E) \\ &+ \frac{1}{2}\frac{\partial G}{\partial V_g}V_g^{dc}\frac{C'}{C}\delta V_{sd}[\mathrm{Re}(\delta^* z)\cos(\omega_L t + \phi_E) + \mathrm{Im}(\delta^* z)\sin(\omega_L t + \phi_E)],\end{aligned} \quad (2.17)$$

where $\delta^* z$ is the complex displacement of graphene, $\mathrm{Re}(\delta^* z) = \delta z\cos(\phi_M)$ is the real part of the complex displacement and $\mathrm{Im}(\delta^* z) = \delta z\sin(\phi_M)$ is the imaginary part.

The first term in eq. 2.17 is a pure electrical signal, which looks like a background signal. The second term is related to the mechanical resonance of graphene and is on top of the background signal. Fig. 2.8 plots the data of our graphene drum resonator. Fig. 2.8a shows the mixing current (magnitude R) vs. frequency and gate voltage. The resonance frequency is tunable by the gate voltage due to the change of tension and electrostatic softening effect. The tunability of the frequency is a signature of the mechanical resonances and it helps us to identify them. Details will be discussed latter in this thesis. Fig. 2.8b shows a line trace when $V_g = 10$V, which indicates a resonance near 60MHz.

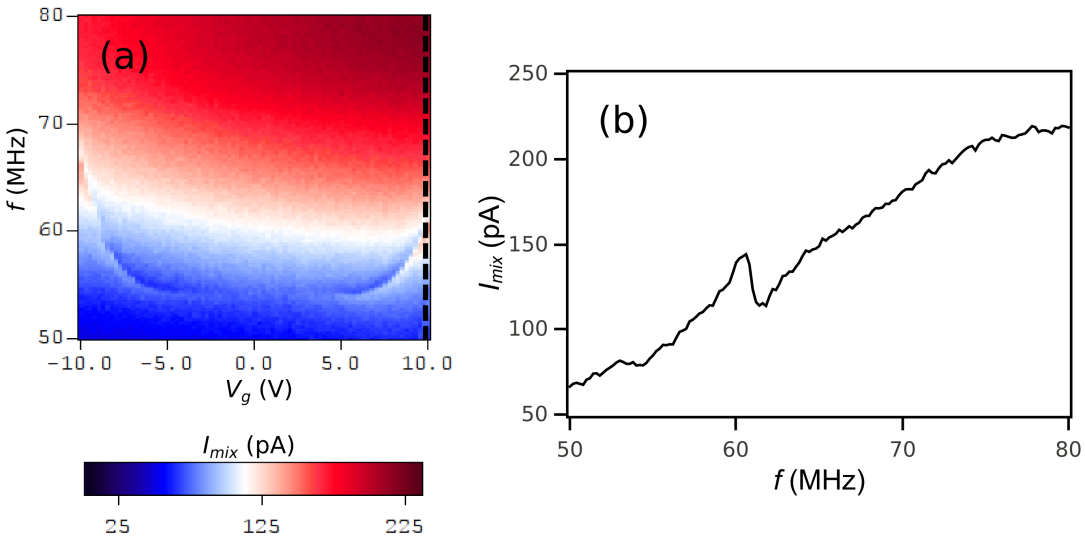

Figure 2.8: Two source mixing signal of a few-layer graphene drum resonator with diameter of 2μm (device T2). $\delta V_{sd} = 18\text{mV}$, $\delta V_g = 18\text{mV}$, $\omega_L = 2\pi \times 1.39\text{kHz}$, Temperature = 296K. (a) Mixing signal vs. frequency and gate voltage. (b) Mixing signal (magnitude R) vs. frequency at $V_g = 10\text{V}$.

Ref. [26] also described a method to measure the amplitude of the resonance. Here is the detail of the method. Instead of measuring the magnitude R in the lock-in amplifier, we could also measure the in phase signal X and the quadrature signal Y. They are related to the magnitude by

$$X = R\cos(\theta), \tag{2.18}$$

and

$$Y = R\sin(\theta), \tag{2.19}$$

where θ is the phase of the lock-in amplifier's input signal (including both the electrical background part and the mechanical part) relative to the reference signal. θ can also be tuned by the phase of the lock-in amplifier. We could properly tune the phase of the lock-in amplifier, so that Y becomes zero when ω is away from ω_0. This means the

electrical background signal is in phase with the reference signal now. Then the $\mathrm{Re}(\delta^* z)$ term in eq. 2.17 should not show up in Y at the resonance frequency either. Then Y at the resonance frequency should be equal to the $\mathrm{Im}(\delta^* z)$ term. Given that the phase $\phi_M = -\pi/2$ at the resonance frequency, we should have $|\mathrm{Im}[\delta^* z(\omega_0)]| = \delta z(\omega_0)$.

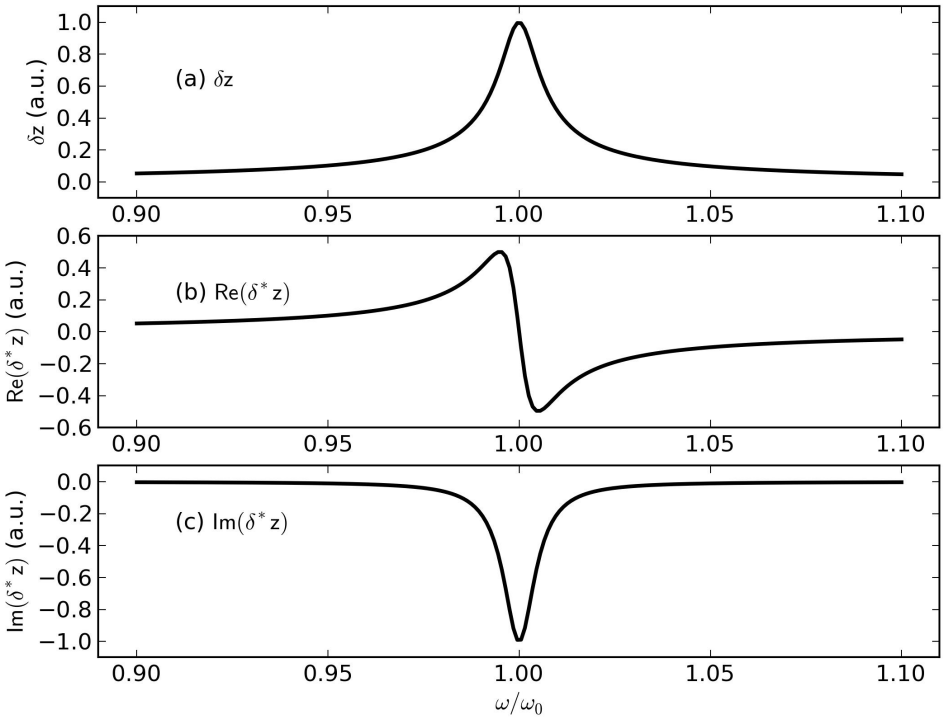

Figure 2.9: Simulation of the line shapes for the two source mixing. (a) Simulation of the Lorentzian line shape of the amplitude δz vs. frequency ω. (b) Simulation of the line shape of $\mathrm{Re}(\delta^* z)$ vs. ω. (c) Simulation of the line shape of $\mathrm{Im}(\delta^* z)$ vs. ω.

2.7 Amplitude Modulation Mixing

The amplitude modulation mixing technique is also an often used technique to study the mechanical resonance of graphene and carbon nanotube devices. [24, 25]. The idea is to apply an amplitude modulated (AM) signal as a source-drain voltage, and for simplicity assume the modulation is 100%:

$$\tilde{V}_{sd} = \delta V_{sd}[1 + \cos(\omega_L t)]\cos(\omega t). \tag{2.20}$$

The ac driving force is

$$\begin{aligned}\tilde{F} &= -\frac{1}{2}C'V_g^{dc}\tilde{V}_{sd} \\ &= -\frac{1}{2}C'V_g^{dc}\delta V_{sd}[1+\cos(\omega_L t)]\cos(\omega t). \end{aligned} \tag{2.21}$$

From eq. 1.14, we can get the displacement of graphene $\tilde{z}$:

$$\tilde{z} = \delta z(\omega_i)[1+\cos(\omega_L t)]\cos(\omega t+\phi_M), \tag{2.22}$$

where

$$\delta z(\omega_i) = \frac{F_0/m}{\sqrt{(\omega_0^2-\omega_i^2)^2+(\omega_i\omega_0/Q)^2}}, \tag{2.23}$$

$F_0 = -\frac{1}{2}C'V_g^{dc}\delta V_{sd}$, and ϕ_M is the phase of the mechanical response relative to the driving force.

Here we follow ref. [8] to do a Taylor expansion of the current with respect to $\tilde{V}_{sd}$ and $\tilde{z}$:

$$I = \frac{\partial I}{\partial V_{sd}}\tilde{V}_{sd} + \frac{\partial I}{\partial z}\tilde{z} + \frac{1}{2}\frac{\partial^2 I}{\partial V_{sd}^2}\tilde{V}_{sd}^2 + \frac{\partial^2 I}{\partial V_{sd}\partial z}\tilde{V}_{sd}\tilde{z} + \frac{1}{2}\frac{\partial^2 I}{\partial z^2}\tilde{z}^2. \tag{2.24}$$

In the above equation, $\frac{\partial I}{\partial V_{sd}}\tilde{V}_{sd}$ and $\frac{\partial I}{\partial z}\tilde{z}$ has no low frequency component at ω_L. $\frac{1}{2}\frac{\partial^2 I}{\partial z^2}\tilde{z}^2$ is zero because of no dc source-drain voltage. Let us check $\frac{1}{2}\frac{\partial^2 I}{\partial V_{sd}^2}\tilde{V}_{sd}^2$ and $\frac{\partial^2 I}{\partial V_{sd}\partial z}\tilde{V}_{sd}\tilde{z}$:

$$\begin{aligned}\frac{1}{2}\frac{\partial^2 I}{\partial V_{sd}^2}\tilde{V}_{sd}^2 &= \frac{1}{2}\frac{\partial^2 I}{\partial V_{sd}^2}\delta V_{sd}^2[1+\cos(\omega_L t)]^2\cos^2(\omega t) \\ &= \frac{1}{2}\frac{\partial^2 I}{\partial V_{sd}^2}\delta V_{sd}^2[1+2\cos(\omega_L t)+\cos^2(\omega_L t)]\frac{1}{2}[1+\cos(2\omega t)]. \end{aligned} \tag{2.25}$$

So the component in the above equation at ω_L is $\frac{1}{2}\frac{\partial^2 I}{\partial V_{sd}^2}\delta V_{sd}^2\cos(\omega_L t)$.

$$\begin{aligned}&\frac{\partial^2 I}{\partial V_{sd}\partial z}\tilde{V}_{sd}\tilde{z} \\ &= \frac{\partial^2 I}{\partial V_{sd}\partial z}\delta V_{sd}[1+\cos(\omega_L t)]\cos(\omega t)\delta z(\omega_i)[1+\cos(\omega_L t)]\cos(\omega t+\phi_M) \\ &= \frac{1}{2}\frac{\partial^2 I}{\partial V_{sd}\partial z}\delta z(\omega_i)\delta V_{sd}[1+2\cos(\omega_L t)+\cos^2(\omega_L t)][\cos(\phi_M)+\cos(2\omega t+\phi_M)]. \end{aligned} \tag{2.26}$$

The component at ω_L is:

$$\frac{\partial^2 I}{\partial V_{sd}\partial z}\delta V_{sd}\delta z(\omega_i)\cos(\omega_L t)\cos(\phi_M) = \frac{\partial^2 I}{\partial V_{sd}\partial z}\delta V_{sd}\mathrm{Re}(\delta^* z). \tag{2.27}$$

The total current at ω_L is:

$$I^{\omega_L} = \frac{1}{2}\frac{\partial^2 I}{\partial V_{sd}^2}\delta V_{sd}^2\cos(\omega_L t) + \frac{\partial^2 I}{\partial V_{sd}\partial z}\delta V_{sd}\mathrm{Re}(\delta^* z)\cos(\omega_L t). \tag{2.28}$$

The first term in the right hand side of the above equation is purely electrical background which does not depends on the motion of the resonator. The coefficient $\frac{\partial^2 I}{\partial V_{sd}^2}$ is related to the nonlinearity of I vs. V_{sd}. The second term is related to the mechanical motion $\tilde{z}$. The coefficient $\frac{\partial^2 I}{\partial V_{sd}\partial z} = \frac{\partial G}{\partial V_g}V_g^{dc}\frac{C'}{C}$. So the mixing current is:

$$I^{\omega_L} = \frac{1}{2}\frac{\partial^2 I}{\partial V_{sd}^2}\delta V_{sd}^2\cos(\omega_L t) + \frac{\partial G}{\partial V_g}V_g^{dc}\frac{C'}{C}\delta V_{sd}\mathrm{Re}(\delta^* z)\cos(\omega_L t). \tag{2.29}$$

Here if neglect the nonlinearity of I vs. V_{sd}, the coefficient in the first term $\partial^2 I/\partial V_{sd}^2$ should come from the fact that changing the potential of the graphene also changes the relative gate voltage which changes the conductance of the graphene.

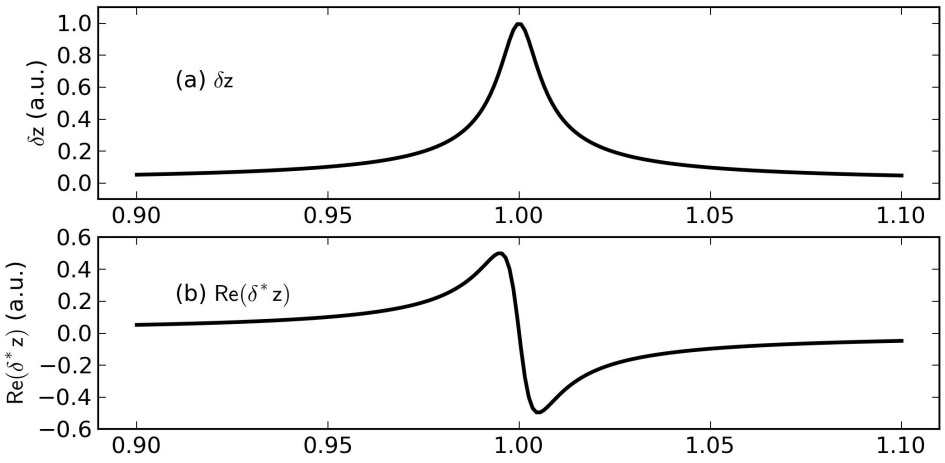

Figure 2.10: Simulation of line shapes. (a) Simulation of the Lorentzian line shape of amplitude δz vs. frequency ω. (b) Simulation of Line shape of $\mathrm{Re}(\delta^* z)$ vs. ω.

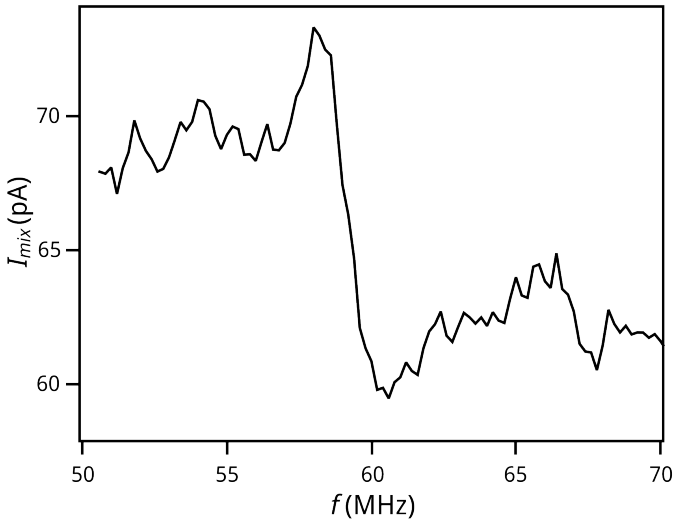

Figure 2.11: AM mixing signal vs. frequency of a few-layer graphene drum resonator with diameter of 2 μm.

2.8 Frequency Modulation Mixing

The frequency modulation (FM) mixing is a powerful and easy-to-use technique, which requires a much simpler measurement setup than the two source mixing technique. An even more important advantage of this technique is when the frequency is at off resonance, the background in the signal should be zero in principle. This makes life much easier when we want to identify the mechanical resonance signal. It is widely used by various works, for example ref. [8, 10]. Here we follow ref. [8] to go over the mechanism of this technique. The idea is to apply a FM signal as the source-drain voltage:

$$\tilde{V}_{sd} = \delta V_{sd} \cos(\omega_c t + \frac{\omega_\Delta}{\omega_L} \sin(\omega_L t)), \tag{2.30}$$

where ω_c is the carrier's base frequency which is on the order of the mechanical resonance frequency of our graphene devices, from 50 MHz to a few hundred MHz. ω_L is the modulation frequency, typically at 1 kHz in our experiments. ω_Δ controls how much the

frequency is modulated, typically from 10 kHz to 200 kHz in our experiments depending on the condition which we will discuss about later.

The ac source-drain voltage provides a ac driving force to the device as shown in eq. 2.8:

$$\tilde{F} = -\frac{1}{2}C'V_g^{dc}\tilde{V}_{sd}, \tag{2.31}$$

Let's first look at $\tilde{V}_{sd}$. It can be expressed as follows:

$$\tilde{V}_{sd} = \delta V_{sd}\cos(\phi(t) + \omega_i \Delta t), \tag{2.32}$$

Here Δt is smaller or on the order of the timescale of the mechanical resonance Q/ω_0, where Q is the quality factor of the resonator. Also the modulation of frequency should at a sufficiently slow frequency ω_L. That means $1/\omega_L$ should be much longer than the timescale of the resonance Q/ω_0 so that we do not measure the transient oscillation of the resonator. Within the timescale of Δt, the ac driving force is at the instantaneous frequency ω_i with a constant phase $\phi(t)$. [8]:

$$\tilde{F} = F_0\cos(\phi(t) + \omega_i \Delta t), \tag{2.33}$$

where the instantaneous frequency is

$$\omega_i = \omega_c + \omega_\Delta \cos(\omega_L t), \tag{2.34}$$

and magnitude $F_0 = -\frac{1}{2}C'V_g^{dc}\delta V_{sd}$.

The ac source-drain voltage also drives a current through device. We do a Taylor expansion of the current with respect to $\tilde{V}_{sd}$ and $\tilde{z}$, similar to the AM mixing technique:

$$I = \frac{\partial I}{\partial V_{sd}}\tilde{V}_{sd} + \frac{\partial I}{\partial z}\tilde{z} + \frac{1}{2}\frac{\partial^2 I}{\partial V_{sd}^2}\tilde{V}_{sd}^2 + \frac{\partial^2 I}{\partial V_{sd}\partial z}\tilde{V}_{sd}\tilde{z} + \frac{1}{2}\frac{\partial^2 I}{\partial z^2}\tilde{z}^2. \tag{2.35}$$

With similar reason as in the AM technique, the first, second and last term has no components at ω_L. It can also be shown that the third term $\frac{1}{2}\frac{\partial^2 I}{\partial V_{sd}^2}\tilde{V}_{sd}^2$ has no component at ω_L because $\tilde{V}_{sd}$ is a FM signal. [8] Then the only term left is $\frac{\partial^2 I}{\partial V_{sd}\partial z}\tilde{V}_{sd}\tilde{z}$, and it is related to the mechanical motion of the resonator.

Let's check $\tilde{z}\tilde{V}_{sd}$:

$$\begin{aligned}\tilde{z}\tilde{V}_{sd} &= \delta z(\omega_i)\cos(\omega_i\Delta t+\phi(t)+\phi_M)\delta V_{sd}\cos(\omega_i\Delta t+\phi(t))\\ &= \frac{1}{2}\delta z(\omega_i)\delta V_{sd}[\cos(\phi_M)+\cos(2\omega_i\Delta t+2\phi(t)+\phi_M)]\\ &= \frac{1}{2}\mathrm{Re}(\delta^* z)\delta V_{sd}+\frac{1}{2}\delta z(\omega_i)\delta V_{sd}\cos(2\omega_i\Delta t+2\phi(t)+\phi_M)\end{aligned} \tag{2.36}$$

Here $\delta^* z$ is complex amplitude of the displacement, and we have $\delta z = |\delta^* z|$. From eq. 1.14, we have:

$$\mathrm{Re}(\delta^* z) = \frac{(\omega_0^2-\omega_i^2)F_0/m}{(\omega_0^2-\omega_i^2)^2+(\omega_i\omega_0/Q)^2}, \tag{2.37}$$

where ω_0 is the intrinsic mechanical resonance frequency, Q is the quality factor. From eq. 2.34 we know that ω_i is slowly modulated at frequency ω_L with an amplitude modulation of ω_Δ. As a result, $\mathrm{Re}(\delta^* z)$ should also be modulated at frequency ω_L. Because $\omega_\Delta << \omega_c$, we can do a Taylor expansion of $\delta z(\omega_i)$ to the first order of $\omega_\Delta\cos(\omega_L t)$:

$$\mathrm{Re}(\delta^* z) = \mathrm{Re}(\delta^* z)|_{\omega=\omega_c} + \frac{\partial \mathrm{Re}(\delta^* z)}{\partial\omega}\omega_\Delta\cos(\omega_L t). \tag{2.38}$$

By plugging eq. 2.36 and eq. 2.38 into eq. 2.35, we can get the low frequency current at ω_L:

$$I^{\omega_L} = \frac{1}{2}\frac{\partial G}{\partial V_g}V_g^{dc}\frac{C'}{C}\delta V_{sd}\frac{\partial \mathrm{Re}(\delta^* z)}{\partial\omega}\omega_\Delta\cos(\omega_L t). \tag{2.39}$$

Fig. 2.12 (c) shows the simulation of the line shape of lock-in amplifier's in-phase signal of a mechanical resonance by FM mixing technique. Fig. 2.12 (d) shows the simulation if we choose to measure the magnitude R instead of the in-phase signal X in the lock-in amplifier. Fig. 2.13 shows the data of a few-layer graphene drum resonator.

Fig. 2.13(a) shows the magnitude R of the lock-in signal. Figure 2.13(b) shows the phase θ of the lock-in signal. In principle, eq. 2.39 indicates that the lock-in signal should only have in-phase signal X and no quadrature signal Y. Because $X = R\cos(\theta)$ and $Y = R\sin(\theta)$, the phase θ should be 0° or 180°. However, the data shows the phase is a little off 0° or 180°, possibly due to some non-zero background quadrature signal. When it is on resonance, the phase has a 180° change because the in-phase signal X has a sign change. This is also shown in ref. [8].

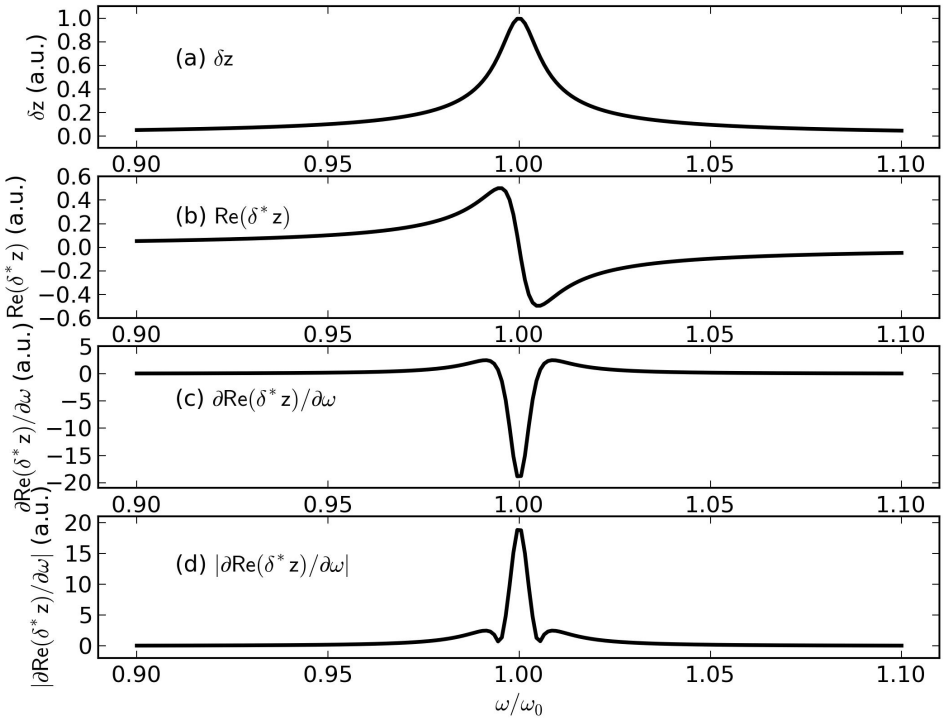

Figure 2.12: Simulation of line shapes for the FM mixing. (a) Simulation of Lorentzian line shape of the amplitude δz vs. frequency ω. (b) Simulation of the line shape of $\mathrm{Re}(\delta^* z)$ vs. ω. (c) Simulation of the line shape of the low frequency mixing current (in-phase signal measured by the lock-in amplifier) for mechanical resonance signal using FM technique: $\partial\mathrm{Re}(\delta^* z)/\partial\omega$ vs. ω. (d) Simulation of the line shape of the magnitude of the signal in (c).

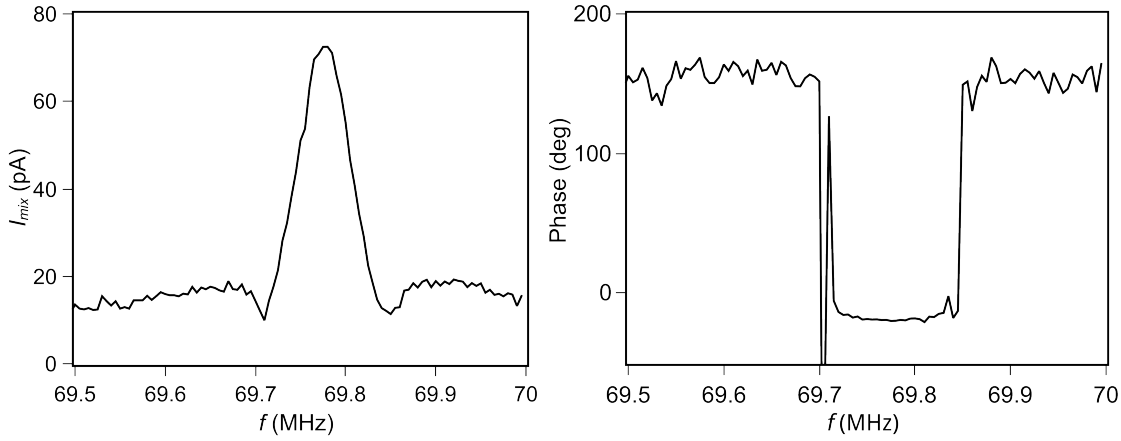

Figure 2.13: Line trace of the mechanical resonance signal using FM technique of a few-layer graphene drum resonator. The lock-in is set to measure the amplitude and phase of the signal. (a) The line trace of the magnitude vs. frequency. (b) The line trace of the phase vs. frequency. The phase has a 180° change due to the sign change of the in-phase signal.

2.9 Measurement of Quality Factor

The quality factor Q can be measured from the FM mixing technique. We denote the distance between the two zeros in the linetraces as Δf and the quality factor $Q = f_0/\Delta f$, where f_0 is the resonance frequency. [8] When the driving is large enough and the nonlinear damping dominates over the linear damping, this measurement of Q is still valid with a slight correction: $Q = 1.09 f_0/\Delta f$. [10]

In order to measure Q correctly, a proper frequency deviation ω_Δ in the formula of the FM signal (eq. 2.30) should be chosen. Since the FM mixing signal I_{mix} is proportional to ω_Δ, ω_Δ should be sufficiently large in order to get a decent signal-to-noise ratio. However when $\omega_\Delta > 2\pi\Delta f$, the measured frequency width is broadened more than the intrinsic width. [8, 10] This is because when the frequency deviation ω_Δ is too large, it is no longer probing $\partial \mathrm{Re}(\delta^* z)/\partial\omega$ at the close vicinity of the carrier frequency ω_c as shown in eq. 2.38. So the strategy for choosing the right ω_Δ is to start

with a large value, usually 200kHz in our cases and then keep decreasing it until the frequency width does not become smaller anymore.

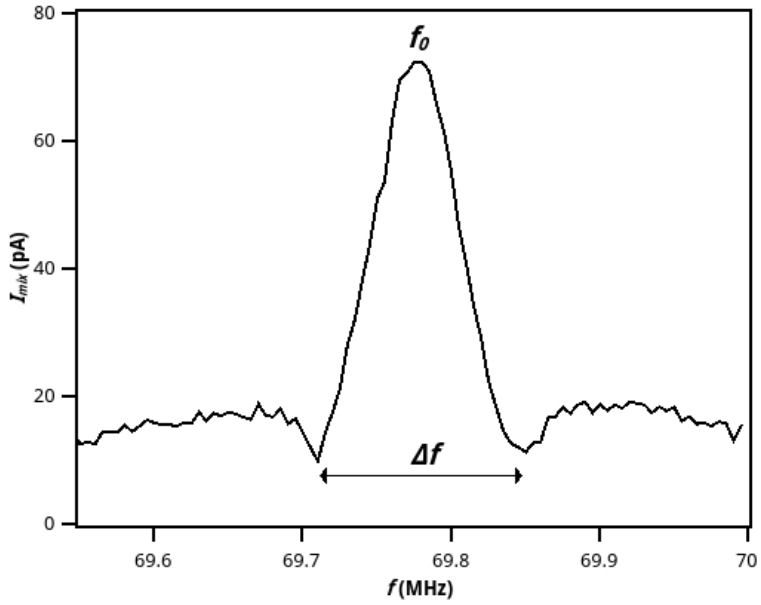

Figure 2.14: Line trace of the FM mixing current vs. frequency of a mechanical resonance. Q is measured by $f_0/\Delta f$.

2.10 Experimental Setup

The experiments were performed in a home built cryostat, the design details can be found in ref. [27]. This cryostat is essentially a dipping probe that can be inserted into the liquid helium dewar. The system can be pumped into high vacuum. We usually perform the experiments in a vacuum condition of $10^{-6} - 10^{-5}$ Torr. The temperature can be varied from room temperature down to liquid helium temperature by changing how much the dipping probe is inserted in the helium dewar. We have two stainless steel semi-rigid coaxial cables with SMA connectors for RF signal and five Manganin wires for dc signal. At the bottom of the probe, there is a customized circuit board for sample mounting.

Our early experiments were performed in the circuit developed in the earlier nanotube mechanical resonator project by Chiu [5]. We used the two source mixing, AM mixing, and FM mixing on this circuit board. Fig. 2.15 shows a two source mixing measurement using this circuit. The characteristic impedance of the coaxial cable that we use is $z_0 = 50\,\Omega$, and the load impedance needs to match $50\,\Omega$ in order to reduce the power reflection at the load. In our case, the typical graphene device resistance is $\sim$ kΩ which is much larger than z_0. Here we need to terminate the device with a $50\,\Omega$ resistor to the ground. By doing so, the total load impedance the input signal sees is about $50\,\Omega$. It should be noted that there is a $1\,\mathrm{k}\Omega$ resistor to the ground, nearby the source electrode. This resistor is connected to a dc wire for dc bias. It is needed because otherwise the impedance for the dc wire at high frequency (50 - 500 MHz) is unknown. With a 1kΩ resistor connected, the impedance is at least 1kΩ and since $1\,\mathrm{k}\Omega >> 50\,\Omega$ it would not affect the total load impedance for V_{sd}^{ac}.

The source and drain bonding pads normally have lateral sizes of $100-250\,\mu$m, and based on the parallel plate capacitor model, the stray capacitances to the global back gate C_s and C_d are $1-7$pF. The impedance of C_s is $X_s = 1/i\omega C_s$. At high frequencies, X_s sets the total load impedance if $X_s \sim z_0$. So the cut-off frequency is

$$f_c = \frac{1}{2\pi z_0 C_s} \approx 450\,\mathrm{MHz} - 3\,\mathrm{GHz}. \tag{2.40}$$

Once the frequency of input signal reaches f_c, we start to get significant reflections in the input signal and the actual power delivered onto the device is less than the input signal.

FM or AM mixing technique can also be used in the same circuit board, with the source electrode connected to a FM or AM signal as shown in Fig. 2.16. Most of the data in my project was taken with the FM mixing in this circuit board. Later, we

adopted a simplified circuit design from ref. [23].The advantage of the new circuit is it takes less electronic elements to make the circuit board as shown in Fig. 2.17.

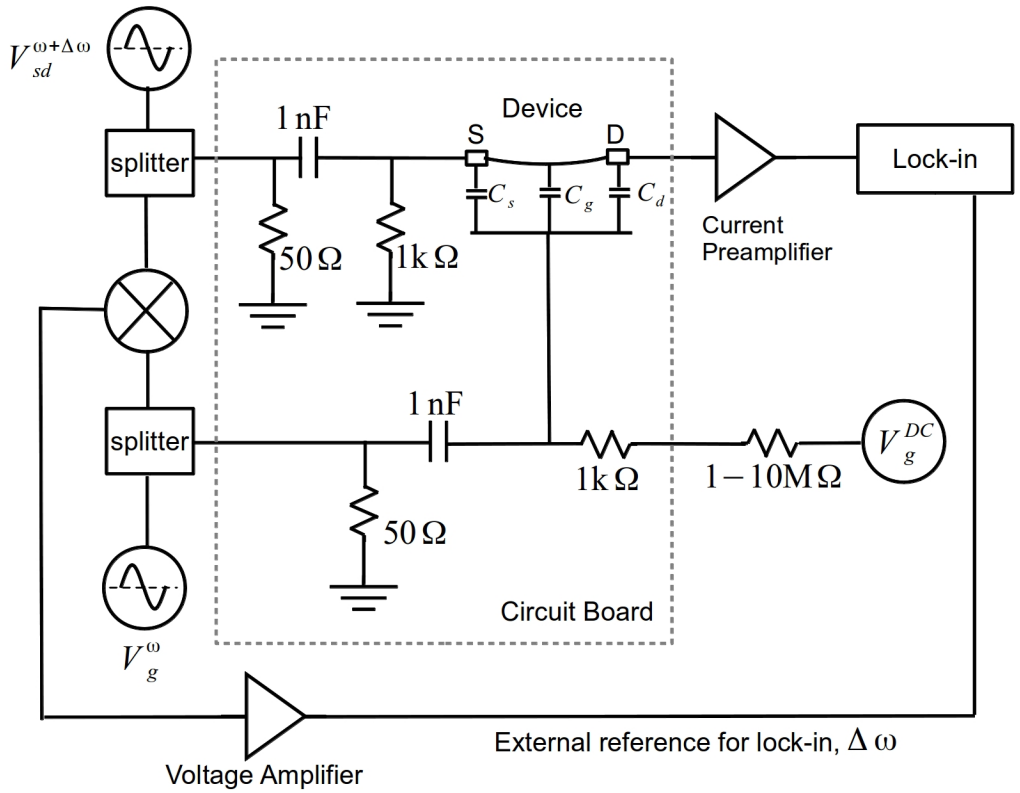

Figure 2.15: Schematic diagram of measurement circuit by by Chiu [27] using two source mixing technique. The function generator's output signal is split into two (with a loss of 3dB). One goes to the device, and the other goes to the mixer. For the device, an ac signal $V_{sd}^{\omega+\Delta\omega}$ at $\omega + \Delta\omega$ is applied to the source electrode. An ac signal V_g^{ω} at ω is applied to the gate. Their mixing signal(at $\Delta\omega$ and $2\omega + \Delta\omega$) goes through a voltage amplifier with a low pass filter. Only the $\Delta\omega$ signal is amplified and sent to the lock-in amplifier as an reference. The drain current is collected by a current preamplifier and then sent to the lock-in amplifier.

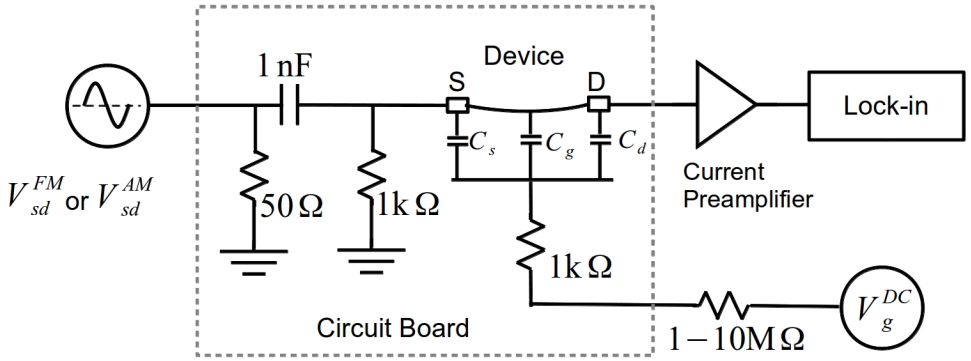

Figure 2.16: Schematic diagram of old measurement circuit by Chiu [27] using FM and AM mixing technique.

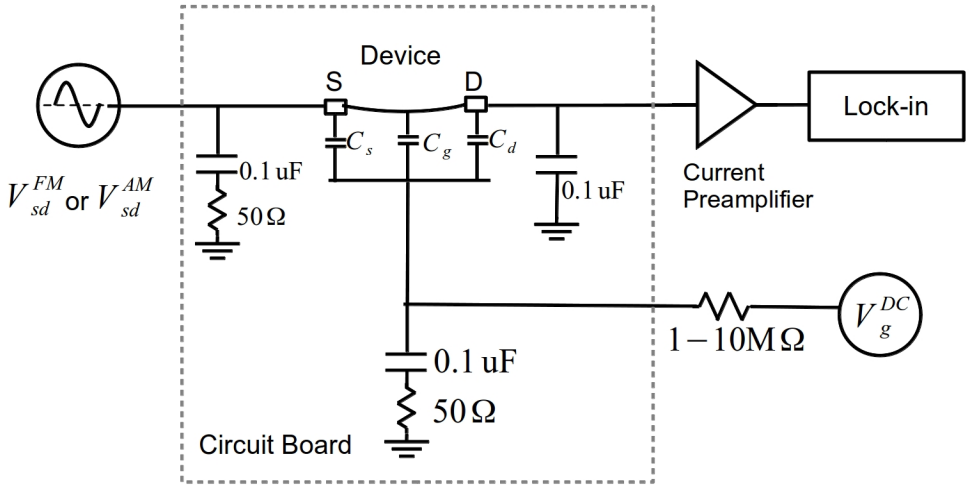

Figure 2.17: Schematic diagram of measurement circuit similar to the circuit in ref. [23]. The ac and dc signals are all applied through the coaxial cable. The 0.1μF capacitor is used to prevent a dc current in the 50Ω resistor which could damage the resistor if the current is large.

Chapter 3

Properties of Graphene Drum Resonators

3.1 Introduction

In this chapter, we will discuss some of the intrinsic properties of graphene drum resonators, including the static and dynamic properties. We will also discuss the magnitude of FM mixing signal of drum resonator considering its difference with the regular parallel plate capacitor model. The contents in this chapter can be found in my previous published work [1].

3.2 Deflection of Graphene Membranes under Electrostatic Pressure

To calculate the resonance frequency of an initially tensioned graphene circular membrane with tension T_0 versus gate voltage V_g, the starting point is the elastic energy for

a two dimensional (2D) membrane, [28, 29]

$$\mathcal{U} = \frac{1}{2}\kappa \int dxdy \left(\nabla^2 h\right)^2 + \frac{1}{2}\int dxdy\, 2\mu \sum_{i,j} u_{ij}^2 + \lambda \left(\sum_i u_{ii}\right)^2 - P\int dxdy\, h, \quad (3.1)$$

where μ is the shear modulus, λ is Lamé's first constant, h is the vertical height displacement of the membrane, P is the pressure on the membrane, κ is the bending modulus, and u_{ij} is the strain tensor. For graphene, $\lambda \approx 48$ N/m, $\mu \approx 144$ N/m, and $\kappa \sim 1$ eV. [30] The strain tensor is given by [29]

$$u_{ij} = \frac{1}{2}\left(\frac{\partial u_i}{\partial x_j} + \frac{\partial u_j}{\partial x_i} + \frac{\partial h}{\partial x_i}\frac{\partial h}{\partial x_j}\right),$$

A vector in the x-y plane with components $u_i(x, y)$, and a z-component $h(x, y)$ represents the displacement of each point on the membrane from equilibrium. To calculate the deflection and resonance frequency of the fundamental mode, we neglect the bending term. [30] The membrane is considered to be initially tensioned by stretching it by an isotropic in-plane strain factor $1 + c$ and then vertically displaced by the pressure. We take a variational approximation to the height to be $h = z_0(1 - r^2/r_0^2)$, where r_0 is the radius of the resonator, r is the cylindrical radius coordinate, and z_0 is a variational parameter equal to the vertical displacement of the center of the membrane. This gives the strain tensor components

$$\begin{aligned} u_{xx} &= 2x^2(z_0/r_0^2)^2 + c \\ u_{yy} &= 2y^2(z_0/r_0^2)^2 + c \\ u_{xy} &= 2xy(z_0/r_0^2)^2 \end{aligned} \quad (3.2)$$

Putting eq. 3.2 into eq. 3.1 gives

$$\mathcal{U} = \frac{2}{3}\pi\frac{z_0^4}{r_0^2}(\lambda + 2\mu) + 2\pi c(\lambda + \mu)z_0^2 - \frac{1}{4}\frac{\epsilon_0 \bar{A}}{d^2} z_0 V_g^2 + 2c^2(\lambda + \mu)\pi r_0^2 \quad (3.3)$$

The term $2c^2(\lambda+\mu)\pi r_0^2$ is a constant arising from the work required to initially strain the membrane, and the electrostatic pressure was expressed as

$$P = \frac{1}{2}\frac{\epsilon_0}{d^2}V_g^2, \tag{3.4}$$

where ϵ_0 is the dielectric constant and d is the distance between the gate and the ground plane. Minimizing the energy with respect to z_0 gives the equation

$$\frac{8}{3}\pi(\lambda+2\mu)\frac{\bar{z}_0^3}{r_0^2} + 4\pi c(\lambda+\mu)\bar{z}_0 - \frac{1}{4}\frac{\epsilon_0\bar{A}}{d^2}V_g^2 = 0, \tag{3.5}$$

where $\bar{A}$ is the area of the resonator, and $\bar{z}_0$ is the optimizing value. For sufficiently small V_g we neglect the cubic terms and get

$$\bar{z}_0 = \frac{1}{4\pi c(\lambda+\mu)}\frac{\epsilon_0\bar{A}}{4d^2}V_g^2. \tag{3.6}$$

The factor $c(\lambda+\mu)$, which is a strain times an elastic constant, is related to the initial tension. As the constant term in the energy, $2c^2(\lambda+\mu)\pi r_0^2$ represents the work required to strain the membrane we use this to determine the tension by considering the work required for an infinitesimal expansion. This yields $T_0 = 2c(\lambda+\mu)$. Thus equation 3.6 is then rewritten as

$$\bar{z}_0 = \frac{1}{8\pi T_0}\frac{\epsilon_0\bar{A}}{d^2}V_g^2. \tag{3.7}$$

For large V_g the cubic term in equation 3.5 dominates, and we expect $\bar{z}_0 \sim V_g^{2/3}$.

3.3 Effective spring constant, mass, and Duffing term

The resonance frequency ω_0 is given by $\omega_0 = \sqrt{k_{eff}/m_{eff}}$ with an effective resonator spring constant k_{eff} and mass m_{eff} . The effective spring constant is given by

$$k_{eff} = \frac{\partial^2\mathcal{U}}{\partial z_0^2},$$

where $\mathcal{U}$ is the total energy including electrostatic terms from the gate voltage. To account for electrostatic effects on ω_0, it is required to approximate the electrostatic energy to 2nd order in z_0 to determine the force gradient. The electrostatic energy is $\frac{1}{2}CV^2$, where C is the resonator capacitance, and V is the voltage on the capacitor. Assuming slow variation of the displacement laterally, we approximate the capacitance as

$$C = \int \frac{\epsilon_0}{d - z_0(1 - r^2/r_0^2)} r dr d\theta$$

Expanding this in a power series in z_0, the maximum deflection, so that $C = C_0 + C_1 + C_2...$, where C_i is a term in the ith power of z_0, gives

$$\begin{aligned} C_0 &= \frac{\epsilon_0 \bar{A}}{d} \\ C_1 &= \frac{\epsilon_0 \bar{A} z_0}{2d^2} \\ C_2 &= \frac{\epsilon_0 \bar{A}}{3d^3} z_0^2 \end{aligned}$$

The contribution to the energy from C_2 produces a force gradient and alters the effective spring constant, yielding

$$k_{eff} = \frac{\partial^2 \mathcal{U}}{\partial z_0^2} = 8\pi(\lambda + 2\mu)\frac{z_0^2}{r_0^2} + 4\pi c(\lambda + \mu) - \frac{\epsilon_0 \bar{A}}{3d^3} V_g^2 \tag{3.8}$$

Using the relation $T_0 = 2c(\lambda + \mu)$ derived above and eq. 3.7, eq. 3.8 can be rewritten as

$$\omega_{res} = 2\pi f_{res} = \sqrt{\frac{2\pi T_0 - \frac{\epsilon_0 \pi r_0^2}{3d^3} V_g^2 + a V_g^4}{m_{eff}}}, \tag{3.9}$$

with a a constant.

Fig. 3.1 shows the resonator frequency tunability, originating from both electrostatic force gradient softening as well as the increase in tension with V_g. [31, 32] The solid curve is a fit using eq. 3.9, yielding the tension T_0 at $V_g = 0$, m_{eff}, and a, which describes the tension increase with V_g. We obtain $T_0 = 6.9 \times 10^{-2}$ N/m, $m_{eff} = 2.5 \times 10^{-18}$ kg, and $a = 1.13 \times 10^{-6}$ N/V^4·m.

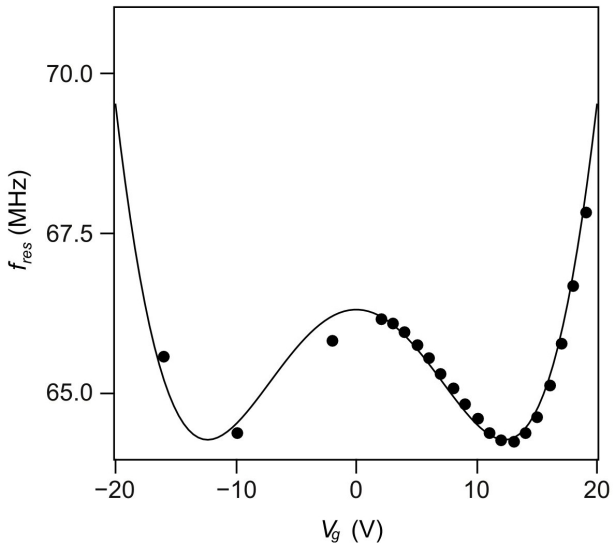

Figure 3.1: The tunability of resonance frequency by the gate voltage. FM mixing singal vs. frequency for device T1 at $T = 57$ K

Duffing term

The Duffing term is represented by a force term $F = -\alpha z_0^3$. Using eq. 3.3 and $\alpha = -\frac{1}{3!}\partial^3 F/\partial z_0^3 = \frac{1}{3!}\partial^4 \mathcal{U}/\partial z_0^4$, yields

$$\alpha = 8\pi(\lambda + 2\mu)/3r_0^2. \tag{3.10}$$

Effective mass

Here we compute the effective mass and resonance frequency of the vibrating membrane using a variant of Rayleigh's method. [33] For the vibrating graphene (or few layer) sheet, we have

$$z_0(t) = \bar{z}_0 + |\delta z| \sin \omega t,$$

where δz is the complex amplitude of the oscillation, and t is the time. The maximum kinetic energy when $z_0 = \bar{z}_0$ and the potential energy is minimal is then

$$KE = \int \frac{1}{2}\sigma\omega^2 |\delta z|^2 (1 - r^2/r_0^2)^2 r dr d\theta,$$

where σ is the resonator areal mass density. This gives

$$KE = \frac{1}{6}\pi\sigma|\delta z|^2 r_0^2 \omega^2.$$

Comparing this expression to the result for the ordinary harmonic oscillator, we get

$$m_{eff} = \frac{1}{3}\pi\sigma r_0^2. \tag{3.11}$$

For the resonance frequency when $V_g = 0$, $k_{eff} = 2\pi T_0$ and using the expression for m_{eff}, we get

$$\omega = \sqrt{\frac{2\pi T_0}{\frac{1}{3}\pi\sigma r_0^2}} = \frac{\sqrt{6}}{r_0}\sqrt{\frac{T_0}{\sigma}},$$

which is within a few percent of the exact result. [34]

3.4 Magnitude of FM signal in drum resonator

The FM technique described in Section. 2.8 will produce a signal with geometric factors arising from the drumhead geometry as compared to a parallel plate model. The signal is expected to be smaller both because the average deflection is less due to the pinned boundary conditions and because the average potential is less because of the voltage drop along the sample. Moreover, upon the transduction of the motion into an electrical signal, because of the shape of the deflection, the resistance change will also be less.

This yields a total attenuation factor of 16. This can be understood as one factor of 1/2 in the drive force from the shape of the distortion not being planar, and another factor of 1/2 since the average potential over the sheet is 1/2 of the applied potential. The signal transduction has a relative factor 1/4 because the resistance change is only concentrated near the center where the deflection is largest, and it is probed by a potential near the center which is $\sim$1/2 the potential applied. In the following we show the detailed computation of the expected total signal reduction from these sources.

From equation 3.1 the electrostatic energy term is given by

$$\mathcal{U}_{el} = -\int dxdy\, h(x,y)P(x,y),$$

where here the pressure P is no longer considered constant within the $x-y$ plane since the electrostatic potential V is now assumed to drop linearly between the electrodes. Fig. 3.2 shows a schematic diagram of the device geometry and potential drop. As before variational expression for the height is given by

$$h = z_0(1 - r^2/r_0^2). \tag{3.12}$$

The local pressure is given by

$$P = \frac{\epsilon_0}{2d^2}(V - V_g)^2,$$

with

$$V = V_{sd}\frac{L - x - r_0}{L},$$

where V_{sd} is the source-drain voltage, $x = 0, y = 0$ corresponds to the center of the circular drumhead and $L = 2r_0$. We then have

$$\mathcal{U}_{el} = -\int dxdy\, \frac{\epsilon_0}{2d^2}\left(-V_g + V_{sd}\frac{L - x - r_0}{L}\right)^2 z_0[1 - (x^2 + y^2)/r_0^2].$$

If $V_{sd} << V_g$ then

$$\mathcal{U}_{el} \cong \mathcal{U}_{DC} + \int dxdy\, \frac{\epsilon_0}{d^2}V_g V_{sd}\frac{L - x - r_0}{L}z_0[1 - (x^2 + y^2)/r_0^2] = \mathcal{U}_{DC} + \mathcal{U}_{AC},$$

where $\mathcal{U}_{DC}$ is the electrostatic energy arising from the DC gate voltage V_g. Performing the integral gives

$$\mathcal{U}_{AC} = \frac{\epsilon_0 \bar{A}}{4d^2}V_g V_{sd} z_0,$$

Giving a force magnitude

$$F_{AC} = \frac{\epsilon_0 \bar{A}}{4d^2}V_g V_{sd} \tag{3.13}$$

As discussed above, compared to the usual expression for a parallel plate capacitance and a spatially constant electrostatic potential,

$$\begin{aligned} F &= \frac{1}{2}C'V_g^2 \\ &= \frac{1}{2}C'(V_g + v_0)^2 \\ &\cong C'V_gV_{sd} \\ &= \frac{\epsilon_0 \bar{A}}{d^2}V_gV_{sd}, \end{aligned}$$

the effective force is 1/4 as much.

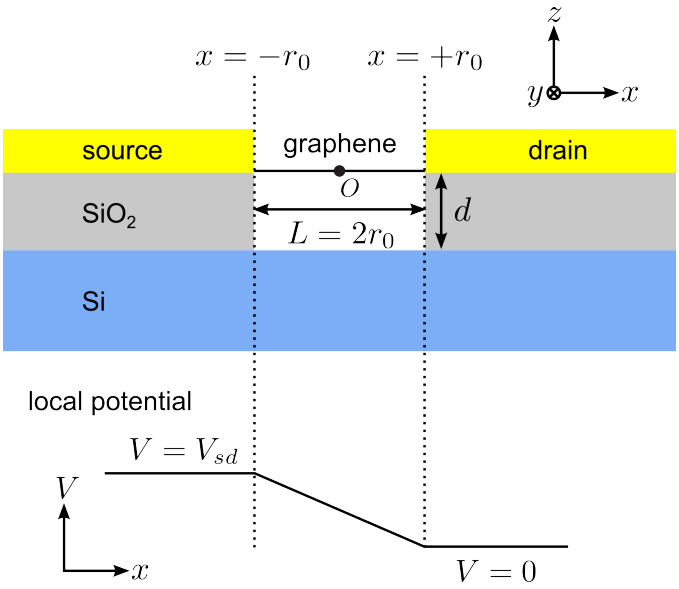

Figure 3.2: Schematic diagram of device geometry on an oxidized Si wafer, with a source, drain, and Si gate. The coordinate directions are indicated as well as the origin by O at the center of the resonator. The diameter of the drum membrane is L, and the radius is r_0. The spacing from the substrate is d. The voltage drop profile along the sample is also shown below the device diagram.

Current change caused by a membrane displacement

The total measured FM signal depends on the change in current caused by the membrane deflection discussed above. The current change caused by the membrane displacement in our experiment is expected to be smaller than the parallel plate result. This is because under the actual parabolic displacement the center has the most change

in conductance while the edge, which is pinned by the boundary, has zero. To determine the change in the current, we use the result that if an inhomogeneous sheet resistance exists then the 2D Laplace equation is modified to [35]

$$\nabla^2 V = \frac{\nabla R \cdot \nabla V}{R}, \tag{3.14}$$

where R is the local sheet resistance and V the electrostatic potential within the sheet. To solve this, we use perturbation theory by assuming the right hand side is small. The correction to lowest order will be

$$\nabla^2 V_{in} = \frac{\nabla R \cdot \nabla V_{hom}}{R}, \tag{3.15}$$

where V_{in} is the inhomogeneous potential produced by the forcing term on the right hand side of eq. 3.15, and V_{hom} is the unperturbed (homogeneous) potential. The total potential will be $V = V_{hom} + V_{in}$. Assuming small resistance changes, we replace the denominator of the right hand side of eq. 3.15 by the unperturbed value of R which we label R_0. To get an expression for ∇R, we start with an expression for R due to small changes in the charge density ρ.

$$\begin{aligned} R &= R_0 + \frac{\partial R}{\partial \rho}\delta\rho \\ \nabla R &= \frac{\partial R}{\partial \rho}\nabla(\delta\rho) \end{aligned} \tag{3.16}$$

using eq. 3.12 $\delta\rho$ can be expressed as

$$\delta\rho = \frac{\partial \rho}{\partial z_0} z_0[1 - (x^2 + y^2)/r_0^2] \tag{3.17}$$

Eqs. 3.16 and 3.17 taken together yield

$$\nabla R = \frac{\partial R}{\partial \rho}\frac{\partial \rho}{\partial z_0}\frac{z_0}{r_0^2}(-2r\hat{r}), \tag{3.18}$$

where $\hat{r}$ is the in-plane unit radial vector. The two derivatives in eq. 3.18 are considered constant. We define $T_R = \partial R/\partial\rho$. We also have

$$\frac{\partial\rho}{\partial z_0} = \frac{\partial}{\partial z_0}(-C_A V_g) = -V_g\frac{\partial C_A}{\partial z_0} = -V_g\frac{\partial}{\partial z_0}\frac{\epsilon_0}{z_0} = -V_g\frac{\epsilon_0}{z_0^2},$$

where C_A is the capacitance per unit area. This yields

$$\nabla R = T_R\frac{V_g\epsilon_0}{d^2}\frac{z_0}{r_0^2}(2r\hat{r}),$$

where d is the distance between the gate and the undisplaced membrane, assuming that positive z_0 indicates downwards deflection towards the gate. The unperturbed potential gradient is given by

$$\nabla V_{hom} = -\frac{V_{sd}}{L}\hat{x}$$

so the right hand side of eq. 3.15 is given by

$$\begin{aligned}\frac{\nabla R\cdot\nabla V_{hom}}{R_0} &= \frac{T_R V_g\epsilon_0}{R_0 d^2}\frac{z_0}{r_0^2}[2r\hat{r}\cdot(-\frac{V_{sd}}{L}\hat{x})]\\ &= \frac{-2T_R\epsilon_0 V_g V_{sd}}{R_0 d^2 L}\frac{z_0}{r_0^2}x\end{aligned}$$

Taking the solution to the 2D Poisson equation

$$\nabla^2 V = \delta(\vec{x}),$$

where $\delta(\vec{x})$ is the Dirac delta function as

$$V = \frac{1}{4\pi}\ln(x^2+y^2).$$

V_{in} is therefore given by

$$\begin{aligned}V_{in}(\vec{x}') &= -\int dxdy\,\frac{2T_R\epsilon_0 V_g V_{sd}}{R_0 d^2 L}\frac{z_0}{r_0^2}x\frac{1}{4\pi}\ln|\vec{x}'-\vec{x}|^2.\\ &= A_0\int dxdy\,x\ln|\vec{x}'-\vec{x}|^2,\end{aligned}$$

with

$$A_0 = -\frac{T_R \epsilon_0 V_g V_{sd}}{2\pi R_0 d^2 L} \frac{z_0}{r_0^2}.$$

The integral is taken over the resonator area, a circle of radius r_0. Converting this into a dimensionless integral over the unit circle by a change of coordinates and evaluating the integral numerically gives

$$\Delta V \cong \pi A_0 r_0^3.$$

Since the voltage and current are related by resistance R by $V = IR$,

$$\frac{\Delta V}{V} = \frac{\Delta R}{R} = -\frac{\Delta G}{G},$$

where $G = 1/R$ is the conductance. Then we have

$$\frac{\Delta V}{V} = -\frac{\Delta G}{G} = \frac{T_R V_g \epsilon_0 z_0}{4d^2 R_0}$$

This gives

$$\Delta G = -\frac{T_R V_g \epsilon_0 z_0}{4d^2 R_0} G = -\frac{T_R V_g \epsilon_0 z_0}{4d^2 R_0^2}.$$

Considering the vibration amplitude $|\delta z|$ this yields an expression for the ac current δI:

$$\delta I = -\frac{T_R V_g V_{sd} \epsilon_0 |\delta z|}{4d^2 R_0^2}.$$

We can rewrite this in terms of the transconductance $T = \partial G / \partial \rho$. We have

$$T = \frac{\partial G}{\partial \rho} = \frac{\partial (1/R)}{\partial \rho} = \frac{-1}{R^2} \frac{\partial R}{\partial \rho}.$$

Thus,

$$\delta I = \frac{T V_g V_{sd} \epsilon_0 |\delta z|}{4d^2}, \tag{3.19}$$

We can compare this to the parallel plate result

$$\begin{aligned} \delta I &= V_{sd} \Delta G \\ &= V_{sd} T V_g C' |\delta z| \\ &= \frac{V_{sd} T V_g \epsilon_0 |\delta z|}{d^2} \end{aligned}$$

Thus we have another 1/4 factor signal reduction because of the geometry. The total signal will be 1/16 of that expected from a parallel plate model for the resonator. With this factor of 1/4, the FM signal is expected to be, using the parallel plate result from ref. [8]

$$\delta I = \frac{1}{8}\frac{\partial G}{\partial V_g} V_{sd} V_g \frac{C'}{C} f_\Delta \frac{\partial}{\partial f} \Re[\delta z],$$

We have also the relation for a harmonic oscillator on resonance

$$\frac{d\Re[\delta z]}{df} = \frac{-2|\delta z|}{\delta f},$$

where δf is the frequency width of the resonance. Therefore the amplitude in terms of known experimental parameters is given by:

$$|\delta z| = \frac{4 d \delta I \delta f}{(\partial G/\partial V_g) V_{sd} V_g f_\Delta} \tag{3.20}$$

Chapter 4

Nonlinear Dynamics

4.1 Introduction

In chapter 1, we reviewed the dynamic behavior of harmonic oscillator in the linear regime, where the equation of motion contains the linear restoring force and linear damping force:

$$m\frac{d^2z}{dt^2} + m\omega_0^2 z + \Gamma\frac{dz}{dt} = G_0\cos(\omega t). \tag{4.1}$$

This equation describes the behavior when displacement z is small. When we turn up the driving, the higher order nonlinear terms in z start to play an important role. In this chapter, we will discuss the Duffing nonlinearity and nonlinear damping in harmonic oscillators. Our experimental data is in consistent with previous related works. [10, 36] We have also observed an anomalous large line width at large drives. We attribute this to the periodic thermal expansion of the graphene from the ac source-drain voltage provides a parametric amplification to the response. Part of the contents in this chapter can be found in my previous published work [1].

4.2 Duffing Nonlinearity and Nonlinear Damping

There are two most often seen nonlinearities in NEMS resonators, and both of them have been reported in graphene and nanotube NEMS devices [10]. One is the restoring force term that is cubic in displacement $-\alpha z^3$, where α is the coefficient. [10, 37] The equation of motion including this term is so-called Duffing equation. The origin of the duffing nonlinearity has two major sources: the external potential has nonlinearity in z [36, 32] and the geometry causes the elastic energy to be nonlinear in z (for example, the membrane is clamped at the boundary and the deflection stretches the membrane) [36]. The other one is the nonlinear damping force term $-\eta z^2 \frac{dz}{dt}$, where η is the coefficient. [36, 10] The nonlinear damping depends on the displacement. The origin however is still unknown. The equation of motion contains these two terms is as follows:

$$m\frac{d^2z}{dt^2} + \Gamma\frac{dz}{dt} + m\omega_0^2 z + \alpha z^3 + \eta z^2\frac{dz}{dt} = G_0\cos(\omega t). \tag{4.2}$$

The duffing term tends to change the effective spring constant and hence the resonance frequency. The frequency of the maximum response shifts as the driving amplitude increases, as shown in fig. 4.1. The relation of the resonance frequency of the maximum response ω_{max} and the amplitude of displacement z_0 is as follows [36]:

$$\omega_{max} = \omega_0 + \frac{3}{8}\frac{\alpha}{m\omega_0}z_0^2 \tag{4.3}$$

For most cases in our experiments, we observe an increase of resonance frequency as z_0 increases, which means we see a positive α. But we sometimes also observe a decrease of the resonance frequency as z_0 increases, with a negative α. The reason for this is still unknown, but it could be related to that the development of the force term quadratic in z renormalizes the measured α. [36] Fig. 4.1 is from ref. [36], and it shows the solution for the magnitude and phase of the response of a Duffing oscillator at various driving

amplitudes. The magnitude of the response grows and the resonance frequency shifts as the driving force increases. Here we also plot in fig. 4.2 a series of line traces of the mixing current vs. frequency at difference driving amplitude for a few-layer graphene drum resonator using FM mixing technique. The line shape becomes more and more asymmetric around the resonance frequency and the resonance frequency increases as the ac driving voltage V_{sd} goes up.

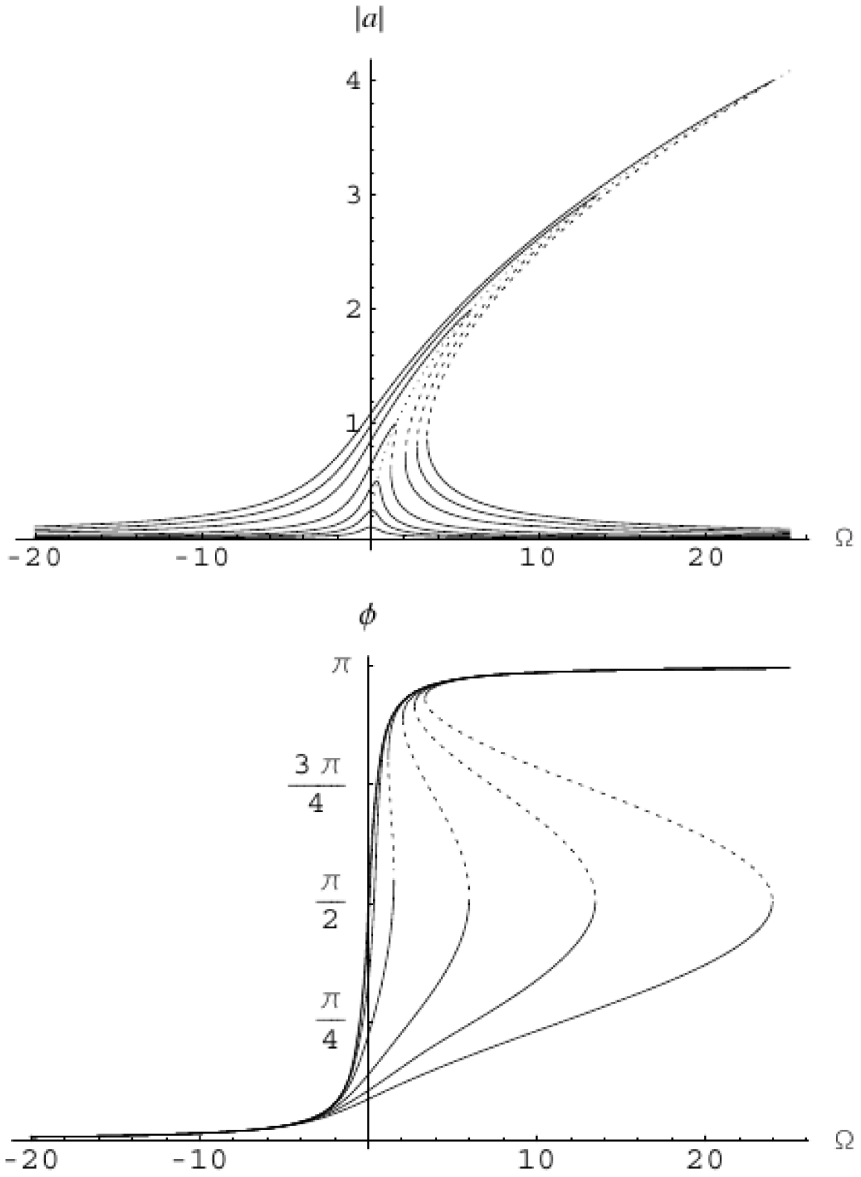

Figure 4.1: Magnitude $|a|$ (upper) and phase ϕ (lower) of the response of a Duffing resonator as a function of frequency Ω with nonlinear damping coefficient $\eta = 0$. The different line traces are at various driving amplitude. This figure is adapted from ref. [36].

At sufficiently large driving amplitude, we start to see the saddle-node bifurcation in the solution of the response. We the frequency sweeps from left to right in fig. 4.1, we see changes of number of solutions of magnitude for each frequency. At first, we only see one solution. Then at a critical point, there are two solutions. After that we see three solutions. Finally, the number of solutions becomes back to one. The stable solution is indicated as solid lines and the unstable solution is indicated as dashed lines in fig. 4.1. This could result in hysteresis if we sweep the frequency upwards and downs. For the upward frequency sweeping, the magnitude of response $|a|$ follows the upper branch until it reaches the maximum point and suddenly falls onto the lower branch; for the downward frequency sweeping, $|a|$ follows the lower branch until it reaches the critical point and switches to the upper branch. Fig. 4.3 shows upward and downward frequency sweeps of the mechanical resonance signal of a device measured by FM mixing technique. Since the mixing current $I_{mix} \propto \partial \mathrm{Re}(z)/\partial\omega$, it is complicated to simulate the line shape of the mixing current of a duffing oscillator using FM mixing technique. However the upward and downward frequency sweep does show a hysteresis and it is similar to the data shown in ref. [10].

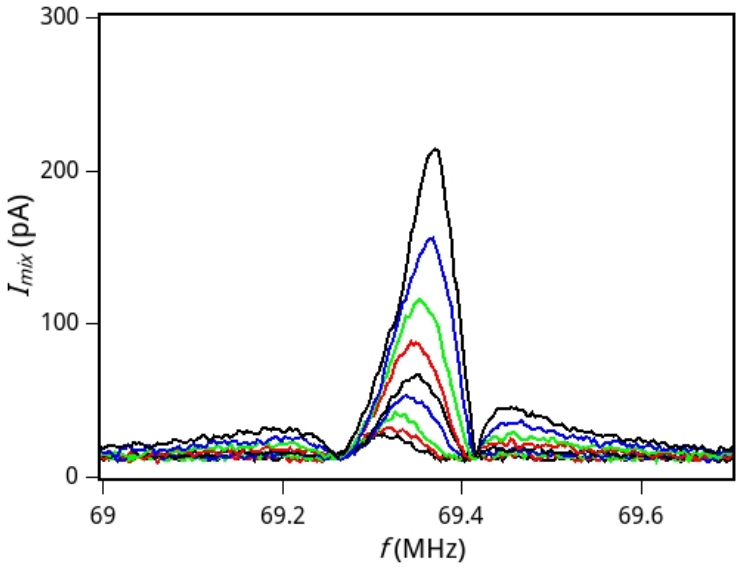

Figure 4.2: FM mixing signal vs. frequency at different source-drain voltages V_{sd} for a few-layer graphene drum resonator (device T1) at T = 57V and V_g = 20V. V_{sd} ranges from 2mV to 7mV. The asymmetric line shapes and shift of resonance frequency shows the duffing nonlinearity.

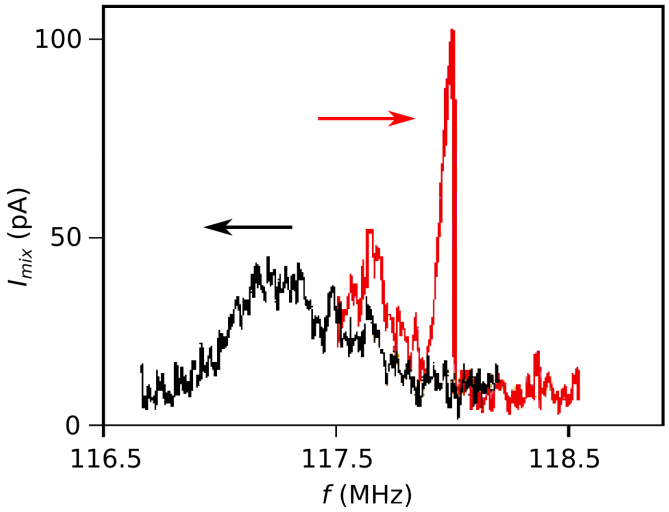

Figure 4.3: Hysteresis of the FM mixing signal vs. frequency of a few-layer graphene drum resonator (device T2). Diameter = 2 μm, V_{sd} = 60mV, f_Δ = 50 kHz, V_g =-10V, T = 4.3 K. Red curve: upward frequency sweep. Black curve: downward frequency sweep.

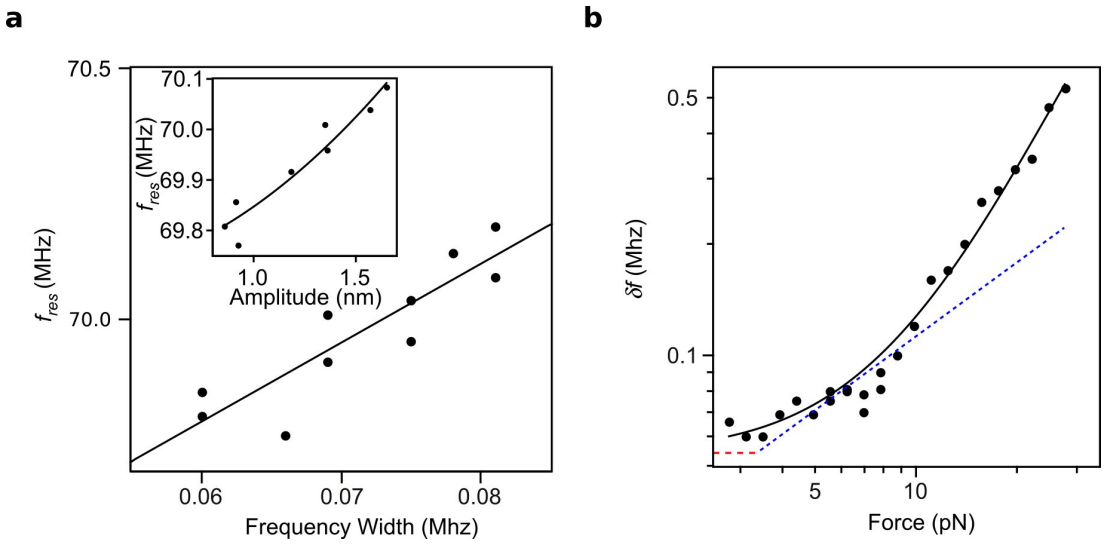

Figure 4.4: Nonlinear resonator dynamics. (a) Main panel: resonance frequency vs. frequency width at $T = 16$ K and $V_g = 18$ V plotted as black circles. Solid curve is a straight line fit to the data. Inset: resonance frequency vs. amplitude at $T = 16$ K and $V_g = 18$ V plotted as black circles. The amplitude is obtained from the FM line shape when it is still approximately Lorentzian (eq. 3.20). Solid curve is a fit to the theoretical expectation (eq. 4.22). (b) Frequency width δf vs. force on the oscillator. Dashed blue curve is the expected trend based on a cubic nonlinear damping term; dashed red curve is the width in the linear damping regime as determined by extrapolating the data in the main panel of part (a) to the zero amplitude frequency determined by the fit to part (a) inset; the solid black curve takes into account both nonlinear damping and a simultaneous parametric drive due to Joule heating by the source drain voltage. Data taken at $T = 16$ K and $V_g = 18$ V.

Plotting Δf against f_{res}, it reveals a straight line trend, as shown in Fig. 4.4a. It can be shown that (eq. 4.23) the slope of this line is related to α/η by $\alpha/\eta \approx 4\pi \frac{d\Delta f}{d\delta f} f_0$. Fitting the data gives $\alpha/\eta = 3.4 \times 10^9$ s^{-1}. We obtain α by plotting Δf versus amplitude (Fig. 4.4a inset), [36, 10, 37] and fitting to the theoretical expectation for α, which gives a frequency shift that is quadratic in the amplitude (eq. 4.22). From Fig. 4.4a inset data with the trilayer m_{eff} we obtain $\alpha = 2.4 \times 10^{15}$ N/m^3. This yields $\eta \sim 1.8 \times 10^5$ Ns/m^3.

To understand the origin of the Duffing nonlinearity, we use a variational method along with continuum elastic theory to determine $\alpha = 8\pi(\lambda+2\mu)/3r_0^2$ (eq. 3.10). Putting in $\lambda = 3 \times 48$ N/m, $\mu = 3 \times 144$ N/m, [30] for a trilayer and r_0=10^{-6} m we find $\alpha = 8.4 \times 10^{15}$, in good agreement to the measured value. This suggests that the origin of the Duffing term is geometric in nature. A smaller value of α is found at a higher temperature $T = 57$K (Fig. 4.5), which may indicate the development of a quadratic force that renormalizes α. [36]

To account for the nonlinear damping, previous work has proposed a viscoelastic model for damping in NEMS. [38] However, the predicted nonlinear damping is much smaller than the typically observed magnitude. [10] Another model for graphene resonators that considers in-plane and bending mode coupling and energy loss by in-plane phonon radiation into the substrate performs numerical calculations for a similar geometry to the one presented here, consisting of a doubly clamped graphene sheet that is 1 μm $\times$ 1 μm. [39] A scaling analysis shows that $\eta \sim T_1\sigma^3\omega^3$, where $T_1 = \lambda + 2\mu$. A similar value to the one measured for our trilayer sample is obtained with a mass ~ 3 trilayer masses, suggesting that this mechanism plays an important role in determining the nonlinear damping in graphene resonators.

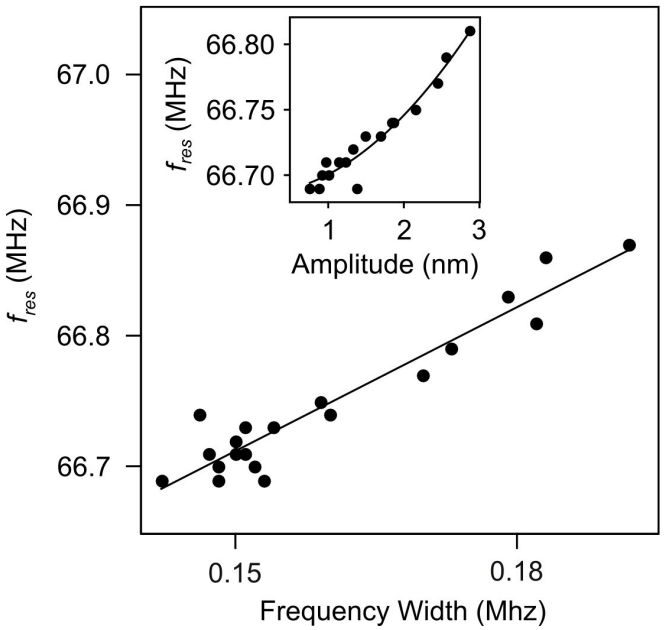

Figure 4.5: Nonlinear oscillator dynamics of the lowest-frequency mode. Main panel: resonance frequency vs. frequency width at $T = 57$ K and $V_g = 18$ V plotted as black circles. Solid curve is a straight line fit to the data. Inset: resonance frequency vs. amplitude at $T = 57$ K and $V_g = 18$ V plotted as black circles. The amplitude is obtained from the FM lineshape when it is still approximately Lorentzian (eq. 3.20). Solid curve is a fit to the theoretical expectation (eq. 4.22). The data analysis yields $\eta = 8 \times 10^4$ Ns/m^3 and $\alpha = 2.4 \times 10^{14}$ N/m^3. T he lower value for α than at $T = 16$ K may indicate the presence of quadratic displacement terms as in eq. 4.7.

4.3 Parametric Driving by Thermal Expansion

To investigate the resonator response at larger drives, in Fig. 4.4b we plot δf versus the effective ac force on the sheet at the drive frequency f, given by $F_{ac} = \frac{\epsilon \pi r_0^2}{4d^2} V_g V_{sd}$ (eq. 3.13), measured at $T = 16$ K. At small drive force, δf is approximately $\propto V_{sd}^{2/3}$ (shown by the blue dashed line) following the expected trend due to nonlinear damping. [10] At larger biases, however, the measured frequency width becomes much larger, tending towards a $\propto V_{sd}^2$ power law.

One possibility is that this originates from higher order terms such as a 5th order damping force term. However, detailed calculation shows such terms lead to a smaller predicted response, rather than larger. We therefore consider the possibility that an unintentional parametric drive is being applied to the resonator. Such a parametric drive results when the resonance frequency is modulated by δf_0 by changing one of the parameters of the oscillator, such as its stiffness (see e.g. ref. [36] review and ref. [26] for recent work on carbon nanotubes). The parametric drive is quantified by $H = 2\delta f_0 / f_0$ which is the dimensionless stiffness modulation,[36] and can produce amplification or even self-oscillations.[36] One possible source of parametric driving is electrostatic forces, however over the voltage range shown we estimate these forces are likely too small to produce the observed behavior. We then consider a parametric drive caused by the periodic thermal expansion of the graphene sheet due to Joule heating by V_{sd}. Then in terms of the ac force drive F_{ac} given above, the power dissipated P_0 and the temperature shift in the sheet ΔT, $H \propto \Delta T \propto P_0 \propto V_{sd}^2 = bF_{ac}^2$ with b given by

$$b \approx \left(\frac{4d^2}{\epsilon_0 A V_g}\right)^2 \frac{|a_T|(\lambda+\mu)}{2\pi R \kappa_{2D} T_0}, \tag{4.4}$$

where a_T is the negative thermal expansion coefficient and the 2D thermal conductivity κ_{2D}=$\kappa_B \tau$ with κ_B the bulk thermal conductivity and τ the layer thickness, and R

the electrical resistance. (eq. 4.21.) The nonlinear equations of motion are solved approximately using the method of harmonic balance. [40] For large drive δf is given by (eq. 4.20)

$$\delta f = \frac{3}{8}\left(1 + \frac{\sqrt{3}\alpha}{2\pi\eta f_0}\right) bF_{AC}^2 f_0 + const. \tag{4.5}$$

scaling as V_{sd}^2 for large drive, as observed. Further approximations yield a function describing the behavior from the linear to the nonlinear asymptotic regime (Section 4.4). The solid curve in Fig. 4.4b shows a fit to this function with b and m_{eff} as fit parameters, yielding $b = 7.8 \times 10^{17}$ N^{-2}, and $m_{eff} = 8.3 \times 10^{-18}$ kg. From this, using the measured R of 1.7 $k\Omega$ we determine at $T = 16$ K, $|a_T|/\kappa_{2D} \sim 2$ W^{-1}. The expected room temperature value with $a_T = -10^{-5}$K^{-1}, [41] and κ=2000 W/m·K for a ∼1 nm thick trilayer [42] gives ~ 5 W^{-1}. From elementary kinetic theory this ratio is unlikely to vary strongly with temperature since the phonon mean free path is expected to be impurity or surface limited below 300 K. [42] The result is thus in reasonable agreement with expectations, providing strong evidence that thermal expansion driven parametric driving is occurring. This result therefore constitutes the first low-temperature measurement of this ratio $|a_T|/\kappa_{2D}$.

4.4 Solution to the Nonlinear Equation of Motion

The equation of motion for a nonlinear oscillator can be expressed as

$$m\frac{d^2\bar{z}}{d\bar{t}^2} + \Gamma\frac{d\bar{z}}{d\bar{t}} + m\omega_0^2\bar{z} + \bar{\chi}\bar{z}^2 + \bar{\mu_0}\bar{z}\frac{d\bar{z}}{d\bar{t}} + \bar{\alpha}\bar{z}^3 + \bar{\eta}\bar{z}^2\frac{d\bar{z}}{d\bar{t}} = \bar{G}_0\cos(\bar{\omega}\bar{t} + \phi). \tag{4.6}$$

Here we add a bar to notate the real length variables. To switch to units such that $\alpha = m = \omega_0 = 1$ the dimensionless length variable is taken to be $z = \bar{z}\sqrt{\bar{\alpha}/m\omega_0^2}$, and the parameters of the oscillator equation of motion can be expressed in dimensionless

form as follows [36]

$$\epsilon = Q^{-1} = \frac{\Gamma}{m\omega_0}; \eta = \frac{\bar{\eta}\omega_0}{\bar{\alpha}}; G_0 = \frac{\bar{G}_0}{\omega_0^3}\sqrt{\frac{\bar{\alpha}}{m^3}}; \chi = \frac{\bar{\chi}}{\omega_0\sqrt{m\bar{\alpha}}}; \mu_0 = \frac{\bar{\mu_0}}{\sqrt{m\bar{\alpha}}}; \omega = \frac{\bar{\omega}}{\omega_0}.$$

Here we assume that Q is determined from frictional forces alone, and ignore frequency broadening which is an interesting topic we will discuss in the next chapter. We take this as a good approximation when the resonator is driven into the regime where nonlinear damping is important. The equation of motion can then be scaled to yield

$$\ddot{z} + \epsilon\dot{z} + z + \chi z^2 + \mu_0 z\dot{z} + z^3 + \eta z^2\dot{z} + [h_0\epsilon\cos(2\omega t + 2\phi)]z = \epsilon^{3/2} g_0\cos(\omega t + \phi) \quad (4.7)$$

The parameter ϵ which is the inverse quality factor is considered a small parameter that enables approximate solutions that are expanded in ϵ. Motivated by our experimental results, in eq. 4.7 we have also included a parametric drive parametrized by h_0 that modulates the resonance frequency by $\delta\omega_0$ at a frequency 2ω as well as force drive parametrized by g_0 such that $G_0 = \epsilon^{3/2} g_0$. The quantity $h_0\epsilon = 2\delta\omega_0/\omega_0$ gives the fractional amplitude of the frequency modulation relative to the undriven characteristic frequency ω_0. To solve this equation, following the original method used by Duffing, (See for example ref. [40]) we first assume to zero order the time dependence for the oscillator displacement with amplitude parameter Γ_0 and frequency ω given by

$$z_0 = \Gamma_0\epsilon^{1/2}\sin\omega t. \quad (4.8)$$

Here we reference the phases of the force and parametric drives to the response, which is taken to be a sine function. For a linear oscillator, the $\phi = 0$ on resonance (the drive being proportional to a cosine when the response is a sine). Note that in this definition of the phase ϕ occurs in the drive term rather than the response. This differs from the conventional treatment of the harmonic oscillator but simplifies the calculations below.

The equation of motion 4.7 is rearranged to yield an expression for the acceleration:

$$\ddot{z} = -\epsilon\dot{z} - z - \chi z^2 - \mu_0 z\dot{z} - z^3 - \eta z^2\dot{z} - [h_0\epsilon\cos(2\omega t + 2\phi)]z + \epsilon^{3/2} g_0\cos(\omega t + \phi) \quad (4.9)$$

the expression for z_0 is substituted into the right hand side of the above equation, and integrated twice to yield a solution for z_1. which produces the following result:

$$\begin{aligned} z_1 \;=\; & -\frac{1}{4}\,\Gamma_0^2\chi\epsilon t^2 + \frac{\Gamma_0^3\epsilon^{\left(\frac{3}{2}\right)}\eta\cos(\omega t)}{4\,\omega} \\ & -\frac{\Gamma_0^3\epsilon^{\left(\frac{3}{2}\right)}\eta\cos(3\,\omega t)}{36\,\omega} + \frac{\Gamma_0^2\epsilon\mu_0\sin(2\,\omega t)}{8\,\omega} \\ & +\frac{3\,\Gamma_0^3\epsilon^{\left(\frac{3}{2}\right)}\sin(\omega t)}{4\,\omega^2} - \frac{\Gamma_0^3\epsilon^{\left(\frac{3}{2}\right)}\sin(3\,\omega t)}{36\,\omega^2} \\ & -\frac{\Gamma_0^2\chi\epsilon\cos(2\,\omega t)}{8\,\omega^2} - \frac{\Gamma_0\epsilon^{\left(\frac{3}{2}\right)}h_0\sin(\omega t + 2\,\phi)}{2\,\omega^2} + \frac{\Gamma_0\epsilon^{\left(\frac{3}{2}\right)}h_0\sin(3\,\omega t + 2\,\phi)}{18\,\omega^2} \\ & +\frac{\Gamma_0\epsilon^{\left(\frac{3}{2}\right)}\cos(\omega t)}{\omega} - \frac{\epsilon^{\left(\frac{3}{2}\right)}g_0\cos(\omega t + \phi)}{\omega^2} + \frac{\Gamma_0\sqrt{\epsilon}\sin(\omega t)}{\omega^2} \end{aligned} \quad (4.10)$$

Equating the coefficients of $\sin(\omega t)$ and $\cos(\omega t)$ between z_0 and z_1 produces a set of equations that can then be solved for Γ_0 and ϕ. The resulting solution is approximate, and when substituted into the original equation of motion produces non-zero error terms. However, these error terms will be at other harmonics besides those at frequency ω and of order ϵ or smaller. Thus the obtained values for Γ_0 and ϕ will be correct to lowest order in ϵ. In the present case, there are two additional issues to the expression given for z_0 in eq. 4.8. One is that it generates a term quadratic in t of order ϵ in z_1. This can be eliminated by adding an ϵ-order constant to z_0 and setting it so the t^2 term vanishes. The other issue is that z_1 contains terms of order ϵ and frequency 2ω. If one were to proceed to higher order, the quadratic terms in the equation of motion would generate additional terms of order $\epsilon^{3/2}$ which are at the same order as the terms with frequency ω. To avoid this, z_0 must be corrected to add these terms so that z_1 is

correct to order $\epsilon^{3/2}$ with only one iteration. The necessary expression is then:

$$z_0 = \Gamma_0\sqrt{\epsilon}\sin(\omega t) + \Lambda_1\epsilon\sin(2\,\omega t) + \Lambda_2\epsilon\cos(2\,\omega t) + \Lambda_3\epsilon,$$

with Λ_1, Λ_2 and Λ_3 constants to be determined. After substituting z_0 into the right hand side of eq. 4.9 and matching the appropriate coefficients we get the following coupled cubic equations for Γ_0 and ϕ with effective cubic parameters η and α:

$$\begin{aligned}\left(2\Omega + \frac{1}{2}h_0\cos 2\phi - \frac{3}{4}\alpha\Gamma_0^2\right)\Gamma_0 - g_0\sin\phi &= 0\\ \frac{1}{4}\Gamma_0^3\eta - \frac{1}{2}\Gamma_0 h_0\sin 2\phi + \Gamma_0 - g_0\cos\phi &= 0\end{aligned} \tag{4.11}$$

The frequency width in the FM technique is determined by the frequency spacing between the stationary points of the real part of the response. [8] The real part is given by the in-phase response to the drive, which we find based on eq. 4.7 to yield $\Re[z] = -\Gamma_0\sin\phi$. Thus we want to find the stationary points of $-\Gamma_0\sin\phi$ subject to the constraints given by the coupled cubic equations in eq. 4.11. Thus we use the method of Lagrange multipliers, which requires finding the stationary points of the function

$$\begin{aligned}f &= -\Gamma_0\sin\phi + \lambda_1\left[\left(2\Omega + \frac{1}{2}h_0\cos 2\phi - \frac{3}{4}\alpha\Gamma_0^2\right)\Gamma_0 - g_0\sin\phi\right]\\ &\quad +\lambda_2\left(\frac{1}{4}\Gamma_0^3\eta - \frac{1}{2}\Gamma_0 h_0\sin 2\phi + \Gamma_0 - g_0\cos\phi\right),\end{aligned}$$

introducing auxiliary Lagrange multiplier variables λ_1, and λ_2 that multiply the two constraint equations. Optimizing this gives 3 equations, which together with the original

constraints eq. 4.11 yield 5 equations and 5 unknowns for $\Omega, \phi, \Gamma_0, \lambda_1$, and λ_2.

$$\begin{aligned}
\frac{1}{4}\left(3\Gamma_0^2\eta - 2h_0\sin 2\phi + 4\right)\lambda_2 - \frac{1}{4}\left[9\Gamma_0^2\alpha - 2h_0\cos 2\phi - 8\Omega\right]\lambda_1 - \sin\phi &= 0 \\
-(\Gamma_0 h_0\cos 2\phi - g_0\sin\phi)\lambda_2 - (\Gamma_0 h_0\sin 2\phi + g_0\cos\phi)\lambda_1 - \Gamma_0\cos\phi &= 0 \\
2\Gamma_0\lambda_1 &= 0 \\
\left(2\Omega + \frac{1}{2}h_0\cos 2\phi - \frac{3}{4}\alpha\Gamma_0^2\right)\Gamma_0 - g_0\sin\phi &= 0 \\
\frac{1}{4}\Gamma_0^3\eta - \frac{1}{2}\Gamma_0 h_0\sin 2\phi + \Gamma_0 - g_0\cos\phi &= 0
\end{aligned} \tag{4.12}$$

From the third equation down in the above equation, we see that unless Γ_0 is zero then $\lambda_1 = 0$. The system of equations can then be simplified to

$$\frac{1}{4}\left(3\Gamma_0^2\eta - 2h_0\sin 2\phi + 4\right)\lambda_2 - \sin\phi = 0 \tag{4.13}$$

$$-(\Gamma_0 h_0\cos 2\phi - g_0\sin\phi)\lambda_2 - \Gamma_0\cos\phi = 0 \tag{4.14}$$

$$\left(2\Omega + \frac{1}{2}h_0\cos 2\phi - \frac{3}{4}\alpha\Gamma_0^2\right)\Gamma_0 - g_0\sin\phi = 0 \tag{4.15}$$

$$\frac{1}{4}\Gamma_0^3\eta - \frac{1}{2}\Gamma_0 h_0\sin 2\phi + \Gamma_0 - g_0\cos\phi = 0 \tag{4.16}$$

We first seek an asymptotic solution to the system of equations 4.13-4.16 valid for large g_0 and h_0. Dividing eq. 4.16 through by $\Gamma_0 h_0$ gives

$$\frac{\Gamma_0^2\eta}{4h_0} - \frac{1}{2}\sin 2\phi + \frac{1}{h_0} - \frac{g_0\cos\phi}{\Gamma_0 h_0} = 0 \tag{4.17}$$

If we assume the parametric drive comes from heating as discussed in Section 4.3, then we expect the parametric drive h_0 will be related to the force drive by $h_0 = bg_0^2$, where b is a constant. Therefore in the limit of large g_0, keeping the dominant term in Γ_0 eq. 4.17 reduces to

$$\frac{\Gamma_0^2\eta}{h_0} = 2\sin 2\phi$$

Eq. 4.14 can then be solved for λ_2:

$$\lambda_2 = -\frac{\Gamma_0 \cos(\phi)}{\Gamma_0 h_0 \cos(2\,\phi) - g_0 \sin(\phi)}$$

and substituted in to eq. 4.13, which gives

$$\frac{1}{4}\frac{(2\Gamma_0^2\eta + 4)\Gamma_0 \cos\phi}{\Gamma_0 h_0 \cos 2\phi - g_0 \sin\phi} + \sin\phi = 0$$

Neglecting the 4 compared to $2\Gamma_0^2\eta$, as appropriate for the large amplitude limit, and dividing the top and bottom of the fraction by h_0 gives:

$$\frac{\frac{1}{4}\frac{(2\Gamma_0^2\eta)}{h_0}\Gamma_0 \cos\phi}{\Gamma_0 \cos 2\phi - (g_0/h_0)\sin\phi} + \sin\phi = 0 \tag{4.18}$$

In the limit of large h_0 this reduces to

$$\frac{1}{4}(4\sin 2\phi)\frac{\cos\phi}{\cos 2\phi} + \sin\phi = 0$$

which gives

$$\begin{aligned} \sin 2\phi \cos\phi + \cos 2\phi \sin\phi &= 0 \\ \sin 3\phi &= 0 \\ \phi &= 0, \pm\pi/3, \pm 2\pi/3... \end{aligned}$$

The values $\phi = 0, \pi$ are not considered since in conjunction with eq. 4.18 these values imply that $\Gamma_0 = 0$. Since the *low-amplitude* resonance has $\phi = 0$, we expect the flanking minima will have $\phi = \pm\pi/3$. These values for the phase can then be substituted into eq. 4.16. For $\phi = \pi/3$, we get the cubic equation

$$\Gamma_0^3 + \left(\frac{4 - \sqrt{3}h_0}{\eta}\right)\Gamma_0 - \frac{2\,g_0}{\eta} = 0$$

For large h_0, it can be shown that there are three real roots, and the one that matches continuously to the single real root for small h_0 is given approximately by

$$\Gamma_0 \approx \sqrt{\frac{\sqrt{3}h_0 - 4}{\eta}}$$

This value for Γ_0 can then be substituted back into eq. 4.15 along with ϕ to determine Ω corresponding to a stationary value of the phase. Solving eq. 4.15 for Ω yields

$$\Omega = \frac{3}{8}\,\Gamma_0^2\alpha - \frac{1}{4}\,h_0\cos(2\,\phi) + \frac{g_0\sin(\phi)}{2\,\Gamma_0}$$

This gives for large h_0 the frequency of the upper frequency minimum in the FM signal, Ω_+:

$$\begin{aligned}\Omega_+ &= \frac{1}{8}h_0 + \frac{3}{8}\frac{\alpha}{\eta}(\sqrt{3}h_0 - 4) + \frac{3^{1/4}}{4}\sqrt{\frac{\eta}{b}} \\ &= \left(\frac{1}{8} + \frac{3\sqrt{3}}{8}\frac{\alpha}{\eta}\right) bg_0^2 + const.\end{aligned}$$

for the case $\phi = -\pi/3$ the equation for Γ_0 is given by

$$\Gamma_0^3 + \left(\frac{4+\sqrt{3}h_0}{\eta}\right)\Gamma_0 - \frac{2\,g_0}{\eta} = 0$$

It can be shown that this equation has one real root,

$$\Gamma_0 = \frac{2\sqrt{3}}{3}\frac{g_0}{h_0}$$

When substituted into eq. 4.15 along with the value for ϕ, we find for large h_0 the frequency of the lower frequency minimum Ω_-:

$$\Omega_- = -\frac{1}{4}h_0 = -\frac{1}{4}bg_0^2$$

This gives in the large drive asymptotic limit

$$\Delta\Omega = \Omega_+ - \Omega_- = \frac{3}{8}\left(1 + \frac{\sqrt{3}\alpha}{\eta}\right) bg_0^2 + \frac{3^{1/4}}{4}\sqrt{\frac{\eta}{b}} - \frac{3}{2}\frac{\alpha}{\eta}. \tag{4.19}$$

This is quadratic in the drive as observed experimentally. Going back to physical units gives

$$\delta f = \frac{3}{8}\left(1 + \frac{\sqrt{3}\alpha}{2\pi\eta f_0}\right) bF_{AC}^2 f_0 + const., \tag{4.20}$$

where F_{AC} is the ac electrostatic force on resonator.

To obtain an approximate solution valid for any drive strength, numerical solutions of the systems of equations 4.13-4.16 are used to show that the two oscillator phases ϕ_+ and ϕ_- corresponding to the two minima in the FM signal can be serviceably approximated by the mathematical functions

$$\begin{aligned} \phi_+ &= \pi/4 + \pi/12 \tanh(bg_0^2) \\ \phi_- &= -\pi/4 - \pi/12 \tanh(bg_0^2) \end{aligned}$$

These phases can be substituted into eq. 4.16 and the resulting cubic equation for Γ_0 solved for each phase. When these values for Γ_0 are substituted back into eq. 4.15 the resulting equation can be solved for Ω. The difference between the two Ω solutions corresponding to ϕ_+ and ϕ_- gives the frequency width function. The solution can be expressed in physical units and then fit to the data.

4.5 Estimation for b

Using the Fourier heat law, the temperature rise ΔT at the center of the graphene membrane assuming thermal equilibration to the ambient substrate temperature at the boundary is

$$\Delta T = \frac{P_0 r^2}{4\kappa_{2D}\bar{A}},$$

where $\bar{A}$ is the membrane area, P_0 is the power dissipated, r is the radius, and κ_{2D} is the two-dimensional thermal sheet conductivity. Taking $P_0 = V_{sd}^2/R$, where R is the device resistance then

$$\Delta T = \frac{V_{sd}^2}{4\pi R \kappa_{2D}}.$$

If a_T is the (negative valued) thermal expansion coefficient, then the change in strain δc is given by

$$\delta c \approx \frac{V_{sd}^2 |a_T|}{4\pi R \kappa_{2D}},$$

which changes the membrane tension T_0 by an amount δT_0 given by

$$\delta T_0 = \frac{V_{sd}^2 |a_T| (\lambda + \mu)}{2\pi R \kappa_{2D}}$$

The parametric drive H is given by $2\delta f_{res}/f_{res}$, where δf_{res} is the modulation of the resonance frequency f_{res}. In terms of the tension, we have $\delta f_{res}/f_{res} = \frac{1}{2}\delta T_0/T_0$. Thus,

$$H = \frac{V_{sd}^2 |a_T| (\lambda + \mu)}{2\pi R \kappa_{2D} T_0}$$

Using the result for the force drive from eq. 3.13, we find

$$H = \left(\frac{4d^2}{\epsilon_0 \bar{A} V_g} \right)^2 G_0^2 \frac{|a_T| (\lambda + \mu)}{2\pi R \kappa_{2D} T_0},$$

and therefore the constant b is given by

$$b = \left(\frac{4d^2}{\epsilon_0 \bar{A} V_g} \right)^2 \frac{|a_T| (\lambda + \mu)}{2\pi R \kappa_{2D} T_0} \tag{4.21}$$

4.6 Expression for α/η

The ratio α/η can be determined from the data at small drive, from the equations 4.13-4.16 setting $h = 0$, and considering g to be small. The phase at the minima of the FM signal is taken to be $\approx \pm\pi/4$. Using these approximations, the system of equations can be solved to yield in dimensionless units

$$\Delta\Omega = 1 + \frac{3}{4}\eta\Gamma_0^2$$

Using also the expression for the frequency shift with drive in terms of α [10, 37]

$$f_{res} = f_0 + \frac{3\alpha|\delta z|^2}{32\pi^2 f_0 m} \tag{4.22}$$

where f_0 is the linear response resonance frequency, and setting $\Delta f = f_{res} - f_0$ and $\delta f = \epsilon f_0 \Delta\Omega$ the linewidth we find

$$\frac{\alpha}{\eta} = 4\pi \frac{d\Delta f}{d\delta f} f_0, \tag{4.23}$$

which gives a way of measuring the ratio α/η.

Chapter 5

Stochastic-Frequency Oscillators

5.1 Introduction

In this chapter, we will discuss our experimental results on the quality factor of graphene drum resonators. We measure Q of the lowest frequency mode and observe that Q inversely scales with the temperature. We attribute this to the frequency broadening of the low frequency mode from nonlinear coupling to thermally excited high frequency modes. The contents in this chapter can be found in my previous published work [1].

5.2 Experimental Results

A key parameter of NEMS resonators is their quality factor Q, which is the ratio of the stored energy to the dissipation per oscillation cycle, and is inversely proportional to the resonance line width. The dissipation can be linear, in which Q is amplitude-independent, or non-linear, [38, 10] in which Q is amplitude-dependent. [36]

Here, we measure both linear and nonlinear damping in monolayer and few-layer electrically-driven graphene drum resonators. Addressing the linear damping

regime first, we show that for sufficiently small drive voltage V_{sd}, Q follows a $1/T$ law in temperature T down to low temperatures. A canonical model for dissipation considers a primary oscillator coupled to a bath of environmental oscillators. [43, 44, 45] However, membranes have a complex thermodynamic behavior that has been well-studied in the literature, including in graphene, for example in ref. [46], that may exhibit new phenomena. Recently Duffing forces in conjunction with fluctuations have been found that could account for Q in nanotube resonators. [11] However, based on the measured Duffing forces in our samples, this phenomenon is too small is account for the observed Q. Other recent work has shown that thermal fluctuations in the fundamental mode's effective spring constant and resonance frequency produced by coupling to thermally excited out of plane modes can potentially determine the linewidth in graphene [47] or carbon nanotube [48] resonators, and predict $Q \propto 1/T$. However, ref. [48], calculates the Q in SWNTs from tension fluctuations, but does not explicitly take into account the nonlinear mode coupling, and is not immediately applicable to two-dimensional (2D) membranes such as graphene. In ref. [47] a tensioned membrane is not directly considered, which is most relevant to typical experimental conditions.

Here we conceptually divide the graphene sheet modes into "fast" and "slow" modes (see e.g. ref. [49]) interacting through nonlinear coupling. The slow mode behavior is reminiscent to that found in NMR, in which Larmor frequency fluctuations from fluctuating environmental magnetic fields broaden the resonance as compared to isolated nuclei. [50, 51] The frequency-dependent oscillator susceptibility has an imaginary dissipative part with a characteristic width $\Gamma \propto T$ on the same scale as the resonance width, similar to a damped oscillator with a damping force $F_d = -m\Gamma\dot{z}$, where z is the oscillator coordinate and m its mass.

Under steady-state conditions the slow mode motion modulates the sheet tension, transferring energy to the fast modes via parametric driving. This produces a viscous damping force $\propto T^2$. The fluctuation-driven broadening is expected to dominate the frictional broadening for typical experimental conditions, consistent with our observation of $\propto 1/T$ behavior of Q. We find that the measured Q varies with the gate voltage V_g, which we attribute to the changing tension as well as electrostatic forces.

We have studied 12 devices in total, but found observable resonances and obtained Q vs. T data from 4 devices, 2 trilayer and 2 monolayer. Fig. 5.1a shows a scanning electron microscope (SEM) image of a trilayer graphene resonator, suspended over a hole in an oxidized highly doped Si wafer with attached source and drain electrodes. Except where otherwise noted, all data shown is from this device. The Si wafer acts as a back gate. A schematic diagram is shown in Fig. 3.2. A frequency-modulated (FM) ac source-drain voltage V_{sd} at carrier frequency f with modulation frequency f_L excites the vibration. This produces a current I_{mix} at frequency f_L proportional to the frequency derivative of the real part of the mechanical response, [8, 10, 25] detected using a lock-in amplifier.

Fig. 5.1b shows the current plotted as a colorscale versus gate voltage V_g and f. Bright features correspond to resonances with gate voltage tunable frequency. The black curve in Fig. 5.1c shows a line trace along the dotted line in Fig. 5.1b, showing a maximum at the resonance frequency f_0. The maximum is surrounded by two minima [8, 10] with frequency spacing δf, equal to the resonance frequency width; $Q = f_0/\delta f$. [10]

Fig. 5.2a shows the resonator frequency tunability, originating from both electrostatic force gradient softening as well as the increase in tension with V_g. [31, 32] A change in concavity of the f_{res} vs. V_g relationship is expected for sufficiently large

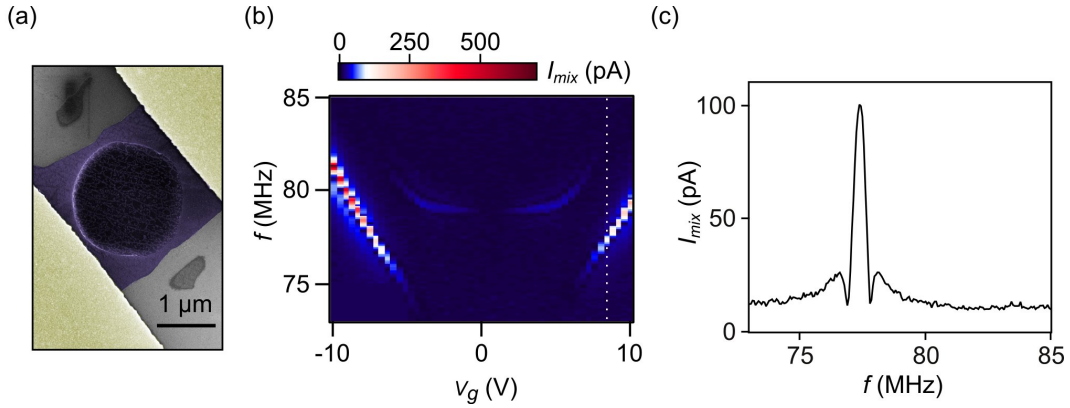

Figure 5.1: Few-layer graphene resonator device image and nanomechanical resonance data. (a) Scanning electron image of a completed graphene drumhead resonator device. Devices are fabricated by exfoliation of graphene layers onto an array of holes etched into an oxidized Si wafer. To avoid collapsing the device when spinning resist on, a layer of PMMA is prepared on a layer of water soluble polyvinyl alcohol, lifted off in water then applied dry to the substrate and baked on. Areas are then exposed and developed, unwanted material is removed using a reactive ion etch. Finally, leads are attached using electron beam lithography and then the device is dried using a critical point dryer. (b) Color plot of signal from FM technique versus gate voltage V_g and drive frequency. The lowest frequency mode visible is taken to be the fundamental resonant mode. (c) Line trace along the dotted line in (b) at $V_g = 8$ V showing the resonance signal.

gate voltages. [23, 31] However, as we do not observe such a change we use a small V_g approximation to fit the data over the entire V_g range. The solid curve is a fit to the function (eq. 3.9)

$f_{res} = \sqrt{\left(2\pi T_0 - \frac{\epsilon\pi r_0^2}{3d^3}V_g^2 + aV_g^4\right)/m_{eff}}/(2\pi)$, yielding the tension T_0 at $V_g = 0$, m_{eff}, and a, which describes the tension increase with V_g. We obtain $T_0 = 6.9 \times 10^{-2}$ N/m, $m_{eff} = 2.5 \times 10^{-18}$ kg, and $a = 1.13 \times 10^{-6}$ N/V^4·m.

For small V_{sd}, the damping is linear and δf is nearly constant, but δf begins to visibly increase as V_{sd} increases above ∼9 mV, as shown in Fig. 5.2b. This increase in δf is a signature of nonlinear damping. [10] In the linear damping regime, Q follows a $1/T$ dependence over more than a decade of measured temperatures, denoted by the dashed line, down to $T = 16$ K as shown at various V_g in Fig. 5.2c. In previous work, a larger exponent power law $\sim 1/T^2$ was observed in conjunction with a saturation to a lower

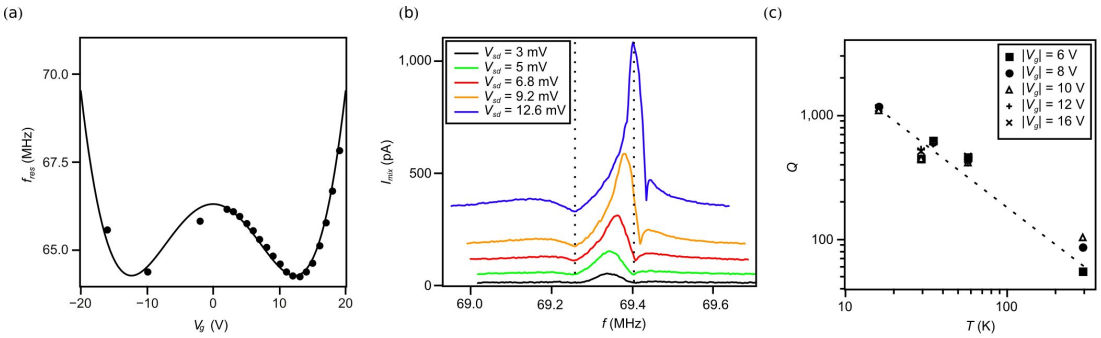

Figure 5.2: Quality factor and resonance frequency of the lowest-frequency mode. (a) Resonant frequency f_{res} vs. V_g plotted as black circles. Solid line fit to the equation described in the text. (b) FM mixing signal vs. frequency for different source-drain drive voltages V_{sd} taken at $T = 57$ K and $V_g = 20$ V. The curves have been offset horizontally to align the left minima and vertically for clarity. Each line trace shows a maximum at resonance surrounded by two minima. The resonance frequency width is determined by the spacing between the minima. Above $V_{sd} \sim 9$ mV, the frequency width increases visibly because of the presence of nonlinear damping. Above $V_{sd} \sim 5$ mV, the resonance frequency shifts upwards from the presence of an anharmonic force on the oscillator. (c) Main panel: Log-log plot of measured quality factor vs. temperature for different gate voltages. The straight line is a guide to the eye proportional to $1/T$. Frequency values for $V_g = 8$V are: $T = 16.0$ K, $f = 75.6$ MHz; $T = 29.5$ K, $f = 71.2$ MHz; $T = 35.0$ K, $f = 68.1$ MHz; $T = 57.0$ K, $f = 66.2$ MHz; $T = 296.0$ K, $f = 71.4$ MHz.

exponent $\sim 1/T^{0.3}$ below $T \sim 100$ K, [23, 25] However, variables such as membrane tension, which could in principle affect Q were not controlled or accounted for, nor were the effects of nonlinear damping.

Recent work considers potential dissipation mechanisms, including thermoelastic losses and currents due to strain-induced dynamic synthetic fields. [52, 53, 39] Other mechanisms, for example clamping losses [54] and surface state dissipation [55] have also been considered. However, none of these proposed mechanisms can account for the magnitude, size, [56] and temperature dependence of Q. Here, we consider a tensioned elastic membrane, with an isotropic strain c from the uniform tension $T_0 = 2c(\lambda + \mu)$, where μ is the shear modulus and λ is Lamé's first constant. The slow modes couple to the fast modes since out of plane bending fluctuations modulate the sheet tension. Fast mode

thermal fluctuations stochastically shift the slow modes' effective spring constant, broadening their resonances. This yields for the fundamental mode with resonance frequency $\omega_0 = 2\pi f_0$ (eq. 5.15)

$$Q = \frac{\xi T_0^{3/2} r_0}{k_B T} \sqrt{\frac{\kappa}{E}} \tag{5.1}$$

where $\xi \approx 6.84$ is a numerical factor, $E = N^2(\lambda^2 + 4\lambda\mu + 4\mu^2) \approx N^2 \times 1.1 \times 10^5$ $(\mathrm{N/m})^2$ with N the number of layers, $\kappa \approx 10^{-16}$ Nm is the bending modulus, T_0 the tension, k_B is the Boltzmann constant, and r_0 is the resonator radius.

Since the frequency does not change significantly as the temperature is varied, we assume that the tension is approximately constant [31] for this sample. For some samples the frequency variation is more significant. Fig. 5.3a inset shows the measured Q for all 4 samples, two trilayer samples T1 and T2 and 2 CVD-grown monolayers M1 and M2. The dotted line shows a $1/T$ trend as a guide to the eye. Some samples follow it more closely, while others, for example sample T2, follow a somewhat different Q vs. T scaling. To fit the data to eq. 5.1 we write the tension T_0 as $T_0 = m_{eff}\omega_0^2/(2\pi)$. Then we re-arrange eq. 5.1 and define $\bar{Q} = \frac{Qk_B}{\xi\omega_0^3 r_0 m_{eff}^{3/2}}\sqrt{\frac{E}{\kappa}}$. Note that $\bar{Q}$ depends only on measured and known parameters. According to eq. 5.1 $\bar{Q} = 1/T$. Plotting the measured $\bar{Q}$ vs. T along with the curve $1/T$ we find that the data follows the expected $1/T$ dependence for all 4 samples. No free parameters are used in the plot. Within the experimental sample-dependent variation of the Q vs. T, the characteristic $1/T$ behavior and magnitude of the data is described by eq. 5.1. This provides strong evidence that frequency broadening from nonlinear coupling to thermally excited modes determines the observed quality factor. The predicted Q increases for increasing size as $\propto r_0$, as observed, [56] providing additional evidence for this picture. As as result, this mechanism is expected to dominate in micro- or nanoscale resonators.

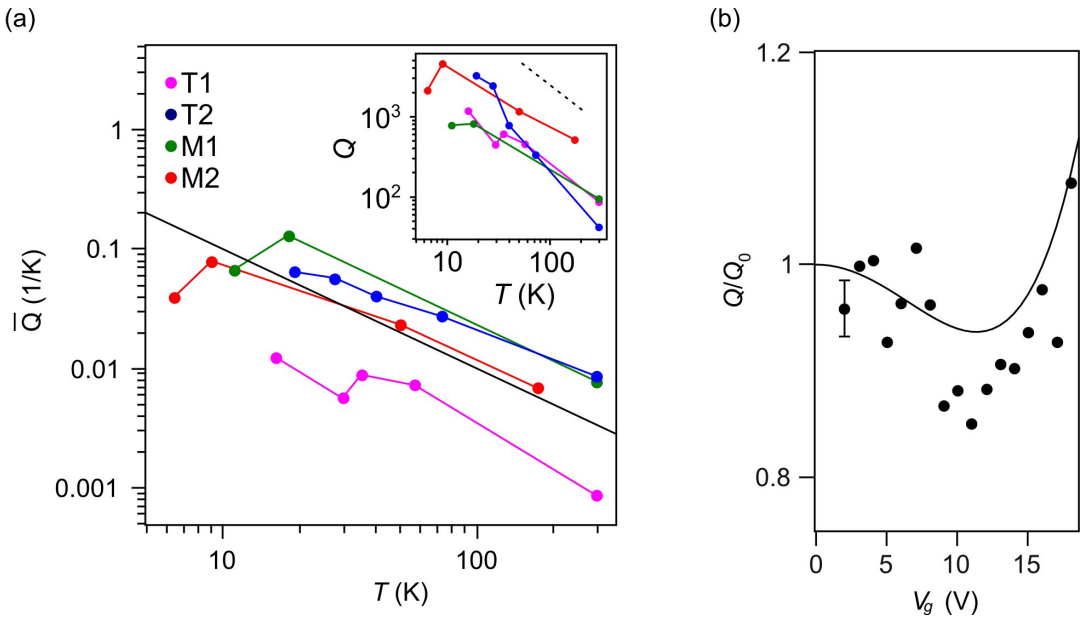

Figure 5.3: Quality factor temperature dependence and gate voltage tunability of the resonance frequency and quality factor at $T = 57$ K. (a) Main Panel: Scaled quality factor $\bar{Q}$ as described in the text vs. T. The masses used for scaling are: M1, 0.8 m_m, M2, 5.2 m_m, T1, 3.2 m_m, T2, 0.7 m_m where m_m is the monolayer effective mass. The masses of T1, T2, and M1 were obtained by fitting to eq. S9 to the measured f_{res} vs. V_g curves, while the mass of M2 was obtained using results for pressurized membranes under large load because only large V_g data was available, and obtaining an unambiguous mass using eq. S9 was difficult. Blue and magenta, trilayer devices, green and red, single layer devices. Solid line: $1/T$, plotted without free parameters. Inset: Q vs. T for the same samples. (b) Q vs. V_g for T1 plotted as solid circles normalized to the extrapolated value at $V_g = 0$. Solid curve plot of theoretical model without free parameters as described in Section 5.3.3.

Q depends weakly on V_g as shown in Fig. 5.3b. Previous work has reported a V_g-dependence of Q in carbon nanotube because of single-electron charging effects. [57, 58] However, as no Coulomb blockade is observed in our samples, we extend the above model to account for the electrostatic forces from an applied V_g, which change the frequencies of the fundamental and excited modes and the resulting intermodal perturbation of the fast modes on the slow modes. Fig. 5.3b shows the measured $Q/Q(V_g = 0)$ vs. V_g, while the solid line shows the theoretically expected curve (Section 5.3.3) using the parameters obtained from Fig. 5.2a, without performing a fit. The agreement is good considering the lack of free parameters in the model curve, providing further evidence

that frequency broadening through nonlinear mode coupling determines Q in graphene resonators. A similar analysis for room temperature data is shown in Fig. 5.4, where both the measured Q modulation and frequency tuning with V_g are larger than at low temperature. More work will be required to fully understand the detailed changes of these curves with temperature. Nevertheless, the order of magnitude of the measured and predicted effects are similar, suggesting that the model captures the basic physics of the Q and f_{res} tunability with V_g.

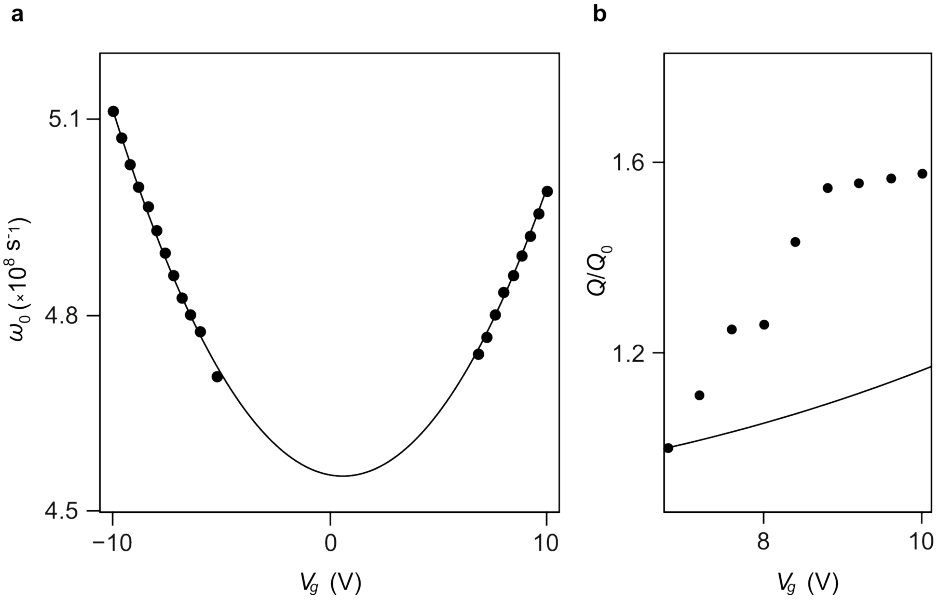

Figure 5.4: (a) Plot of the frequency vs. gate voltage measured at room temperature for the device T1 taken with $V_{sd} = 70$ mV. The solid line is a fit to a 2nd order polynomial. Since the dependence of the frequency on V_g is relatively strong, we assume that the frequency is dominated by the tension and neglect electrostatic effects. The tension is then related to the frequency by $\omega = \sqrt{2\pi T_0/m}$. (b) The measured Q vs. V_g is shown as the black circles. We then use the method discussed in section S5 to compute the expected Q, which is plotted as the solid line. Since Q was not easily extrapolated back to zero frequency, the data and theory were matched at the lowest measured V_g.

Within this model, while the frequency broadening Γ does not correspond to a viscous damping force, in steady state under a sinusoidal drive it produces an average dissipation rate that is the same as if Γ originated from such a viscous force. This implies that the root mean square amplitude of the motion must become large

enough for conventional friction to dissipate the input power from the drive (eq. 5.19). We calculate the energy transfer rate to the fast modes by assuming that the tension modulations during oscillation parametrically drive the fast modes in conjunction with a Langevin force. This produces a calculated frictional damping force proportional to velocity that is $\propto T^2$ and is characteristically smaller than the frequency broadening given above for typical device parameters and measurement conditions (eq. 5.18). This is consistent with our observation of $\propto T$ behavior for the linewidth.

5.3 Theoretical Anslysis

Recent theoretical work has suggested that the linewidth in carbon nanotube[48] or graphene [47] resonators could result from fluctuations in the tension caused by the thermally excited modes. However, the work on carbon nanotubes considers tension fluctuations, which is not immediately applicable to two-dimensional membranes. It also does not consider the temporal behavior of the fluctuations, which is important for determining the contribution of motional narrowing to the linewidth. The work on graphene does not explicitly consider a tensioned membrane, which is relevant to our experimental situation. As a result, we first consider a model in which the modes of the sheet are divided conceptually into "fast" and "slow" modes by their frequency. As the fast modes oscillate due to thermal excitation, they perturb the slow modes' resonance frequency through nonlinear coupling. Later in this section we consider dissipative line broadening due to intermodal energy transfer. This contribution to line broadening is found to be small compared to the frequency fluctuation broadening for our device geometry and typical parameters.

We now focus specifically in the fluctuations in the effective spring constant of the fundamental mode. We take its equation of motion as that of a harmonic oscillator:

$$\frac{d^2z}{dt^2} + \omega_0^2[1 + x(t)]z = F_{ext}(t)/m, \tag{5.2}$$

where z is the displacement, t is the time, ω_0 is the characteristic frequency, $F_{ext}(t)$ is any external force applied to the oscillator, m the oscillator mass, and $x(t)$ is a random function with a mean of zero and autocorrelation function $R(\tau) = \langle x(t)x(t+\tau)\rangle$ which represents the frequency fluctuations $\delta\omega$ due to the fast modes. Since the frequency in the oscillator equation is a stochastic variable, the physical situation is reminiscent of that in nuclear magnetic resonance (NMR) in which a precessing spin undergoes Larmor frequency fluctuations due to fluctuating environmental magnetic fields.[50, 51] For this situation, this stochastic equation was successfully treated using the method of model coefficients in which the random variable is assumed to have a specific known behavior that produces an exact result for the mean solution of equation 5.2.[50, 51] (see also ref. [59] for review.)

Two limits exist with different behavior, determined by comparing the magnitude of the frequency fluctuations $\delta\omega$ with the inverse correlation time of the fluctuations ν. If $\nu << \delta\omega$ then the frequency fluctuations are sufficiently slow that the full intrinsic linewidth $\Gamma_i = \delta\omega$ results. On the other hand, if $\nu >> \delta\omega$ the oscillator averages the fluctuations, resulting in a narrower linewidth Γ_{mn} than $\delta\omega$, which is the regime of motional narrowing in NMR.

The spectral density of the frequency fluctuations in x, $S(\omega)$, defined as

$$S(\omega) = \int_{-\infty}^{\infty} R(\tau)e^{i\omega\tau}d\tau,$$

at zero frequency can be written as $S(0) = \Delta t\langle x^2\rangle = 4\Delta t\langle\delta\omega^2\rangle/\omega_0^2$, where Δt is a characteristic correlation time for the fluctuations. Setting $\Delta t = 1/\nu$, the frequency

width Γ_{mn} is given by [50, 51, 59]

$$\Gamma_{mn} = \frac{\omega_0^2}{2} S(0), \tag{5.3}$$

The linewidth is therefore

$$\Gamma = \min\left[\Gamma_{mn}, \Gamma_i\right] \tag{5.4}$$

To compute Γ_i and Γ_{mn}, we begin by Fourier transforming the energy given in eq. 3.1, by using the Fourier transform relations

$$\begin{aligned} h(\vec{q}) &= \int h(\vec{x}) e^{-i\vec{q}\cdot\vec{x}} d^2\vec{x} \\ h(\vec{x}) &= \int h(\vec{q}) e^{i\vec{q}\cdot\vec{x}} \frac{d^2\vec{q}}{(2\pi)^2} \end{aligned}$$

which yields

$$\begin{aligned} \mathcal{U} &= \int \frac{d^2\vec{q}}{(2\pi)^2} h^*(\vec{q}) h(\vec{q}) \left[c(\lambda+\mu) q^2 + \frac{1}{2}\kappa q^4 \right] \\ &+ \int \frac{d^2\vec{q}_1 d^2\vec{q}_2 d^2\vec{q}_3 d^2\vec{q}_4}{(2\pi)^6} h^*(\vec{q}_1) h^*(\vec{q}_2) h(\vec{q}_3) h(\vec{q}_4) u(\vec{q}_1, \vec{q}_2, \vec{q}_3, \vec{q}_4) \\ &\times \delta(\vec{q}_4 + \vec{q}_3 - \vec{q}_2 - \vec{q}_1) \end{aligned} \tag{5.5}$$

where $u(\vec{q}_1, \vec{q}_2, \vec{q}_3, \vec{q}_4)$ is given by

$$u(\vec{q}_1, \vec{q}_2, \vec{q}_3, \vec{q}_4) = \frac{1}{16}\lambda[(\vec{q}_1 \cdot \vec{q}_3)(\vec{q}_2 \cdot \vec{q}_4) + (\vec{q}_1 \cdot \vec{q}_4)(\vec{q}_2 \cdot \vec{q}_3)] + \frac{1}{4}\mu(\vec{q}_1 \cdot \vec{q}_2)(\vec{q}_3 \cdot \vec{q}_4)$$

If u were zero then $\mathcal{U}$ would be that of noninteracting quadratic normal modes. The u function thus describes the nonlinear modal interactions to 4th order in h. For a given configuration of $h(q)$ values the shift in the effective spring constant of the mode with wavevector $\vec{\bar{q}}$ is determined by adding a cosine wave to the sheet and collecting quadratic terms in its amplitude A_m. The height Fourier components then become

$$h_m(\vec{q}) = h(\vec{q}) + \frac{(2\pi)^2 A_m}{2}[\delta(\vec{q} - \vec{\bar{q}}) + \delta(\vec{q} + \vec{\bar{q}})]$$

Then

$$\begin{aligned}
\delta\mathcal{U} &= \int \frac{d\vec{q}_1 d\vec{q}_2 d\vec{q}_3 d\vec{q}_4}{(2\pi)^6}\left(h^*(\vec{q}_1)+\frac{(2\pi)^2 A_m}{2}[\delta(\vec{q}_1-\vec{\bar{q}})+\delta(\vec{q}_1+\vec{\bar{q}})]\right) \\
&\times \left(h^*(\vec{q}_2)+\frac{(2\pi)^2 A_m}{2}[\delta(\vec{q}_2-\vec{\bar{q}})+\delta(\vec{q}_2+\vec{\bar{q}})]\right) \\
&\times \left(h(\vec{q}_3)+\frac{(2\pi)^2 A_m}{2}[\delta(\vec{q}_3-\vec{\bar{q}})+\delta(\vec{q}_3+\vec{\bar{q}})]\right) \\
&\times \left(h(\vec{q}_4)+\frac{(2\pi)^2 A_m}{2}[\delta(\vec{q}_4-\vec{\bar{q}})+\delta(\vec{q}_4+\vec{\bar{q}})]\right) \\
&\times u(\vec{q}_1,\vec{q}_2,\vec{q}_3,\vec{q}_4)\delta(\vec{q}_1+\vec{q}_2-\vec{q}_3-\vec{q}_4) \qquad (5.6)
\end{aligned}$$

Collecting the terms quadratic in A_m, the shift is related to integrals over the mean squares of the modal displacements. In thermal equilibrium, the mean square modal displacements undergo thermal fluctuations, broadening the frequency response. The contribution of a given fast mode with frequency ω' to $S(0)$, labeled $S_{\omega'}(0)$ is

$$S_{\omega'}(0) = \frac{4}{\omega_0^2}\langle\delta\omega^2\rangle_{\omega'}\Delta t_{\omega'},$$

where $\langle\delta\omega^2\rangle_{\omega'}$ is the mean square fluctuation in the slow mode with frequency ω_0 caused by the fast mode with frequency ω', and $\Delta t_{\omega'}$ is the characteristic time scale of those fluctuations. Since the bandwidth of a harmonic oscillator with characteristic frequency ω' and quality factor $Q_{\omega'}$ is $\omega'/Q_{\omega'}$ this gives $\Delta t_{\omega'} \approx Q_{\omega'}/\omega'$. We then have

$$S(0) = \int S_{\omega'}(0)\rho(\omega')d\omega', \qquad (5.7)$$

where $\rho(\omega')$ is the density of modes at frequency ω'.

The quantity $\langle\delta\omega^2\rangle_{\omega'}$ is computed by first computing the total $\langle\delta\omega^2\rangle$ by squaring equation 5.6 and thermally averaging it with respect to the quadratic part of $\mathcal{U}$, using the relation that $\frac{1}{2}\delta k_{eff}/k_{eff} = \delta\omega/\omega$, where k_{eff} is the slow mode effective

spring constant. To perform the thermal average, we use the relation that

$$\begin{aligned}\langle h^*(\vec{q}_4)h^*(\vec{q}_3)h(\vec{q}_2)h(\vec{q}_1)\rangle_{0>} &= \frac{1}{4}\frac{(2\pi)^2\delta(\vec{q}_4-\vec{q}_2)}{\beta(A\vec{q}_4^2+B\vec{q}_4^4)}\frac{(2\pi)^2\delta(\vec{q}_3-\vec{q}_1)}{\beta(A\vec{q}_3^2+B\vec{q}_3^4)} \\ &+ \frac{1}{4}\frac{(2\pi)^2\delta(\vec{q}_3-\vec{q}_2)}{\beta(A\vec{q}_3^2+B\vec{q}_3^4)}\frac{(2\pi)^2\delta(\vec{q}_4-\vec{q}_1)}{\beta(A\vec{q}_4^2+B\vec{q}_4^4)} \\ &+ \frac{1}{4}\frac{(2\pi)^2\delta(\vec{q}_4+\vec{q}_3)}{\beta(A\vec{q}_4^2+B\vec{q}_4^4)}\frac{(2\pi)^2\delta(\vec{q}_2+\vec{q}_1)}{\beta(A\vec{q}_2^2+B\vec{q}_2^4)} \end{aligned} \tag{5.8}$$

where $A = c(\lambda+\mu)$ and $B = \frac{1}{2}\kappa$ are elastic constants that define the quadratic part of $\mathcal{U}$, and $\beta = 1/k_BT$, with k_B the Boltzmann constant and T the temperature. (See for example, ref. [49].) The factor of 1/4 and the extra term compared to the work in ref. [49] arise because the height is real, so $h(\vec{q}) = h^*(-\vec{q})$. The result is that the total mean square frequency fluctuations are given by

$$\langle\delta\omega^2\rangle = \frac{27\bar{A}\bar{q}^4\omega_0^2E}{512\beta^2k_{eff}^2}\int\frac{dq}{2\pi}\frac{q^5}{(Aq^2+Bq^4)^2} = \frac{27\bar{A}\bar{q}^4\omega_0^2E}{2048\pi\beta^2k_{eff}^2AB}, \tag{5.9}$$

where $E = N^2(\lambda^2+4\lambda\mu+4\mu^2)$ is an elastic constant and N is the number of layers. Converting this to an integral over frequency using the density of modes obtained from the frequency relation $\omega = \sqrt{2(Aq^2+Bq^4)/\sigma}$ gives,

$$\langle\delta\omega^2\rangle = \frac{27\bar{q}^4\omega_0^2E}{512\beta^2k_{eff}^2}\int d\omega'\left(\frac{-A+\sqrt{A^2+2\sigma\omega'^2B}}{B}\right)^2\frac{1}{\sigma^2\omega'^4}\rho(\omega')$$

From this we find that $S_{\omega'}(0)$ is given by

$$S_{\omega'}(0) = \frac{27\bar{q}^4E}{128\beta^2k_{eff}^2}\left(\frac{-A+\sqrt{A^2+2\sigma\omega'^2B}}{B}\right)^2\frac{Q_{\omega'}}{\sigma^2\omega'^5} \tag{5.10}$$

5.3.1 Fast mode behavior

Completing the calculation requires finding the $Q_{\omega'}$ in eq. 5.10. Similar to the fundamental mode, the linewidth and $Q_{\omega'}$ of the fast modes also have two potential sources, frequency fluctuations and energy damping. However, frequency fluctuations are ineffective at causing the fast mode amplitude fluctuations that produce the frequency

shifts in the fundamental mode. These amplitudes fluctuate on a timescale determined by the modal energy damping rate. Therefore a determination of the energy damping rate for the fast modes is necessary to find the appropriate $Q_{\omega'}$. A variety of energy relaxation mechanisms are possible including coupling to electrons, clamping losses, or to in-plane phonons which are expected to produce relatively high quality factors $\sim 10^5$ or higher for geometries similar to our experiment. [39, 53, 52] Here, we also consider a mechanism of energy transfer from one vibrational mode to another. The tension fluctuations within the sheet give rise to spatially inhomogeneous wave velocity fluctuations. Such fluctuations also scatter the standing waves of the sheet in a manner similar to Rayleigh scattering. However, because the fluctuations are time dependent, scattering among modes with different frequencies is expected to occur. We compute the energy damping rate of the fast modes due to such scattering using perturbation theory for the wave equation. The Lagrange density for the membrane is

$$\mathcal{L} = \frac{1}{2\sigma}\left(\frac{\partial h}{\partial t}\right)^2 - A(\nabla h)^2 - \frac{1}{8}(\lambda + 2\mu)(\nabla h)^4 - B(\nabla^2 h)^2.$$

Neglecting bending for modes that are longer wavelength than the cutoff $\sqrt{A/B}$ the equation of motion is

$$\sigma\frac{\partial^2 h}{\partial t^2} - A\nabla^2 h - \left\{\frac{1}{4}(\lambda + 2\mu)\left[\nabla(\nabla h)^2 \cdot \nabla h + (\nabla h)^2\nabla^2 h\right]\right\} = 0$$

We consider the term in braces as a perturbation. The unperturbed problem has time-periodic solutions satisfying the eigenvalue equation

$$\nabla^2 h + k_l^2 h = 0,$$

where k_l^2 is the lth eigenvalue for each solution. The perturbation scatters a given mode into other modes, giving it a finite lifetime. We denote the instantaneous state of the

membrane as a superposition of eigenmodes $\Psi_l = 1/\sqrt{A}e^{i\vec{k}_l\cdot\vec{x}}$, where l is the mode index.

$$h(t) = \sum_l \Psi_l e^{-i\omega_l t} c_l(t),$$

where $c_l(t)$ are coefficients for which we want to obtain a differential equation. Substituting the expression for $h(t)$ into the equation of motion, we get

$$\sum_l \Psi_l e^{-i\omega_l t}\left\{-2i\omega_l\dot{c}_l(t) + \ddot{c}_l(t) + \frac{1}{4\sigma}(\lambda+2\mu)\left[2(\vec{k}_l\cdot\nabla h)^2 + (\nabla h)^2 k_l^2\right]\right\} = 0$$

Taking the inner product denoted by

$$\langle f, g\rangle = \int d^2\vec{x} f^*(\vec{x}) g(\vec{x})$$

of this equation with $\Psi_m e^{i\omega_m t}$ yields

$$-2i\omega_m\dot{c}_m(t) + \ddot{c}_m(t) = \sum_l \frac{1}{4\sigma}(\lambda+2\mu)\langle\Psi_m, [2(\vec{k}_l\cdot\nabla h)^2 + (\nabla h)^2 k_l^2]\Psi_l\rangle e^{i\omega_{lm}t} c_l(t)$$

where $\omega_{lm} = \omega_m - \omega_l$. Assuming only one of the modes has non-negligible amplitude so that $c_l(t) \approx 0 << c_n(t)$ except for one particular mode n, the equation becomes

$$-2i\omega_m\dot{c}_m(t) + \ddot{c}_m(t) = \frac{1}{4\sigma}(\lambda+2\mu)\langle\Psi_m, [2(\vec{k}_n\cdot\nabla h)^2 + (\nabla h)^2 k_n^2]\Psi_n\rangle e^{i\omega_{nm}t} c_n(t)$$

For large times, growing amplitude solutions for c_m occur when the right hand side of the above includes zero frequency components. In this case the $\ddot{c}_m$ term yields a fast oscillating homogeneous solution and no time-averaged energy transfer so long as that the perturbation is sufficiently weak that $c_n(t)$ varies slowly on the time scale of $1/\omega_m$. We will see below that this condition is satisfied to first order. Neglecting this term, which makes a negligible contribution to the slowly growing inhomogeneous term and energy transfer, the equation then becomes essentially the same as time-dependent perturbation theory in quantum mechanics. The lowest order solution is

$$c_m = \frac{i}{2\omega_m}\int_0^t \frac{c_n(0)}{4\sigma}(\lambda+2\mu)\left[\langle\Psi_m, (\nabla h)^2 k_n^2\Psi_n\rangle + \langle\Psi_m, 2(\vec{k}_n\cdot\nabla h)^2\Psi_n\rangle\right] e^{i\omega_{nm}t'} dt' \tag{5.11}$$

The first matrix element term in the brackets results from velocity fluctuations. The thermal expectation value of the second term is the same as the first. Therefore we replace the entire integrand with twice the first term. Factoring out the k_n the matrix element is therefore

$$V_{mn} = \langle \Psi_m, (\nabla h)^2 \Psi_n \rangle = \frac{1}{\bar{A}} \int d^2\vec{x} (\nabla h)^2 e^{i(\vec{k}_n - \vec{k}_m)\cdot\vec{x}} \tag{5.12}$$

Thus the matrix element is the Fourier transform of $(\nabla h)^2$ at the scattering wave vector $\Delta\vec{k} = \vec{k}_n - \vec{k}_m$. This should depend on the squared height modulations with wavevector $\Delta\vec{k}$, which have a characteristic frequency $\omega(\Delta\vec{k})$.

The energy transfer rate is determined from eq. 5.11.

$$\frac{1}{E_n}\frac{dE_m}{dt} = \frac{d}{dt}\frac{k_{eff,m}|c_m(t)|^2}{k_{eff,n}|c_n(0)|^2} = \frac{k_{eff,m}}{k_{eff,n}}\frac{k_n^4(\lambda+2\mu)^2}{64\omega_m^2}\int_0^t V_{mn}(t)V_{mn}^*(t)e^{i\omega_{mn}\tau}d\tau + c.c.$$

Taking the thermal average gives

$$\left\langle \frac{1}{E_n}\frac{dE_m}{dt} \right\rangle = \frac{k_{eff,m}}{k_{eff,n}}\frac{k_n^4(\lambda+2\mu)^2}{64\omega_m^2}\int_0^t \langle V_{mn}(t)V_{mn}^*(t)\rangle e^{i\omega_{mn}\tau}d\tau + c.c.$$

for large t, this becomes

$$\left\langle \frac{1}{E_n}\frac{dE_m}{dt} \right\rangle = \frac{k_{eff,m}}{k_{eff,n}}\frac{k_n^4(\lambda+2\mu)^2}{32\omega_m^2}\Re[S_{V_{mn}}(\omega_{mn})], \tag{5.13}$$

where $S_{V_{mn}}$ is the power spectral density of V_{mn} at frequency ω_{mn}. This should be peaked at frequency $\omega(\Delta\vec{k})$ with width $\sim \omega(\Delta\vec{k})$, while the area under the peak vs. frequency is $|V_{mn}|^2$. We therefore expect an analog of Fermi's golden rule to apply, i.e.

$$\begin{aligned}\left\langle \frac{1}{E_n}\frac{dE_m}{dt} \right\rangle &= \frac{k_{eff,m}}{k_{eff,n}}\frac{k_n^4(\lambda+2\mu)^2}{32\omega_m^2}|V_{mn}|^2\delta[\omega(q_n) - \omega(q_m) \pm \omega(q_n - q_m)] \qquad (5.14)\\ &= \frac{k_n^2(\lambda+2\mu)^2}{32\sigma^2u^2}|V_{mn}|^2\delta[\omega(q_n) - \omega(q_m) \pm \omega(q_n - q_m)],\end{aligned}$$

where $k_{eff,n} \approx \bar{A}Aq_n^2$, u is the wave velocity and

$$\omega(q) = \sqrt{\frac{2(Aq^2 + Bq^4)}{\sigma}},$$

where the final result for the total normalized energy loss rate is obtained by an integration over the final states. Evaluating eq. 5.14 numerically for typical parameters yields $Q_f \sim 10^4$ at room temperature and $\sim 10^6$ at low temperature, scaling as $1/T^2$. Note that using a broader frequency function than a δ-function to account for the finite frequency width of $S_{V_{mn}}$ leads to a larger predicted Q, thus the above estimates constitute a lower bound on Q from this mechanism. Having found Q_f, we must now compare Γ_{mn} to Γ_i to determine whether motional narrowing is expected to be important. To first evaluate Γ_i we use eq. 5.9 using $k_{eff} \approx \bar{A}Aq^2$, yielding

$$Q_i = \frac{\xi T_0^{3/2} r_0}{k_B T} \sqrt{\frac{\kappa}{E}} \tag{5.15}$$

where $\xi \approx 6.84$ is a numerical factor, $E = N^2(\lambda^2 + 4\lambda\mu + 4\mu^2) \approx N^2 \times 1.1 \times 10^5$ (N/m)^2 with N the number of layers, $\kappa \approx 10^{-16}$ Nm is the bending modulus, T_0 the tension, k_B is the Boltzmann constant, and r_0 is the resonator radius. Evaluation of eq. 5.7 using $Q_{\omega'} = Q_i \sim 100 - 1000$, obtained from eq. 5.15 using typical parameters gives $\Gamma_i \sim \Gamma_{mn}$. Since we have instead $Q_{\omega'} = Q_f >> Q_i$, the fluctuations are sufficiently slow so that we find that $\Gamma_i << \Gamma_{mn}$ and thus the static limit is the relevant one, since other energy damping mechanisms [39, 53, 52] such as clamping loss mentioned above are also expected to produce significantly larger Q values than Q_i. Therefore we expect the effects of motional narrowing to be minimal and the measured quality factor should follow the relation given for Q_i, eq. 5.15, as observed.

5.3.2 Energy Transfer to fast modes from fundamental mode

In the steady state, vibrations of the fundamental mode produce a periodic modulation of the membrane tension with frequency ω_0 and amplitude $\delta\omega$. Each fast mode, approximated as an independent oscillator with frequency ω_f, then has its frequency modulated

at frequency ω_0. The equation of motion for each fast mode can then be written as [60]

$$\ddot{z} + \Gamma\dot{z} + \omega_f^2[1 + \epsilon\cos(\omega_0 t)]z = \sqrt{\Gamma D}\xi(t) \tag{5.16}$$

where $D = k_B T/m_{eff}$ is a diffusion constant and $\sqrt{\Gamma D}\xi(t)$ is a delta-correlated stochastic function that models the Langevin force. In the steady state the root mean square amplitude of the oscillator is given by (assuming $Q >> 1$ and neglecting terms of order higher than ϵ^2 ($\epsilon = 2\delta\omega_f/\omega_f$ or terms with frequency $2\omega_0$ or higher)

$$\sigma_{zz} = \frac{D}{\omega_f^2} + \frac{3D}{2\omega_f^4}\delta\omega^2 - 2\delta\omega\frac{D}{\omega_f}\left[\frac{1}{2\omega_f^2}\cos(\omega_0 t) + \frac{\Gamma}{4\omega_0\omega_f^2}\sin(\omega_0 t)\right].$$

Here we neglect frequency broadening, since we are in the static limit where $\nu << \delta\omega$, and the moments of the solutions $\sigma_{zz}(\omega_f)$ corresponding to the equations with different ω_f in the ensemble would be expected to be very similar since $\omega_0 << \omega_f$. When the parametric drive is zero, the modal amplitude thermal fluctuations are given by $\sigma_{zz} = D/\omega_f^2$. For finite parametric drive caused by the vibrations in the fundamental mode, the relative frequency modulations $\delta\omega_f/\omega_f = \frac{1}{2}\delta T_0/T_0$ and are therefore the same for each fast mode. The sine and cosine terms thus represent a coherent response of all the fast modes to the vibration of the fundamental mode. Thus the fundamental mode vibration modulates the sheet tension at the same frequency ω_0. Since the membrane is under electrostatic pressure, the changing tension displaces the equilibrium point of the fundamental mode, which corresponds to a force $z_0\delta k_{eff}$. The term proportional to the sine therefore yields a frictional damping force on the fundamental mode that is proportional to its velocity.

In addition, the second term of eq. 5.16 shows that in steady state each fast mode has excess energy above the equipartition energy, $E_{excess} = \frac{3D}{4\omega_f^4}\delta\omega_f^2 k_{fast}$, where k_{fast} is the stiffness of the fast mode. Each fast mode oscillator dissipates this excess

energy at an average rate $\frac{3D}{4\omega_f^4}\delta\omega_f^2\Gamma k_{fast}$, which balances the input power due to the parametric drive. The total energy loss per unit time from all the fast modes is given by

$$\left\langle \frac{dE}{dt} \right\rangle = \frac{\delta\omega_0^2}{\omega_0^2}\frac{3}{4}\frac{\bar{A}^2 A}{m\beta}\int_0^{q_{max}} \frac{dq}{2\pi}\frac{q^3}{Q\omega(q)} \tag{5.17}$$

where $q_{max} = \sqrt{A/B}$. The damping force F_d due to the coherent tension modulations is given by (setting $\langle h^*(\vec{q}_1)h(\vec{q}_2)\rangle = \frac{1}{2}\bar{A}\sigma_{zz}(2\pi)^2\delta(\vec{q}_1 - \vec{q}_2)$ and taking the expectation value of the eq. 5.6 to find the mean stiffness modulation)

$$F_d = \dot{z}\frac{\tilde{E}\vec{q}^2\bar{A}^2\delta\omega_0}{2\omega_0^3 m\beta}\int_0^{q_{max}} \frac{dq}{2\pi}\frac{q^3}{Q\omega(q)}, \tag{5.18}$$

where $\tilde{E}$ is an elastic constant on the order of the Young's modulus. It can be verified that the damping force given by eq. 5.18 leads to essentially the same energy loss from the excited slow resonator mode as the steady state loss from the fast modes given by eq. 5.17 when the tension is dominated by the stretching from the displacement. Thus, within this picture, energy flows from the slow modes to the fast modes via coherent tension oscillations in the sheet. Energy relaxation can also occur to the wider environment through loss mechanisms such as clamping loss or radiation of in-plane phonons.

For typical device parameters and at room temperature and below this friction force produces a frequency broadening less than Γ_i. We thus expect the frequency broadening to dominate the linewidth. This is consistent with the observed $\propto T$ linewidth dependence.

Relation between steady-state dissipation and the friction force

In steady state, we assume that the motion is effectively ergodic and the time and ensemble averages of quantities related to the motion are equal. The oscillator sus-

ceptibility determines the steady state response of the fundamental mode. The imaginary part determines the mean rate of energy dissipation in the fundamental mode due to energy transfer to the environment. If the frictional damping force is represented by $m\Gamma_d\dot{z}$, then the power dissipated is $P = \frac{1}{2}m\omega_0^2\Gamma_d\langle\delta z^2\rangle$. On the other hand the imaginary part of the susceptibility including frequency fluctuations on resonance is

$$\chi''(\omega) = \frac{1}{\omega_0\Gamma},$$

with Γ determined by the fluctuation broadening, eq. 5.15, assuming that $\Gamma_d << \Gamma$. The dissipated power is then $P = F^2Q/(m\omega_0)$, where F is the magnitude of the sinusoidal force drive. Equating these, we find the mean square amplitude of the motion is

$$\langle\delta z^2\rangle = \frac{F^2}{\Gamma\Gamma_d m^2\omega_0^2}. \tag{5.19}$$

Note that since $\Gamma_d < \Gamma$ this is in general larger than $\langle\delta z^2\rangle$ would be if Γ originated from a frictional force. Nevertheless, the amplitude response measured at the drive frequency, e.g. by a lock-in amplifier will be identical to that determined by $\chi(\omega)$, just as if Γ represented a frictional force. This is because unlike the case of purely frictional force damping, the amplitude response power spectrum is spread out in frequency $\sim \delta\omega$ because of the fluctuating stiffness, while a lock-in measures the amplitude only in a narrow bandwidth around the excitation frequency.

5.3.3 Electrostatic forces effect on quality factor

The electric field up to second order in the height is given by, [61]

$$\begin{aligned} E(\vec{r}) &= \left[-\frac{V}{d}+\frac{V}{d}\int\frac{d^2\vec{q}}{(2\pi)^2}\frac{\cosh(qz)}{\sinh(qd)}qh(q)e^{i\vec{q}\cdot\vec{x}}\right. \\ &- \left.\frac{V}{d}\int\frac{d^2\vec{q}_1}{(2\pi)^2}\frac{d^2\vec{q}_2}{(2\pi)^2}\frac{\cosh(q_2d)}{\sinh(q_2d)}\frac{\cosh(q_1z)}{\sinh(q_1d)}q_1q_2h(\vec{q}_2)h(\vec{q}_1-\vec{q}_2)e^{i\vec{q}_1\cdot\vec{x}}\right]\hat{z} \\ &- \frac{V}{d}\int\frac{d^2\vec{q}}{(2\pi)^2}\frac{\sinh(qz)}{\sinh(qd)}qh(\vec{q})e^{i\vec{q}\cdot\vec{x}}(i\hat{q}) \\ &+ \frac{V}{d}\int\frac{d^2\vec{q}_1}{(2\pi)^2}\frac{d^2\vec{q}_2}{(2\pi)^2}\frac{\cosh(q_2d)}{\sinh(q_2d)}\frac{\sinh(q_1z)}{\sinh(q_1d)}q_2h(\vec{q}_2)h(\vec{q}_1-\vec{q}_2)e^{i\vec{q}_1\cdot\vec{x}}(i\vec{q}_1) \end{aligned} \tag{5.20}$$

where $\vec{r}=(\vec{x},z)$ is the three dimensional position vector for in-plane position $\vec{x}=(x,y)$. Using the expression of the electric field the capacitance correction can be computed from the surface charge density $\sigma_s=\epsilon_0\vec{E}\cdot\hat{n}$ with the unit normal to the graphene membrane $\hat{n}=(\nabla h-\hat{z})/[1+(\nabla h)^2]^{1/2}$. The capacitance C is given by $C=Q/V=\int\sigma_s d\bar{A}/V$. Including this electrostatic term modifies $\mathcal{U}$. Keeping terms up to 2nd order yields additional terms $\Delta\mathcal{U}$ (The 4th order electrostatic term is negligible compared to the mechanical one under typical physical conditions in our experiment).

$$\Delta\mathcal{U}=\int\frac{d^2\vec{q}}{(2\pi)^2}h^*(\vec{q})h(\vec{q})\left(-\frac{\epsilon_0V_g^2}{2d^2}\frac{\cosh qd}{\sinh qd}q-\frac{\epsilon_0V_g^2}{4d}q^2\right)$$

The addition of these terms modifies eq. 5.9 to

$$\langle\delta\omega^2\rangle=\frac{27}{512}\frac{\bar{A}\bar{q}^4\omega_0^2E}{\beta^2k_{eff}^2}\int\frac{dq}{2\pi}\frac{q^5}{\left[-\frac{\epsilon_0V_g^2}{2d^2}\frac{\cosh qd}{\sinh qd}q+(A-\frac{\epsilon_0V_g^2}{4d})q^2+Bq^4\right]^2}, \tag{5.21}$$

This can be approximated by

$$\langle\delta\omega^2\rangle=\frac{27}{512}\frac{\bar{A}\bar{q}^4\omega_0^2E}{\beta^2k_{eff}^2}\int\frac{dq}{2\pi}\frac{q^5}{(C+Dq+Aq^2+Bq^4)^2}, \tag{5.22}$$

with $A=c(V_g)(\lambda+\mu)-\frac{\epsilon_0V_g^2}{4d}$, $B=\frac{1}{2}\kappa$, $C=-\frac{\epsilon_0V_g^2}{2d^3}$, $D=-\frac{\epsilon_0V_g^2}{2d^2}$. Equation 5.22 is used to compute Q by numerical integration and plotted for appropriate parameters in Fig. 5.3.

Chapter 6

Graphene/h-BN NEMS Resonator

Recently hexagonal boron nitride (h-BN), a two-dimensional insulator has been used as a substrate for graphene to achieve ultra-high mobility (60000 cm^2/Vs). [62] For our graphene NEMS resonators, the high field effect mobility is welcomed because it will enhance the transconductance dG/dV_g, which as a result will enhance the signal of mechanical resonance. If the graphene is covered by h-BN without exposing to the air, the electrical quality will be very stable. So we decided to make a graphene/h-BN NEMS resonator and test its performance. In this chapter, we will present some data from a graphene/h-BN drum resonator as well as its fabrication technique.

The strategy we choose for fabricating the device is as follows: Firstly, we prepare an oxidized Si chip with a 2 μm large hole in the SiO_2, and also two electrodes embedded in the SiO_2 on two sides of the hole. To make this chip with predefined hole and electrodes, we use the same techniques as for making the CVD grown graphene drum resonators described in Chapter 2. Secondly, we transfer a graphene/h-BN bilayer on top

of the hole and electrodes, with graphene attached to the electrodes and h-BN covering graphene. Here we follow ref. [63, 64] to fabricate clean graphene devices without being contaminated by polymers. We first use mechanical exfoliation method to deposit thin layer of h-BN and monolayer graphene separately onto two clean oxidized Si chips. Then we put a piece of a polydimethylsiloxane (PDMS) on a glass slide. We spin coat a layer of poly-propylene carbonate (PPC) on top of that. We then use this to pick up the h-BN from the Si chip to the surface of PPC. After that, we pick up the graphene from the Si chip to h-BN on PPC with careful alignment. Now we have a graphene/h-BN heterostructure on PPC with graphene on top of h-BN. Then we transfer graphene/h-BN onto the predefined chip with holes and electrodes, with graphene facing the hole and electrodes. Finally, we dissolve the PPC in Remover PG.

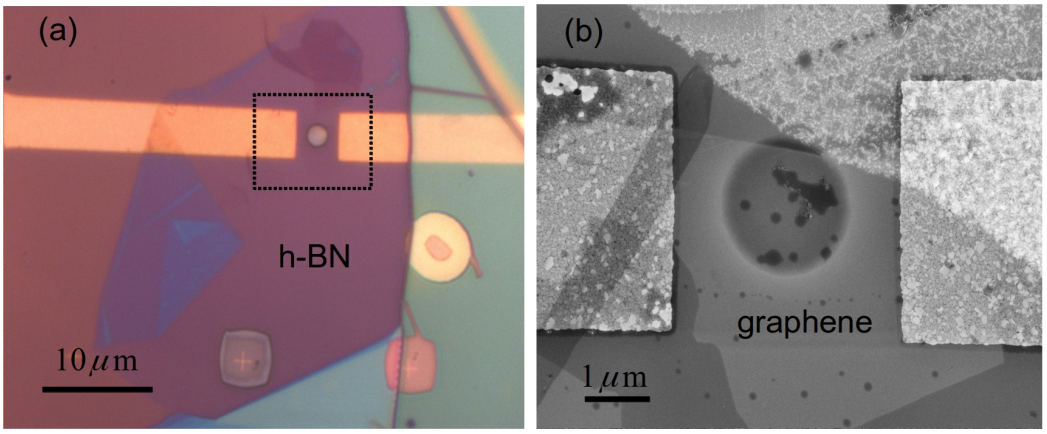

Figure 6.1: Device image of a graphene/h-BN drum resonator with a diameter 2 μm. (a) Optical image of the device. The graphene is monolayer and h-BN is multilayer. The graphene is not visible in the optical image. (b) SEM image of the device.

Fig. 6.2 shows the plot of room temperature conductance vs. gate voltage. The transconductance $dG/dV_g = 27\mu$S/V near the Dirac point, which is much higher than my previous graphene drum resonator devices. Here we use FM mixing technique to actuate and detect the mechanical resonance signal. We apply a FM signal as source-

drain voltage and a DC voltage to the back gate.

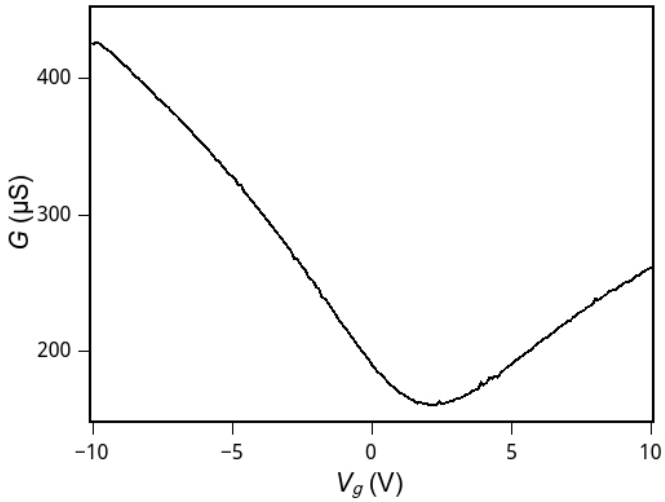

Figure 6.2: Conductance vs. gate voltage at room temperature. $dG/dV_g = 27\mu$S/V near the Dirac point.

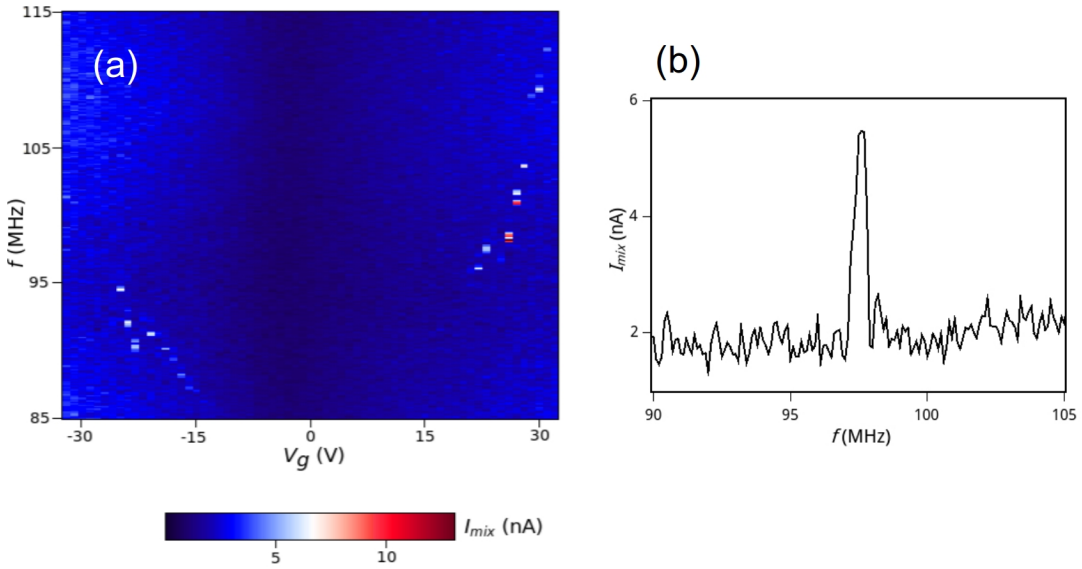

Figure 6.3: Room temperature data of a graphene/h-BN drum resonator with diameter of 2 μm. (a) Color plot of FM mixing signal vs. gate voltage V_g and drive frequency. $V_{sd} = 225$mV. (b) Line trace of mixing signal vs. frequency at $V_g = 23$V.

What is more interesting is that graphene on h-BN can be doped by simply shining a light on the device while a gate voltage V_d is applied. [65] The Dirac point

will shift to and stay at V_d if we turn off the light. Because dG/dV_g is largest near the Dirac point, this will allow us to optimize the Dirac point location and maximize the mechanical resonance signal. Also, if we have a clean device with Dirac point near zero gate voltage, we are usually not able to study the mechanical resonance behavior near the Dirac point. This is because the ac driving force $\tilde{F} = C'V_g\tilde{V}_{sd}$ near zero gate voltage is small and the mechanical resonance mixing signal is also small. However, this photoinduced doping technique for graphene/h-BN device will allow us to study the mechanical resonance behavior near the Dirac point. Graphene's density of states is finite, which makes the problem interesting too.

Chapter 7

Conclusions

7.1 Summary

We mainly studied two problems on graphene NEMS resonators. One is the nonlinear dynamics of graphene drum resonators. As the driving is sufficiently large, the system enters into the nonlinear regime. We measured the coefficient of the Duffing nonlinearity and the nonlinear damping in our devices. We also observed an anomalous large resonance line width at large driving voltage. We attribute this to that the ac source-drain voltage periodically heats the graphene and thus cause the thermal expansion of the graphene. This periodic thermal expansion provides parametric amplification to the amplitude of resonance. Since the resonance line width in the nonlinear damping regime depends on the amplitude, the parametrically amplified amplitude increases the line width more rapidly. Based on this model, we provided the first low temperature measurement of $|a_T|/\kappa_{2D}$, the ratio of graphene's thermal expansion coefficient to its thermal conductivity.

The other problem is the quality factor Q of graphene NEMS resonators. The quality factor Q measured by spectral measurement techniques are low, for our devices

typically on the order of 100 at room temperature and on the order of one to a few thousands at low temperatures down to 4.2K. And we also observed the measured Q of the fundamental mode of our drum resonators scales inversely with the temperature. Various dissipation mechanisms have been proposed [52, 53, 39, 54, 55], but none of them can account for the magnitude, size, [56] and temperature dependence of Q. In chapter 5, we developed a model in which the thermally excited high frequency modes stochastically shift the resonance frequency of the fundamental mode through nonlinear intermodal coupling. The frequency line width is dominated by the stochastic frequency fluctuation instead of the frictional damping. This result predict the same temperature and size dependence [56] of Q in the experiments.

7.2 Future Works

To further confirm whether frequency fluctuation dominates the frequency line width Γ, a time domain experiment such as a ring-down experiment should be able to yield additional insight into the behavior of these systems. If the frequency fluctuation dominates, we should be able to see that it takes a much longer time than $1/\Gamma$ for the oscillation to decay. However, it is very challenging to do these type of measurements on NEMS devices because of the small sizes of the devices. Maybe sometime in the future, new techniques will be developed to overcome these problems.

Bibliography

[1] T. Miao, S. Yeom, P. Wang, B. Standley, and M. Bockrath. Graphene nanoelectromechanical systems as stochastic-frequency oscillators. *Nano Letters*, 14(6):2982–2987, 2014. URL `http://pubs.acs.org/articlesonrequest/AOR-2s7NmgFWCCkPqWVaUVhc`.

[2] K. L. Ekinci and M. L. Roukes. Nanoelectromechanical systems. *Review of Scientific Instruments*, 76(6):061101, 2005. doi:10.1063/1.1927327. URL `http://link.aip.org/link/?RSI/76/061101/1`.

[3] S. Iijima. Helical microtubules of graphitic carbon. *Nature*, 354(6348):56–8, 1991. English.

[4] A. K. Geim and K. S. Novoselov. The rise of graphene. *Nature Materials*, 6:183–191, 2007.

[5] H.-Y. Chiu, P. Hung, H. W. C. Postma, and M. Bockrath. Atomic-scale mass sensing using carbon nanotube resonators. *Nano Letters*, 8(12):4342–4346, 2008.

[6] B. Lassagne, D. Garcia-Sanchez, A. Aguasca, and A. Bachtold. Ultrasensitive mass sensing with a nanotube electromechanical resonator. *Nano Letters*, 8(11):3735–3738, 2008.

[7] J. Chaste, A. Eichler, J. Moser, G. Ceballos, R. Rurali, and A. Bachtold. A nanomechanical mass sensor with yoctogram resolution. *Nature Nanotechnology*, 7(5):301–304, 2012.

[8] V. Gouttenoire, T. Barois, S. Perisanu, J.-L. Leclercq, S. T. Purcell, P. Vincent, and A. Ayari. Digital and fm demodulation of a doubly clamped single-walled carbon-nanotube oscillator: Towards a nanotube cell phone. *Small*, 6(9):1060–1065, 2010. ISSN 1613-6829. doi:10.1002/smll.200901984. URL `http://dx.doi.org/10.1002/smll.200901984`.

[9] C. Chen, S. Lee, V. V. Deshpande, G.-H. Lee, M. Lekas, K. Shepard, and J. Hone. Graphene mechanical oscillators with tunable frequency. *Nature Nanotechnology*, 8(12):923–927, 2013.

[10] A. Eichler, J. Moser, J. Chaste, M. Zdrojek, I. Wilson-Rae, and A. Bachtold. Nonlinear damping in mechanical resonators made from carbon nanotubes and graphene. *Nature Nanotechnology*, 6(6):339–342, 2011.

[11] A. Eichler, J. Moser, M. Dykman, and A. Bachtold. Symmetry breaking in a mechanical resonator made from a carbon nanotube. *Nature Communications*, 4, 2013.

[12] A. C. Neto, F. Guinea, N. Peres, K. S. Novoselov, and A. K. Geim. The electronic properties of graphene. *Reviews of modern physics*, 81(1):109, 2009.

[13] J.-H. Chen, C. Jang, S. Xiao, M. Ishigami, and M. S. Fuhrer. Intrinsic and extrinsic performance limits of graphene devices on SiO_2. *Nature Nanotechnology*, 3(4):206–209, 2008.

[14] C. Lee, X. Wei, J. W. Kysar, and J. Hone. Measurement of the elastic properties and intrinsic strength of monolayer graphene. *Science*, 321(5887):385–388, 2008.

[15] P. Chaikin and T. Lubensky. *Principles of Condensed Matter Physics*. Cambridge University Press, 2000. ISBN 9780521794503. URL `http://books.google.com/books?id=P9YjNjzr9OIC`.

[16] D. Garcia-Sanchez, A. Van der Zande, A. S. Paulo, B. Lassagne, P. McEuen, and A. Bachtold. Imaging mechanical vibrations in suspended graphene sheets. *Nano Letters*, 8(5):1399–1403, 2008.

[17] K. S. Novoselov, A. K. Geim, S. Morozov, D. Jiang, Y. Zhang, S. Dubonos, I. Grigorieva, and A. Firsov. Electric field effect in atomically thin carbon films. *Science*, 306(5696):666–669, 2004.

[18] A. Reina, X. Jia, J. Ho, D. Nezich, H. Son, V. Bulovic, M. S. Dresselhaus, and J. Kong. Large area, few-layer graphene films on arbitrary substrates by chemical vapor deposition. *Nano Letters*, 9(1):30–35, 2008.

[19] J. Velasco Jr, Z. Zhao, H. Zhang, F. Wang, Z. Wang, P. Kratz, L. Jing, W. Bao, J. Shi, and C. N. Lau. Suspension and measurement of graphene and Bi_2Se3 thin crystals. *Nanotechnology*, 22(28):285305, 2011.

[20] S. Lee, K. Lee, and Z. Zhong. Wafer scale homogeneous bilayer graphene films by chemical vapor deposition. *Nano Letters*, 10(11):4702–4707, 2010.

[21] J. D. Caldwell, T. J. Anderson, J. C. Culbertson, G. G. Jernigan, K. D. Hobart, F. J. Kub, M. J. Tadjer, J. L. Tedesco, J. K. Hite, M. A. Mastro, et al. Technique for the dry transfer of epitaxial graphene onto arbitrary substrates. *ACS Nano*, 4(2):1108–1114, 2010.

[22] V. Sazonova, Y. Yaish, H. Ustunel, D. Roundy, T. A. Arias, and P. L. McEuen. A tunable carbon nanotube electromechanical oscillator. *Nature*, 431(7006):284–287, 2004.

[23] C. Y. Chen, S. Rosenblatt, K. I. Bolotin, W. Kalb, P. Kim, I. Kymissis, H. L. Stormer, T. F. Heinz, and J. Hone. Performance of monolayer graphene nanomechanical resonators with electrical readout. *Nature Nanotechnology*, 4(12):861–867, 2009.

[24] V. Sazonova. *A Tunable Carbon Nanotube Resonator*. Ph.D. thesis, Cornell University, 2006.

[25] A. M. van der Zande, R. A. Barton, J. S. Alden, C. S. Ruiz-Vargas, W. S. Whitney, P. H. Q. Pham, J. Park, J. M. Parpia, H. G. Craighead, and P. L. McEuen. Large-scale arrays of single-layer graphene resonators. *Nano Letters*, 10(12):4869–4873, 2010.

[26] A. Eichler, J. Chaste, J. Moser, and A. Bachtold. Parametric amplification and self-oscillation in a nanotube mechanical resonator. *Nano Letters*, 11(7):2699–2703, 2011.

[27] H.-Y. Chiu. *Thermal properties and nanoelectromechanical system based on carbon nanotubes*. Ph.D. thesis, California Institute of Technology, 2009.

[28] F. Guinea, M. I. Katsnelson, and A. K. Geim. Energy gaps and a zero-field quantum Hall effect in graphene by strain engineering. *Nature Physics*, 6(1):30–33, 2010. ISSN 1745-2473.

[29] L. Landau, E. Lifshitz, A. Kosevich, and L. Pitaevskiĭ. *Theory of Elasticity*. Theoretical Physics. Butterworth-Heinemann, 1986. ISBN 9780750626330.

[30] E. V. Castro, H. Ochoa, M. I. Katsnelson, R. V. Gorbachev, D. C. Elias, K. S. Novoselov, A. K. Geim, and F. Guinea. Limits on charge carrier mobility in suspended graphene due to flexural phonons. *Physical Review Letters*, 105:266601, 2010.

[31] V. Singh, S. Sengupta, H. S. Solanki, R. Dhall, A. Allain, S. Dhara, P. Pant, and M. M. Deshmukh. Probing thermal expansion of graphene and modal dispersion at low-temperature using graphene nanoelectromechanical systems resonators. *Nanotechnology*, 21(16):165204, 2010.

[32] I. Kozinsky, H. W. C. Postma, I. Bargatin, and M. L. Roukes. Tuning nonlinearity, dynamic range, and frequency of nanomechanical resonators. *Applied Physics Letters*, 88(25):253101, 2006. ISSN 00036951.

[33] C. Fox. *An Introduction to the Calculus of Variations*. Dover Books on Mathematics. Dover Publications, 2010. ISBN 9780486654997.

[34] P. Morse. *Vibration and sound*. American Institute of Physics for the Acoustical Society of America, 1981. ISBN 9780883182871.

[35] D. W. Koon and C. J. Knickerbocker. What do you measure when you measure resistivity? *Review of Scientific Instruments*, 63(1):207, 1992. ISSN 00346748.

[36] R. Lifshitz and M. C. Cross. *Reviews of Nonlinear Dynamics and Complexity*. John Wiley & Sons, 2009. ISBN 9783527626366. Reproduced with permission.

[37] L. Landau and E. Lifshitz. *Mechanics*. Course of theoretical physics. Butterworth-Heinemann, 1976. ISBN 9780750628969.

[38] S. Zaitsev, O. Shtempluck, E. Buks, and O. Gottlieb. Nonlinear damping in a micromechanical oscillator. *Nonlinear Dynam.*, 67:859–883, 2012. ISSN 0924-090X.

[39] A. Croy, D. Midtvedt, A. Isacsson, and J. M. Kinaret. Nonlinear damping in graphene resonators. *Physical Review B*, 86(23):235435, 2012.

[40] J. Stoker. *Nonlinear vibrations in mechanical and electrical systems*. Pure and applied mathematics. Interscience Publishers, 1950.

[41] W. Z. Bao, F. Miao, Z. Chen, H. Zhang, W. Y. Jang, C. Dames, and C. N. Lau. Controlled ripple texturing of suspended graphene and ultrathin graphite membranes. *Nature Nanotechnology*, 4(9):562–566, 2009.

[42] A. A. Balandin, S. Ghosh, W. Bao, I. Calizo, D. Teweldebrhan, F. Miao, and C. N. Lau. Superior thermal conductivity of single-layer graphene. *Nano Letters*, 8(3):902–907, 2008.

[43] P. Ullersma. An exactly solvable model for Brownian motion: I. Derivation of the Langevin equation. *Physica*, 32(1):27–55, 1966. ISSN 0031-8914.

[44] R. P. Feynman and F. L. Vernon Jr. The theory of a general quantum system interacting with a linear dissipative system. *Annals of physics*, 24(0):118–173, 1963. ISSN 0003-4916.

[45] A. Caldeira and A. Leggett. Path integral approach to quantum Brownian motion. *Physica A*, 121(3):587–616, 1983. ISSN 0378-4371.

[46] A. Fasolino, J. H. Los, and M. I. Katsnelson. Intrinsic ripples in graphene. *Nature Materials*, 6(11):858–861, 2007. ISSN 1476-1122.

[47] V. V. Lebedev and E. I. Kats. Long-scale dynamics of crystalline membranes. *Physical Review B*, 85:045416, 2012.

[48] A. W. Barnard, V. Sazonova, A. M. van der Zande, and P. L. McEuen. Fluctuation broadening in carbon nanotube resonators. *Proceedings of the National Academy of Sciences*, 109:19093–19096, 2012.

[49] R. Shankar. Renormalization-group approach to interacting fermions. *Reviews of Modern Physics*, 66:129–192, 1994. doi:10.1103/RevModPhys.66.129.

[50] P. W. Anderson. A mathematical model for the narrowing of spectral lines by exchange or motion. *Journal of the Physical Society of Japan*, 9:316–339, 1954.

[51] R. Kubo. Note on the stochastic theory of resonance absorption. *Journal of the Physical Society of Japan*, 9:935–944, 1954.

[52] C. Seoánez, F. Guinea, and A. H. Castro Neto. Dissipation in graphene and nanotube resonators. *Physical Review B*, 76:125427, 2007.

[53] F. von Oppen, F. Guinea, and E. Mariani. Synthetic electric fields and phonon damping in carbon nanotubes and graphene. *Physical Review B*, 80:075420, 2009.

[54] X. M. H. Huang, X. L. Feng, C. A. Zorman, M. Mehregany, and M. L. Roukes. VHF, UHF and microwave frequency nanomechanical resonators. *New Journal of Physics*, 7(1):247, 2005.

[55] P. Mohanty, D. A. Harrington, K. L. Ekinci, Y. T. Yang, M. J. Murphy, and M. L. Roukes. Intrinsic dissipation in high-frequency micromechanical resonators. *Physical Review B*, 66(8):085416, 2002.

[56] R. A. Barton, B. Ilic, A. M. van der Zande, W. S. Whitney, P. L. McEuen, J. M. Parpia, and H. G. Craighead. High, size-dependent quality factor in an array of graphene mechanical resonators. *Nano Letters*, 11(3):1232–1236, 2011.

[57] B. Lassagne, Y. Tarakanov, J. Kinaret, D. Garcia-Sanchez, and A. Bachtold. Coupling mechanics to charge transport in carbon nanotube mechanical resonators. *Science*, 325(5944):1107–1110, 2009. doi:10.1126/science.1174290.

[58] G. A. Steele, A. K. Httel, B. Witkamp, M. Poot, H. B. Meerwaldt, L. P. Kouwenhoven, and H. S. J. van der Zant. Strong coupling between single-electron tunneling and nanomechanical motion. *Science*, 325(5944):1103–1107, 2009.

[59] A. Brissaud and U. Frisch. Solving linear stochastic differential equations. *Journal of Mathematical Physics*, 15(5):524–534, 1974. ISSN 00222488.

[60] C. Zerbe, P. Jung, and P. Hänggi. Brownian parametric oscillators. *Physical Review E*, 49:3626–3635, 1994.

[61] Y.-P. Zhao, G.-C. Wang, T.-M. Lu, G. Palasantzas, and J. T. M. De Hosson. Surface-roughness effect on capacitance and leakage current of an insulating film. *Physical Review B*, 60:9157–9164, 1999.

[62] C. Dean, A. Young, I. Meric, C. Lee, L. Wang, S. Sorgenfrei, K. Watanabe, T. Taniguchi, P. Kim, K. Shepard, et al. Boron nitride substrates for high-quality graphene electronics. *Nature Nanotechnology*, 5(10):722–726, 2010.

[63] L. Wang, I. Meric, P. Huang, Q. Gao, Y. Gao, H. Tran, T. Taniguchi, K. Watanabe, L. Campos, D. Muller, et al. One-dimensional electrical contact to a two-dimensional material. *Science*, 342(6158):614–617, 2013.

[64] P. Zomer, M. Guimarães, J. Brant, N. Tombros, and B. van Wees. Fast pick up technique for high quality heterostructures of bilayer graphene and hexagonal boron nitride. *Applied Physics Letters*, 105(1):013101, 2014.

[65] L. Ju, J. Velasco Jr, E. Huang, S. Kahn, C. Nosiglia, H.-Z. Tsai, W. Yang, T. Taniguchi, K. Watanabe, Y. Zhang, et al. Photoinduced doping in heterostructures of graphene and boron nitride. *Nature Nanotechnology*, 9(5):348–352, 2014.